Modelado numérico de un sistema de tipo andino y su respuesta a variaciones climáticas y reológicas

Quinteros, Javier

2008

UNIVERSIDAD DE BUENOS AIRES
Facultad de Ciencias Exactas y Naturales
Departamento de Computación

MODELADO NUMÉRICO DE UN SISTEMA DE TIPO ANDINO Y SU RESPUESTA A VARIACIONES CLIMÁTICAS Y REOLÓGICAS

Tesis presentada para optar al título de Doctor de la Universidad de Buenos Aires en el área de Ciencias de la Computación

Javier Quinteros

Directores:	Pablo Miguel Jacovkis
	Víctor Alberto Ramos
Consejero de estudios:	Pablo Miguel Jacovkis

Lugar de trabajo:	Laboratorio de Tectónica Andina
	Departamento de Ciencias Geológicas
	Facultad de Ciencias Exactas y Naturales - UBA

Buenos Aires, 2008.

Facultad de Ciencias Exactas y Naturales

MODELADO NUMÉRICO DE UN SISTEMA DE TIPO ANDINO Y SU RESPUESTA A VARIACIONES CLIMÁTICAS Y REOLÓGICAS

Resumen

En esta tesis se modelan numéricamente procesos asociados a la tectónica de placas por medio del diseño y la implementación de dos modelos completamente originales basados en el método de los elementos finitos. Además, es la primera vez que se aplican este tipo de modelos numéricos a las regiones tratadas en esta tesis.

El primer modelo está basado en las ecuaciones de Stokes (dinámica de fluidos) y simula la evolución de largo plazo y en gran escala de la corteza en un orógeno de tipo Andino. Este modelo ha sido acoplado con un modelo de compensación isostática y otro de erosión. Se simuló la evolución de la corteza superior de los Andes Australes a los 47°S durante el Mioceno. Se determinó en la simulación el rol clave de la erosión superficial y de la cortical, así como también la aparición de un fenómeno de *rain-shadow*.

El otro es un modelo termo-mecánico y basado en la deformación de sólidos. Es capaz de simular el comportamiento elasto-visco-plástico de los materiales y reproducir procesos geodinámicos hasta una profundidad de 410 km bajo diversas condiciones cinemáticas. Se pueden incluir una cantidad arbitraria de materiales con diferentes propiedades por medio de sus parámetros. No se conocen implementaciones de modelos con este tipo de características que se apliquen al estudio de este tipo de procesos. El modelo fue utilizado para estudiar las particularidades de un proceso denominado *delaminación*. Se simuló la evolución durante casi 9 millones de años (My) de un dominio de 150 km de profundidad y 300 km de ancho que incluye el manto litosférico y astenosférico. En este experimento, las raíces del orógeno se desprenden de la corteza inferior debido a su transformación en *eclogita*.

Además, se presenta en detalle un *framework* de propósito general. Éste fue diseñado para resolver distintos tipos de ecuaciones en derivadas parciales por el método de los elementos finitos. Su diseño modular y el uso adecuado de las abstracciones brindan una gran flexibilidad para utilizar diferentes tipos de elementos para resolver los problemas. También puede ser extendido a otro tipo de ecuaciones y elementos.

Esta tesis es un ejemplo de los avances y mejoras que pueden ser alcanzados en distintas ramas de la ciencia por medio de la investigación y colaboración interdisciplinaria.
Palabras clave: Método de los elementos finitos; Geodinámica; Tectónica de placas; Comportamiento elásto-visco-plástico; Deformación de sólidos; Ecuaciones de Stokes; Andes.

Javier Quinteros

Facultad de Ciencias Exactas y Naturales

NUMERICAL MODELING OF AN ANDEAN SYSTEM AND ITS RESPONSE TO CLIMATIC AND RHEOLOGICAL VARIATIONS

Abstract

Plate tectonic processes are numerically modeled in this thesis by means of the design and implementation of two completely original models based on the finite element method. Besides, it is the first time that this type of numerical models are applied to the regions studied in this thesis.

The first model is based on Stokes equations (fluid dynamics) and simulates the large-scale and long-term evolution of the crust in an Andean-type orogen. It has been coupled with an isostatic compensation model and with an erosion model. The evolution of the upper crust of the Patagonian Andes at 47°C during Miocene is simulated. The key role of the crustal and superficial erosion was determined in the simulation as well as the establishment of a rain-shadow.

The other model is thermo-mechanical and based on solids deformation. It can simulate elasto-visco-plastic behaviour of materials and reproduce geodynamical processes to a depth of 410 km under different kinematical conditions. Any number of materials with different properties can be included in the simulations by means of a proper setting of parameters. No other models with these features have been implemented and applied to the study of this type of processes. The model is employed to study the insights of a geodynamic process called *delamination*. The evolution of a 150 km deep and 300 km wide domain consisting of lithosphere and asthenosphere through almost 9 million years (My) is simulated. In this experiment, the root of the orogen detaches from the lower crust due to its transformation into a dense eclogite.

In addition, a full-featured general purpose framework is presented in detail. This was designed to solve different types of partial differential equations by means of the finite element method (FEM). Its modular design and the proper use of abstractions give a huge flexibility to employ different types of elements to solve the problem. It can also be extended to other type of elements and equations.

This thesis is an example of the improvements and enhancements that can be achieved in different branchs of science by means of the interdisciplinary research and collaboration.

Keywords: Finite element method; Geodynamics; Plate tectonics; Elasto-visco-plastic behaviour; Solids deformation; Stokes equations; Andes.

Javier Quinteros

Agradecimientos / Acknowledgements

I would like to deeply thank the people that gave me support and orientation during these years. To my advisors Víctor Ramos and Pablo Jacovkis. The former had the *inconceivable* idea of facing this multidisciplinary work and the latter guided me through the mathematical maze of numerical modelling.

To Alejandro Otero, Stephan Sobolev, Anton Popov, Alexey Petrunin, Eduardo Dvorkin, Eric Sandvol, Suzanne M. Kay and Pablo Leal. All of them helped to improve the quality of this work by means of fruitful discussions.

Other persons have guided me, not from an academical point of view but from a personal one. To Guillermo Ruiz, Birgit Hollenbach, Cassie Fenton, Aissa Rechlin, Alejandro Otero, Pablo Leal, Ana Tedesco, the members of GeoCine, Javier Elembogien, Fernando Daffara, Patricia Giorgio, Neil McGlashan, Esteban Mocskos, Luciana Baldoni, Jessica Rauch, Gustavo Beade, Martín Kind, Ana Ruedin, Daniel Acevedo, Leticia Seijas, Marita Cadile, Benjamín Heit, Silvia Barredo, Gabriel Bursztyn and many others. Many of them have played an incredibly important role during these years.

A substantial part of this work has been possible thanks to the advice and guidance of Stephan Sobolev, Anton Popov and Alexey Petrunin from GeoForschungsZentrum (GFZ) in Potsdam, Germany.

This research was supported by CONICET, by means of a grant, and the University of Buenos Aires through UBACYT projects X160 and I056.

A mi familia, ahora extendida, que me brindó
su afecto y apoyo incondicional de siempre.
Nada de esto hubiera sido posible sin ellos.

Resumen extendido y conclusiones

La tectónica de placas puede ser vista como la rama de la geología que explica y estudia los movimientos a gran escala de las placas que constituyen la litósfera. Basada en la teoría de la *deriva continental* que propuso Wegener (1915) a principios del siglo 20, sólo fue aceptada mundialmente a partir de la publicación de la teoría de la expansión del fondo oceánico a principios de los años 60 (Vine and Matthews, 1963).

Aunque las causas y procesos que efectivamente llevan a los desplazamientos continentales son conocidos en la actualidad (ver capítulo 2), las mediciones todavía distan mucho de ser precisas. El estudio de la interacción entre estos procesos y su apropiada cuantificación difícilmente podrían ser realizadas por mediciones directas.

El objetivo de esta tesis es desarrollar un modelo numérico termo-mecánico original basado en el método de los elementos finitos. El modelo debe ser lo suficientemente flexible para poder simular distintas condiciones en zonas de subducción, incluyendo variantes geométricas, composicionales y mecánicas.

En esta tesis se presentaron dos modelos numéricos originales. El que se presenta en el capítulo 3 está basado en las ecuaciones de Stokes para simular el comportamiento viscoplástico de la corteza superior. El supuesto subyacente de que las deformaciones elásticas pueden ser descartadas lo transforma en un modelo simple y fácilmente aplicable a la evolución de la litósfera, aunque sólo en caso de un dominio de gran escala y durante un período de tiempo prolongado. Se empleó una típica distribución estacionaria de temperaturas asociada a zonas de subducción. La compensación isostática fue lograda mediante la resolución numérica de la ecuación de una viga de Timoshenko. También se desarrolló un modelo de erosión superficial para estudiar la relación entre el clima y la deformación tectónica, mientras que ciertas técnicas numéricas fueron aplicadas para simular los efectos de la erosión cortical en las cercanías de la trinchera.

El modelo general está basado en los trabajos previos de Beaumont et al. (1992), Willett (1992), Fullsack (1995), Beaumont et al. (2006), aunque varias mejoras fueron introducidas y ciertos problemas fueron solucionados. La inclusión de un componente térmico con variaciones laterales ayuda a tener una evaluación más precisa de la influencia del arco volcánico en zonas de orógenos no formados por colisión. Por otro lado, la posibilidad de modelar la erosión cortical en la trinchera resulta fundamental para poder estudiar la evolución de fenómenos como la migración del arco magmático y sus consecuencias mecánicas.

Se estableció un intercambio apropiado entre los tres componentes (deformación tectónica, compensación isostática y erosión superficial) a través del tiempo. El modelo fue implementado en MATLAB y, debido a esto, cuenta con ciertas limitaciones en el número de elementos que puede manejar.

No obstante, se obtuvieron resultados muy satisfactorios mediante la aplicación de este modelo, particularmente desarrollado para el estudio de zonas de subducción. El modelo fue aplicado a una transecta a aproximadamente 47°S. Los resultados muestran bajos valores de viscosidad en las cercanías del arco magmático debido al alto flujo térmico y, consecuentemente, una zona de mayor debilidad donde el material fluye más fácilmente.

A medida que el orógeno se eleva, la erosión se vuelve cada vez más efectiva. Al alcanzar el primero una cierta altura, los vientos húmedos no pueden sobrepasar la divisoria provocando una distribución marcadamente asimétrica de precipitaciones y erosionando fuertemente el lado occidental. Por otro lado, la migración del arco a causa de la erosión cortical provoca que el lado oriental incremente su gradiente térmico, se deforme y se eleve. La combinación de ambos procesos provoca que migre hacia el este el punto de máxima erosión.

La cantidad de material erosionado durante la simulación coincide con los resultados de Thomson et al. (2001), quienes por medio de trazas de fisión establecieron que la erosión superficial fue de 4 a 9 km en el oeste y menos de 3 km en el este. Asimismo, el orden del volumen de material erosionado es también coherente con el depositado en la *Formación Santa Cruz* (Nullo and Combina, 2002), que abarcan el mismo rango de tiempo que la simulación.

Un hecho particular es el cambio en el estilo de deformación, que cambia su orientación de máxima tasa de deformación desde la zona de *retro-shear* a la de *pro-shear*. Entre los factores que favorecen esto, podemos mencionar la fuerte erosión de la parte occidental y la erosión cortical presente en la trinchera. Lo primero coincide con estudios previos de Beaumont et al. (1992), quien encontró que la remoción de material de un plateau favorece el incremento de la tasa de deformación en ese preciso lugar. Por otro lado, la migración del arco (a causa de la erosión cortical) provoca una migración de los bajos valores de viscosidad, que se verán en sectores cada vez más al este y en profundidad.

El establecimiento de un fenómeno de *orographic rain-shadow* en circunstancias similares a las propuestas por Blisniuk et al. (2005) también puede ser apreciado en la evolución presentada en los resultados.

En este caso particular, es importante remarcar que el modelado de los procesos que actuaron en esta región durante el período considerado es completamente novedoso, contribuyendo a brindar apoyo a ciertas hipótesis geológicas relacionadas con la evolución Miocena de los Andes a estas latitudes.

La capacidad de seguir la evolución de la topografía a través de millones de años, de cuantificar los volúmenes erosionados de roca y el tiempo en que pudo haber ocurrido, de calcular la distribución de las tensiones dentro de la corteza superior, de entender el modo en que las condiciones termales se relacionan con las propiedades mecánicas de la corteza y de brindar la flexibilidad de adaptarse a múltiples geometrías y configuraciones a través de los distintos parámetros, entre otras características, transforman a este modelo en una herramienta poderosa y flexible para los geólogos que investiguen la evolución a gran escala de orógenos formados en zonas de subducción.

Sin embargo, la formulación de este tipo de modelos sufre de un problema de base en el cálculo de la compensación isostática al realizarse por medio de un segundo modelo. Primeramente, puede llevar a la aparición de un alto nivel de tensiones espurias debido a la naturaleza irreal de las condiciones de borde impuestas en la base del dominio. El material se eleva debido a estas condiciones, pero es luego compensado hacia abajo por el modelo isostático como resultado del apilamiento tectónico. Entonces, todo el material se eleva (en una primera aproximación) mientras que en realidad la mayor parte del acortamiento se hunde y transforma en la raíz cortical y sólo una pequeña parte se eleva.

En segundo lugar, el nivel de compensación isostático existe a una cierto nivel relativamente superficial en la litósfera. Si el dominio estudiado necesita incluir el manto astenosférico, el modelo de compensación isostática sería impráctico y hasta inapropiado. Debido a esto, la inclusión del comportamiento elástico que almacena la tensión para compensar regionalmente la distribución de la carga, considerando las fuerzas restauradoras, es completamente necesaria para extender la profundidad a la que se puede simular. Puede verse entonces que la ausencia de una *componente elástica*, que había sido descartada en el modelo de deformación tectónica basado en las ecuaciones de Stokes, de hecho fue incluida de forma no natural mediante la ecuación de la viga.

El modelo presentado en el capítulo 4 está basado en la deformación de sólidos. Puede simular el comportamiento elasto-visco-plástico de las rocas hasta una profundidad de 410 km aproximadamente bajo diversas condiciones cinemáticas. Debido a estas características, el modelo de compensación isostática no es necesario y todos los problemas mencionados son resueltos.

En líneas generales, se buscó extender y mejorar las capacidades de los modelos desarrollados en Babeyko et al. (2002), Sobolev and Babeyko (2005), Babeyko and Sobolev

(2005), Sobolev et al. (2006), Babeyko et al. (2006). Éstos están basados en ecuaciones de dinámica de fluidos con características elásticas, viscosas y plásticas. En este momento son considerados uno de los más avanzados a nivel mundial.

Estos modelos fueron mejorados desde aspectos computacionales, mecánicos y geológicos. Debe aclararse que no existen hasta este momento modelos basados en elementos finitos y que tengan estas características que se apliquen al estudio de los fenómenos de geodinámica detallados a lo largo de esta tesis.

La formulación propuesta ha sido implementada con las siguientes características:

- elemento de cuatro nodos: requiere menos esfuerzo computacional para calcular la solución,
- integración reducida selectiva: evita el bloqueo volumétrico e implica un menor costo computacional,
- una matriz gradiente modificada: disminuye el efecto del *hourglass* causado por la integración reducida.

Se acopló al modelo tectónico un modelo térmico apropiado de manera de calcular con mayor precisión los valores de viscosidad sobre el dominio.

El dominio estudiado puede incluir una cantidad y distribución arbitraria de materiales, cuyas propiedades son tomadas como parámetros y, por lo tanto, independientes del modelo.

También se implementó un algoritmo de remallado basado en la ecuación de Laplace. La posición de los nodos pertenecientes a los bordes del dominio es impuesta como una condición de Dirichlet. La traducción del estado del dominio desde la malla distorsionada hacia la nueva malla sin distorsión es calculada luego del remallado en base a la información (tensión, propiedades del material, etc.) almacenada por las partículas marcadoras (o lagrangeanas).

Los diferentes tipos de comportamiento fueron validados mediante conocidos casos de prueba. Mediante el caso de prueba de la inestabilidad de Rayleigh-Taylor, no sólo se validaron los resultados sino también el correcto desempeño del algoritmo de remallado y mapeo de las variables de estado entre las mallas.

El modelo fue utilizado para estudiar los detalles de un proceso denominado *delaminación*. Como ejemplo, se simuló la evolución de un dominio de 150 km de profundidad y 300 km de ancho que incluye el manto litosférico y astenosférico durante más de 8 My. En este experimento, las raíces del orógeno se separan de la corteza inferior a causa de su transformación en una roca más densa denominada *eclogita*.

Se pudieron identificar los puntos de debilidad del sistema. Básicamente, el contacto entre la eclogita y la base de la corteza y el núcleo mismo del volumen de eclogita existente. Se determinó también que la fuerza ejercida por el manto desde los costados, la ductilidad propia de la eclogita y su exceso de peso debido al incremento de densidad son las principales causas para la formación de una pluma descendente que es empujada y deformada por celdas convectivas compuestas en su mayor parte de astenósfera caliente.

Se cuantificó el rebote isostático que implicaría el desprendimiento de las raíces corticales de un orógeno de 3 km de altura. Luego de un colapso de aproximadamente 550 m, el desprendimiento de la raíz eclogitizada comienza y el orógeno se levanta isostáticamente. Cuando el desprendimiento finaliza, las raíces se sumergen en la astenósfera y el orógeno encuentra el nuevo estado de equilibrio. De los 550 m colapsados, se recuperan cerca de 200 m.

Para alcanzar la flexibilidad necesaria de manera de resolver todas las ecuaciones que comprenden al modelo por el método de los elementos finitos, se diseño e implementó un *framework* de propósito general sobre el cual se programó el modelo presentado en el capítulo 4.

En el capítulo 5 se brindan explicaciones detalladas del diseño y la implementación del *framework* propuesto para resolver problemas asociados a ecuaciones en derivadas parciales mediante FEM. Su diseño modular y el uso apropiado de las abstracciones permitieron brindar una inmensa flexibilidad para emplear distintos tipos de elementos para las resoluciones. Asimismo, permite beneficiarse de la reutilización de código previamente validado, reduciendo el número de errores e incrementando la confiabilidad en el caso de problemas con soluciones no conocidas.

También se implementó un elemento de ocho nodos que no es utilizado particularmente en los experimentos, sino que se incluyó, con muy buenos resultados, para probar la flexibilidad del *framework*. Se muestran algunas medidas de su desempeño, mostrando que el *framework* propuesto no sólo puede ser flexible sino también eficaz desde un punto de vista asociado al tiempo de procesamiento.

Debido a su modularidad, el *framework* podría migrarse fácilmente a un cluster de tipo Beowulf para ser ejecutado en paralelo mediante la técnica del *análisis de subestructuras* propuesto por Bathe (1996).

Es fundamental remarcar que el desarrollo y la utilización de modelos numéricos como herramientas para alcanzar un mejor entendimiento de los procesos geodinámicos a profundidades considerables es de gran importancia para la geología, debido a que la escasez de evidencias y mediciones directas vuelven cualquier cuantificación de los fenómenos una tarea no confiable. En esta dirección, se proveen dos aproximaciones diferentes para el estudio de problemas geodinámicos.

Por último, desde un aspecto computacional, se destaca el diseño e implementación de un *framework* genérico para resolver ecuaciones en derivadas parciales mediante FEM, no como una herramienta cerrada sino como una base o guía para futuros desarrollos de investigadores que, por medio de su propio trabajo, quieran hacer uso o mejorar el *framework* presentado.

El trabajo realizado para esta tesis es un ejemplo de las mejoras y avances que pueden ser alcanzadas en diferentes ramas de la ciencia por medio de la investigación y colaboración interdisciplinaria.

Trabajos futuros y mejoras

Aunque lejos del alcance de esta tesis, el *framework* aquí presentado está siendo ampliado mediante la inclusión de elementos espectrales de alto orden (Patera, 1984, Karniadakis et al., 1985) y elementos que incluyen la *condensación* de sus nodos internos (ver por ejemplo Henderson and Karniadakis, 1995).

También, está siendo incluida, entre las ecuaciones que se pueden resolver, la implementación de un nuevo método llamado *Kinematic Laplacian Equation (KLE)* desarrollado por Ponta (2005) para resolver problemas de dinámica de fluidos. Algunos resultados y características del método KLE pueden ser consultadas en Otero (2006).

Hasta este momento, las condiciones de contorno tienen ciertas limitaciones en el caso de que sean dependientes del tiempo. Para superar estas limitaciones, se evalúa la inclusión de algunas rutinas de parseo (*muParser*) para permitir definir las condiciones como funciones en vez de constantes. De esta manera, las funciones podrían ser pasadas como parámetro en simples archivos de texto sin necesidad de compilarlas en el código.

Se analiza también la inclusión de una interfaz extra para la librería Pardiso (Schenk et al., 2001), de manera de incorporar una alternativa a la ya incorporada SuperLU (Demmel et al., 1999) al momento de resolver el sistema de ecuaciones.

Desde un punto de vista geológico, la aplicación de estos modelos a casos de geodinámica está en sus inicios. Los ejemplos presentados en esta tesis son sólo los primeros de muchos que podrán ser simulados por medio de estas herramientas y abren un nuevo campo de tectónica comparativa que podría ayudar a validar diferentes modelos geológicos propuestos y que están basados en evidencia fragmentada. De esta manera, el presente trabajo contribuye, no sólo a una mejor comprensión de los procesos, sino a sentar nuevas premisas que pueden ser validadas por observaciones geológicas, generando una aproximación iterativa a algunos problemas fundamentales de la geodinámica.

La influencia del coeficiente de fricción entre placas y su relación con la evolución de la faja plegada y corrida, el rol de los sedimentos en la trinchera, las anomalías térmicas por intrusión de magmas, la subducción de dorsales sísmicas y asísmicas, la influencia de fluidos en ambientes tectónicos particulares, la formación y evolución de cuencas de antepaís, la migración del *forebulge* relacionado al avance del frente orogénico y otros son sólo ejemplos de futuros casos que pueden ser simulados por este modelo.

Contents

List of Figures

List of Tables

Dadas tales transformaciones, que pueden lindar con lo paradójico, de nada o de muy poco nos servirá para la aclaración de un concepto el origen de una palabra. Saber que ***cálculo****, en latín, quiere decir* ***piedrita*** *y que los pitagóricos las usaron antes de la invención de los números, no nos permite dominar los arcanos del álgebra...*

Jorge Luis Borges, Sobre los clásicos (Otras Inquisiciones - 1952)

1 Introduction

1.1 Objectives

Plate tectonics can be seen as the branch of geology that explains the large scale motion of the different plates that constitute the lithosphere. Based on the *continental drift* theory proposed by Wegener (1915) in the beginning of the 20^{th} century, its worldwide acceptance began after the appearance of the seafloor spreading theory in the 60's.

Although the actual causes and processes that lead to continental displacements are well known nowadays (see next chapter), the figures remain quite obscure. The study of the interaction among these processes and its proper quantification might hardly be accomplished by direct measurements.

The aim of this thesis is to develop a novel and proper thermo-mechanical model based on the finite element method, flexible enough to simulate different types of subduction conditions, including compositional, geometrical and mechanical variations.

Two original numerical models are provided in this thesis in order to study geodynamical processes. One is based on Stokes equations (fluid mechanics) and simulates the large-scale and long-term evolution of the crust in an Andean-type orogen. It has been coupled with an isostatic compensation[1] model based on the beam equation and with a superficial erosion model in order to study the feedback between climate and tectonic deformation.

The model is based on the previous works of Beaumont et al. (1992), Willett (1992), Fullsack (1995), although many enhancements have been added and some drawbacks were solved. The most interesting, related to the case studied, is the possibility to include the effects of crustal erosion in the trench.

The other one is a complex thermo-mechanical model based on solids deformation that can simulate elasto-visco-plastic behaviour of materials. It can reproduce geodynamical processes up to a depth of 410 km under different kinematical conditions. Any number of materials with different properties can be included in the simulations by means of a proper setting of parameters. It should be noted that the formulation and features proposed and implemented for this model provide much better possibilities than the models that are being already applied to the study of geodynamics.

To achieve the necessary flexibility for the model to deal with the numerical resolution of partial differential equations by means of the finite element method, a generic framework was designed and implemented. The final thermo-mechanical model used to study the geodynamical processes involving the aim of this thesis are implemented over this framework.

The full-featured general purpose finite element method (FEM) framework presented in detail in chapter 5 was designed to solve different types of partial differential equa-

[1]A detailed explanation about isostatic compensation will be found at the beginning of the next chapter.

tions by means of the finite element method. Its modular design and the proper use of abstractions give a huge flexibility to employ different types of elements to solve the problem. It can also be extended to other type of elements and equations.

Due to its modularity, the framework is capable of being easily migrated to a cluster environment by means of the *substructure analysis* proposed in Bathe (1996).

The work done for this thesis is an example of the improvements and enhancements that can be achieved in different branchs of science by means of interdisciplinary research and collaboration.

1.2 Context of this thesis

1.2.1 Geodynamical modeling

In the last twenty years, the development and application of numerical models to the study of plate tectonic processes became a powerful tool to improve and contrast the different theories in this brand new branch of geology.

The very first numerical experiments that showed some success were the ones related to the deflection of the lithosphere. Since the studies of Vening-Meinesz (1941) it is accepted that the lithosphere behaves as a flexed thin plate in response to a tectonic load. Since the early 80's Turcotte and Schubert (1982) proposed the use of the analytical solution of the beam equation to calculate its behaviour. Even if some good results can be achieved by means of this method, some drawbacks should be taken into account. Lateral variations in the effective elastic thickness (T_e) cannot be included in the model [2]. Unfortunately, it is a common fact that sedimentary basins form in zones with large lateral variations, not only of mechanical properties, but also of crustal geometry, resulting in a major limitation when selecting the T_e. Also, the rheology cannot be considered heterogeneous. Due to these reasons, unrealistic high stresses could be predicted along the lithosphere.

[2] A detailed explanation of the *effective elastic thickness* can be found in chapter 2 and 3.

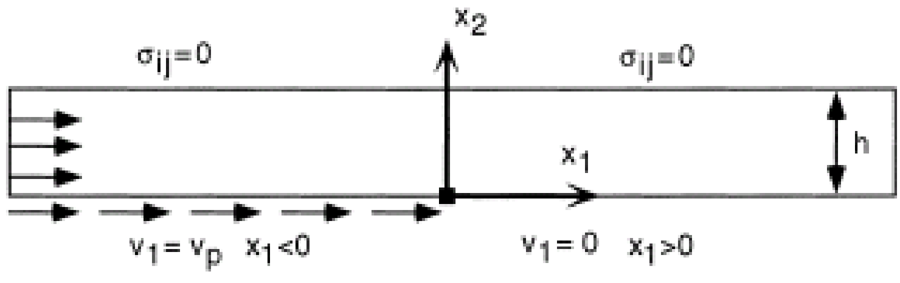

Figure 1.1: Boundary conditions to simulate the subduction motion. After Willett (1999b).

By means of the finite differences method García Castellanos et al. (1997) developed a numerical model that allowed to calculate the evolution of foreland basins under vertical load conditions. The load could be moved through time, simulating a thrust belt. A simple rheology model was included to calculate T_e. In the mechanical part, three modes of operation could be selected: pure elastic, viscoelastic and elastic-plastic. The stress calculation was more accurate, but its relaxation due to the viscous component was only allowed in one of the three modes (viscoelastic). However, even if it was a good implementation at that moment, no real two-dimensional constitutive equations were used and, the most important drawback, kinematic components were not taken into account. The model was able to calculate the deflection under load conditions, but the mechanical variations and kinematic part of the lithosphere were considered as inputs and not a result of the system dynamics.

One of the first models based on partial differential equations that could be considered "complete", from a kinematical point of view, was the one originally proposed by Beaumont et al. (1992) and Willett (1992). Both of them work under the assumption that elastic strains are negligible when deformation is large and that the brittle behaviour of an orogen could be expressed by means of a rigid-plastic rheology. However, they state that it is also formally analogous to a viscous rheology based on the Stokes equations with a plastic behaviour related to the Levy-Mises theory (Malvern, 1969).

They applied the finite element method to solve the equations.

The approach by which they simulate the subduction motion can be seen in figure 1.1. There, a simplified vision of a collision between two continents is proposed, with one continent "fixed" in space (right part of the figure). The non-slip boundary condition imposed over the bottom side of the domain leads to a concentration of the deformation due to the sudden kinematic change. However, the results obtained with this model were accurate enough at that moment and helped reach a better understanding of the continent-continent collision process.

The first versions of this model did not take into account the isostatic compensation, necessary to stabilize the system after the tectonic stacking caused by the collision. One of the main improvements of their work was the coupling of the deformation model with the surface erosion model.

Beaumont et al. (1992) and Willett (1999a) used this model to study the influence of erosion and climate in the way that orogens evolve and the particular features of their final structure. An example of these results is shown on figure 1.2, where one can see the evolution of an orogen that suffers a strong erosion process due to the humid winds that move in the opposite sense of the overriding plate.

The analysis was applied to the Southern Alps of New Zealand, where the wind motion is opposite to the subducting plate motion, and to the Olympic Mountains of Washington State, where the wind and subducted plate motion coincide.

Later, Fullsack (1995) presented an enhanced and more detailed version of the model based on an arbitrary Lagrangian-Eulerian formulation (ALE). It solved Stokes equations using an element with four nodes for velocities and only one node for pressure. Some work-arounds should be applied to avoid numerical issues due to the chosen element.

The isostatic compensation needed to stabilize the system was introduced by means of a second model, which solved the Timoshenko (1934) beam equation as an analogy to the behaviour of the lithosphere (Vening-Meinesz, 1941, Turcotte and Schubert, 1982). This second model was coupled to the deformation one in a similar way as the previ-

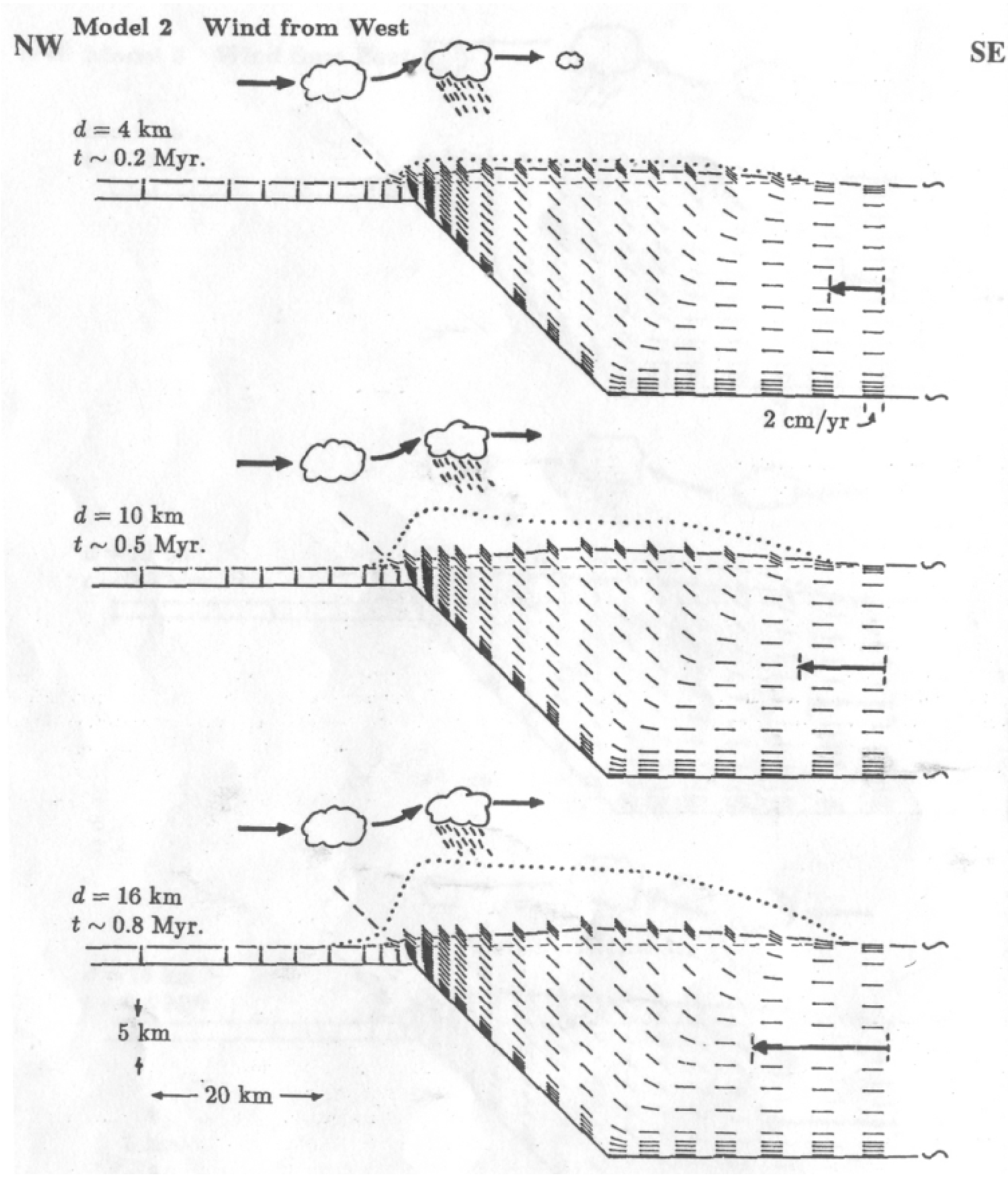

Figure 1.2: Evolution of the plane-strain model when the precipitations come from the west. Dotted lines are the projected position without erosion; black small lines represent velocity and the bold arrow is the total amount of shortening. After Beaumont et al. (1992).

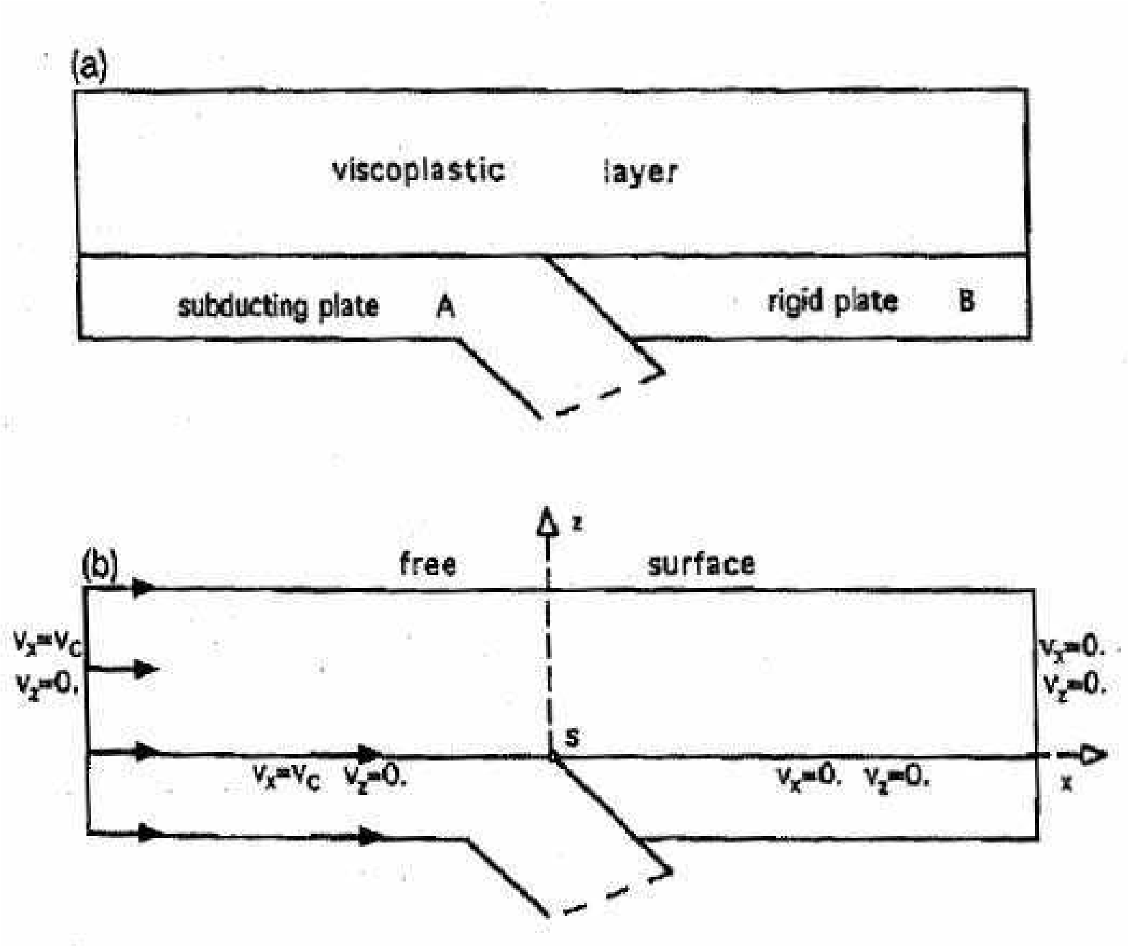

Figure 1.3: Schematic view of the model used by Beaumont et al. (1992) and Willett (1992, 1999a,b) that was formally defined by Fullsack (1995).

ously developed surface erosion model. On one hand, the velocities resulting from the deformation model were updated with the calculations of the isostatic model and on the other, the load distribution of the latter was updated with the results of the former.

In this work, Fullsack mentioned the *inclusion of thermo-mechanical coupling in future versions of the model*.

The absence of a properly coupled thermal model inhibited the application of the code to model deeper parts of the lithosphere, where more complex thermal distributions can be found and the feedback between thermal and mechanical properties needs to be

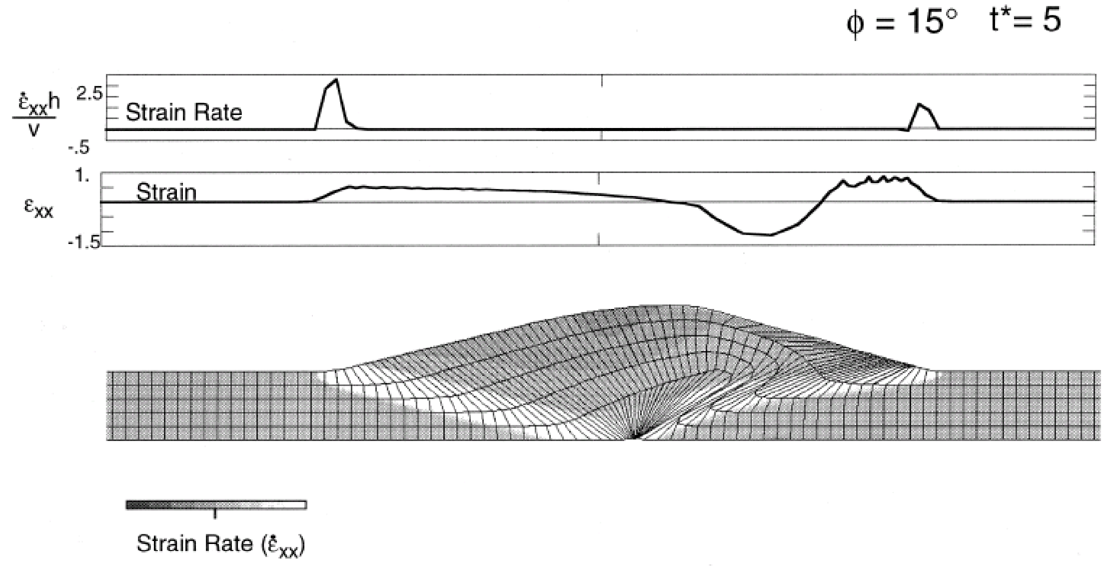

Figure 1.4: Strain and strain rate of a subduction zone with basal and internal angle of friction of 15°. After Willett (1999b).

increased. Only in the last years was this model enhanced with a fully coupled thermal component (Pysklywec and Shahnas, 2003, Pysklywec and Beaumont, 2004).

Some interesting results on the evolution of wedges were published by Willett (1992, 1999b). The work-around in these papers was to simplify the temperature distribution considering it linear and depth dependent.

Figure 1.4 shows one of the cases analyzed by Willett (1999b) under the assumption of a collision. The final topography and distribution of the deformation caused by the compression under particular conditions is calculated to study the influence of the parameters on the existence of small extensional regions in a compressional setting.

Some years ago the models based on fluid equations, that included the elastic component and were able to simulate a more realistic behaviour, became more popular as more accurate results could be obtained if the analogy between long-term deformation and visco-plastic fluid dynamics was discarded. Also, coupling with a proper thermal model facilitates extension to a deeper domain, not only including the upper and lower crust but the lithospheric and asthenospheric mantle. This way, processes that were supposed to occur between 100 and 400 km depth could be modeled and their surface expressions studied and quantified.

Many models were developed with different complexities (see for instance Gemmer et al., 2003), but one of the most complete and successful was the one designed by Sobolev and Babeyko (2005) and Babeyko et al. (2002) called *LAPEX-2D* and based on the prototype published by Poliakov et al. (1993) called *PARAVOZ*.

The model was based on a system of coupled thermo-mechanical equations in 2-D: the momentum conservation and mass conservation equations combined with the constitutive laws and an energy conservation equation.

The model used an explicit scheme with a Lagrangian approach where an inertia term was included in the momentum conservation. It is known that inertial forces are almost nonexistent in this type of problems, due to its quasistatic nature, and usually discarded (Beaumont et al., 1992). The appearance of this *pseudo-inertial* term was considered as a numerical *trick* to allow the explicit integration of velocities (Babeyko et al., 2002).

This inclusion involves some numerical problems in the conditioning of the matrix when long term deformation processes are simulated. This fact led them to use very small time steps in order to work with well-conditioned matrices. In some special cases, the time step was almost half a year (Sobolev, personal communication (2005)), this being too small for simulations of 40 to 50 My of lithospheric evolution.

The test cases performed in order to validate the code showed that the achieved results were satisfactory when the Reynolds number was below 10^{-2} and *reasonably good* with a value equal to 10^{-1}. Unfortunately, in the case of intensive convection of the material, two orders of magnitude above the desired value of the Reynolds number should be used ($Re = 1$) in order to keep the time step above a value that turns the algorithm computationally feasible considering the necessary processing time (Babeyko et al., 2002).

Anyway, the inclusion of a thermal model that was fully coupled to a proper mechanical model, providing a good feedback between them, was a great advance in the application of numerical techniques on geodynamics. Also, it included a quite advanced, complex and realistic rheology that, in combination with both models, could simulate the behaviour of rocks under different geodynamic settings at almost any depth up to 410 km.

Some important contributions about the influence of different parameters in subduction systems were achieved in the last five years by means of its application (see for instance Babeyko et al., 2002, Sobolev and Babeyko, 2005, Babeyko and Sobolev, 2005, Sobolev et al., 2006, Babeyko et al., 2006).

One can see in figure 1.5 one of the results published by Babeyko et al. (2002), that were achieved by means of the explicit model. In this case, the intra-crustal convection caused by increasing heat flow in a geological setting similar to the one in the Puna were simulated.

The study included algorithms to simulate the intrusion of hot material into the strong/weak crust and the rheological changes that this can cause.

A few years later, Sobolev and Babeyko (2005) published a detailed study about the shortening suffered in the Andes and the quantification of the different causes that led the orogen to its present situation. Figure 1.6 shows some snapshots of the simulation made for the evolution of the Central Andes. One can see the thickening of the crust due to the compression and the delamination process that occurs.

The main conclusions of this paper are associated with the relation between the friction coefficient, the displacement velocity of the different plates and the generation of topography in the Central Andes. This constituted one of the most important milestones related to quantification in geodynamics.

Babeyko and Sobolev (2005) used also this model to study the role of the failure of the Paleozoic sediments as a main cause to explain the difference between the development of the Altiplano and the Puna, considering their tectonic deformation styles. One can see in figure 1.7 the three main deformation modes considered to explain the deformation

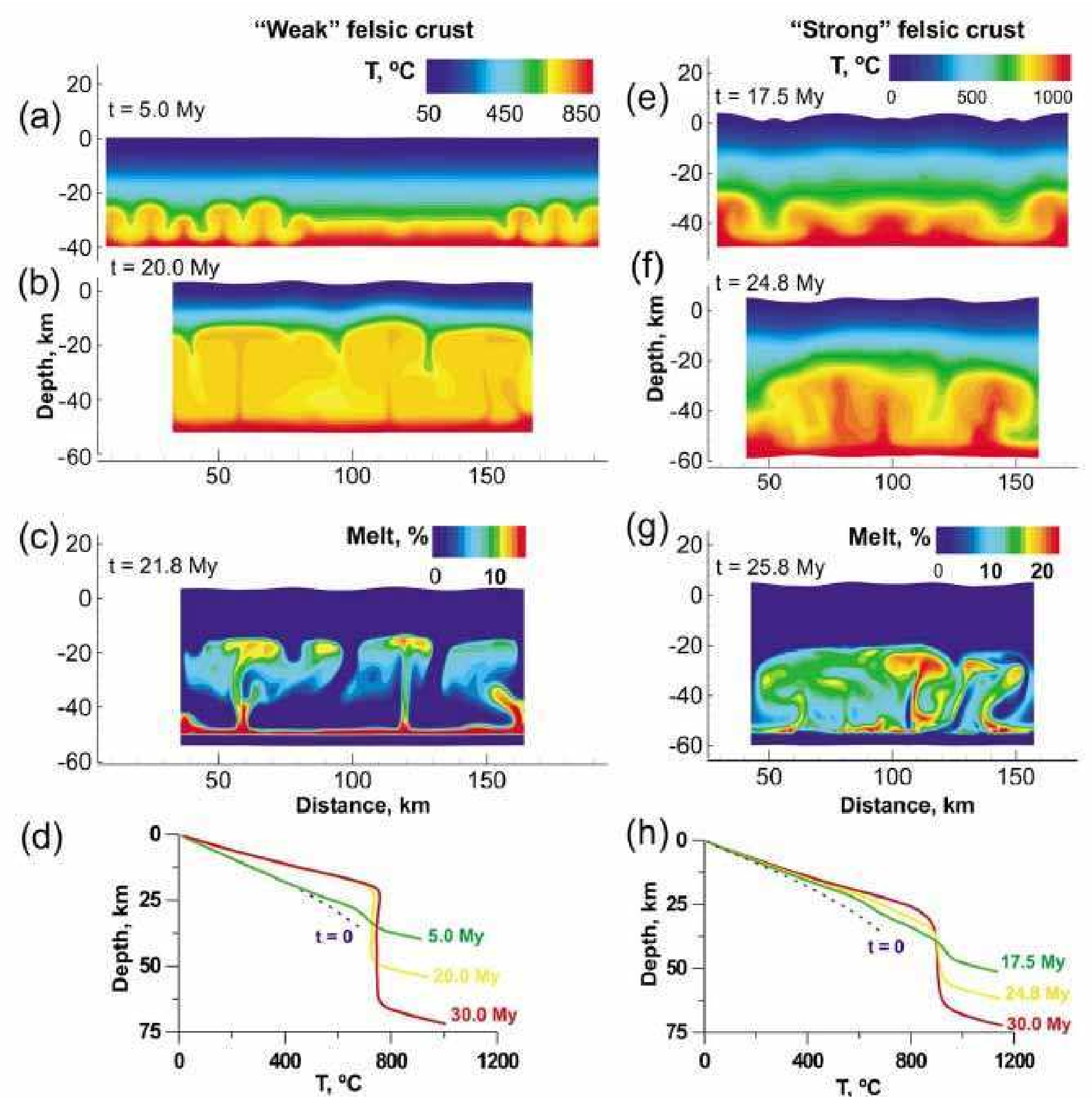

Figure 1.5: Intra-crustal convection caused by increasing mantle heat flow for two different crustal rheologies. After Babeyko et al. (2002).

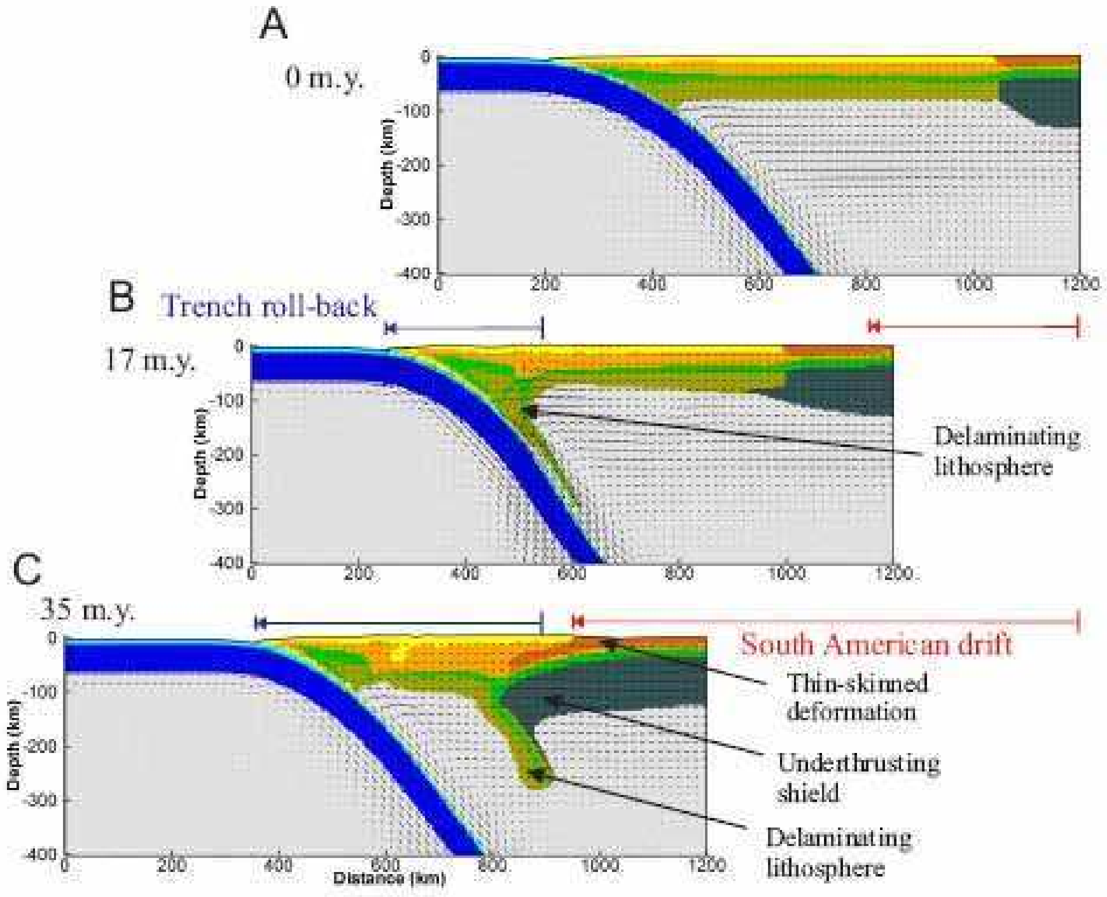

Figure 1.6: Evolution of tectonic shortening from the Central Andes. After Sobolev and Babeyko (2005).

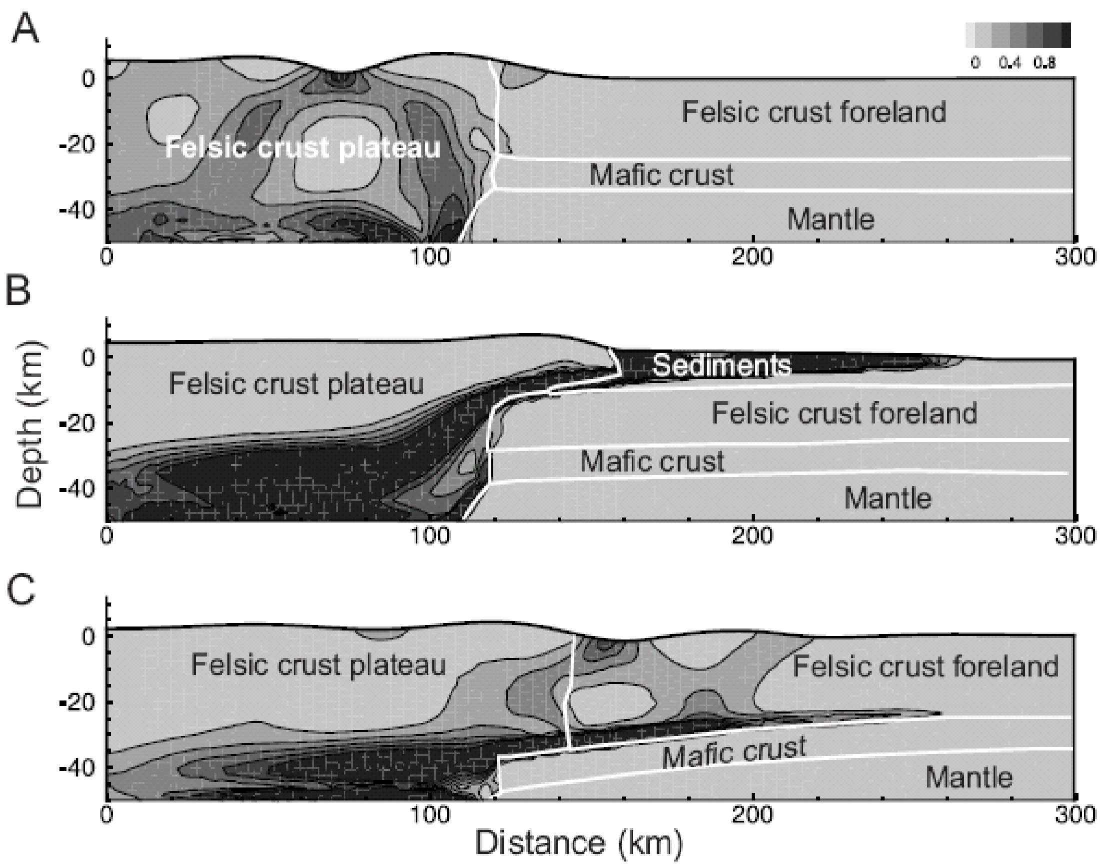

Figure 1.7: Accumulated finite strain after 50 km of shortening for three major deformation modes. (A) Pure shear mode. Cold foreland, normal uppermost crust. (B) Simple shear, thin-skinned mode. Cold foreland, weak uppermost crust. (C) Simple shear, thick-skinned mode. Warm foreland, normal uppermost crust. After Babeyko and Sobolev (2005).

style in the Puna and the Altiplano.

It should be remarked that neither erosion nor sedimentation processes were considered in the different versions of the model used by Sobolev and Babeyko (2005), Babeyko et al. (2002), Babeyko and Sobolev (2005).

1.2.2 Computational mechanics

Considering the computational point of view, some interesting work exists in this area that tries to address the problem of being flexible in the approach used to solve different equations.

In some complex physical processes, where the whole behaviour of the system is described by means of more than one partial differential equation, including the ones related to geodynamics, many common tasks can be found throughout all the computational steps. The numerical resolution of the different equations by the finite element method encompasses many stages that are defined in a generic way.

Even if many implementations can exist to solve some usual problems, these are usually coded from *scratch* with no possibility to adapt them in order to solve specific and complex problems. Specially if these are tightly coupled.

At least two different levels of abstraction can be found in the definition of the finite element method. First of all, the resolution scheme is valid for any element that can be used. This gives the possibility to choose the convergence properties desired/needed for a certain problem, namely the way that the solution should be interpolated. Under some circumstances, some elements can be preferred to others. Besides, some stages like domain definition and discretization, stiffness matrix assemblage and system resolution are independent from the type of problem that needs to be solved.

Some interesting improvements were proposed in the last years to design frameworks with a certain flexibility as to implement this type of abstractions. Among them, we can mention the work published by Sonzogni et al. (2002), where some implementation details of continuum mechanics problems resolution in a Beowulf cluster are given.

Previously, Cardona et al. (1994) presented a framework that allowed some flexibility in the program configuration and the resolution methods used by means of a powerful command interpreter.

Dari et al. (1999) presented a generic framework of resolution to some problems of the continuum mechanics. The user was able to code the resolution methods but did not have to worry about the parallelization and some technical details.

The idea of Dari et al. (1999) was improved in this thesis by defining a specific architecture throughout the framework. This includes general interfaces among the components of the model to isolate them. This way, almost any part of the model can be reused when trying to solve a new problem or when solving the same problem with different approaches.

The main advantage is that the validated parts of the framework can be still considered *valid* if no modifications need to be included inside the classes.

The main objective of the work described is not only to provide a tool to solve different problems of continuum mechanics, but also a framework that allows to reuse the classes designed by means of appropriate abstractions and the constant improvement and variety at the different abstraction layers.

1.3 Outline of the thesis

The geological concepts needed to understand the insights of the models developed in this thesis are carefully explained in chapter 2.

In chapter 3 one can find all the details of a mechanical numerical model based on fluid mechanics equations, designed to represent the crustal deformation in a subduction zone. Processes like crustal erosion, superficial erosion and isostatic compensation are taken into account in this model. A substantial part of this chapter has been already published in the Journal of Applied Mechanics (Quinteros et al., 2006a).

In chapter 4 the details are given of the final thermo-mechanical numerical model based on solid deformation that can handle complex rheologies, as well as elastic, viscous and plastic behaviour. It includes not only the transient mechanical part of the deformation model but also the thermal component of the evolution.

All the specifications concerning the software design insides are given in chapter 5. The relationship among the different classes is shown in a class diagram, as well as the necessary sequence of messages between objects in order to calculate the solution to some specific equations. Also, the implementation details and the validation cases are thoroughly described.

In chapter 6 the results are shown of the application of the models presented in chapters 3 and 4 to some specific geodynamic settings. In addition, the performance of the framework presented in chapter 5 is evaluated by considering the computational time required to solve different problems and some efficiency measures related to the model scalability.

Finally, the conclusions and an outline of possible future works are presented in chapter 7.

Wegener's hypothesis in general is of the foot-loose type, in that it takes considerable liberty with our globe, and is less bound by restrictions or tied down by awkward, ugly facts than most of its rival theories. Its appeal seems to lie in the fact that it plays a game in which there are few restrictive rules and no sharply drawn code of conduct. [...]
Can geology still call itself a science, when it is possible for such a theory as this to run wild? [...]
If we are to believe in Wegener's hypothesis we must forget everything which has been learned in the past 70 years and start all over again.

R. T. Chamberlain, (1928). American geologist.

2

Geological concepts

In the beginning of the 20^{th} century, geology was exclusively related to the study of rocks on land, although some efforts were made to understand the deformation and the characteristics of the mountain systems. The hypothesis governing the ideas of that time was the *fixist hypothesis*, that stated that the continents are essentially stationary and that motions of the crust were basically *vertical*. The presence of marine rocks at the top of some mountains or in large areas of continental land was considered an evidence of that (Moores and Twiss, 1995).

The vertical motion of the crust was closely related to *isostasy*, that was considered one of the main driving forces and the cause of this motion.

2.1 Isostatic compensation: local vs. regional

The differences in the gravity measurements that can cause the presence (or absence) of large mountain belts was heavily discussed during the second half of the 19^{th} century.

Two explanations were put forward. The first one by George Biddel Airy and the second one by John Henry Pratt. Airy was the Director of the Greenwich Observatory, while Pratt was an archdeacon and a devoted scientist. Both theories proposed compensation of the extra mass of a mountain above sea-level by a less-dense region below sea-level, what would later be known as a *crustal root*. However, they differed in the way that the compensation is achieved.

The Airy model assumes an upper layer of constant density floating on a more-dense substratum. It states that under the assumption of complete isostatic compensation, the mass deficiency of the root equals the extra load of the surface. There is a certain compensation depth at and below which the pressure of all the overlying columns is equal. The pressure is then considered to be hydrostatic as if the inner part of the Earth acts like a fluid (see figure 2.1.a). Thus, isostatic compensation is equivalent to Archimedes' principle, considering the mountains as the body which is sunk. An example of this is shown in figure 2.2.

On the other hand, the Pratt model states that a depth level exists (called D) above which any vertical column has constant density up to the surface. Below the base level, the density is constant for every column. This way, the topography has a direct relation to the mean density of its vertical column (see figure 2.1.b).

However, both models relay on the concept of *local compensation isostasy* and it became apparent that both models had serious deficiencies in situations where compensation over a larger region was needed (Lowrie, 1997).

In the 1920's F. A. Vening-Meinesz performed extensive studies at sea trying to clarify the relationship between topography and gravity anomalies over large topographic features. In 1931 he proposed a new model that included the Airy and Pratt models. Under this model, the idea of a light upper layer floating over a denser substratum was

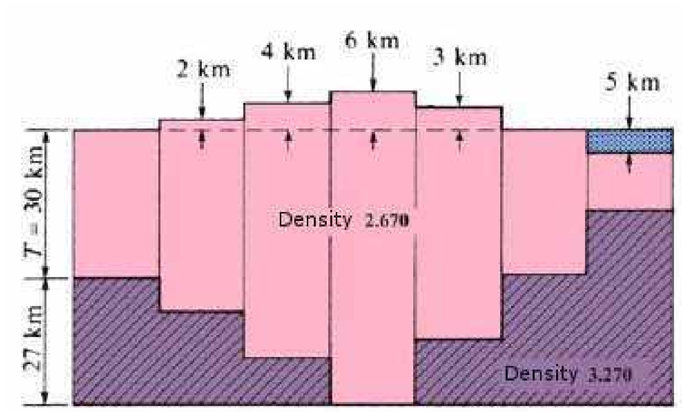

a)

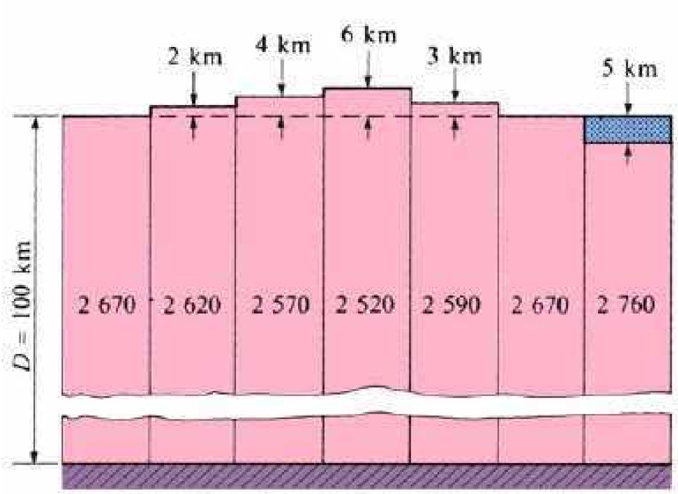

b)

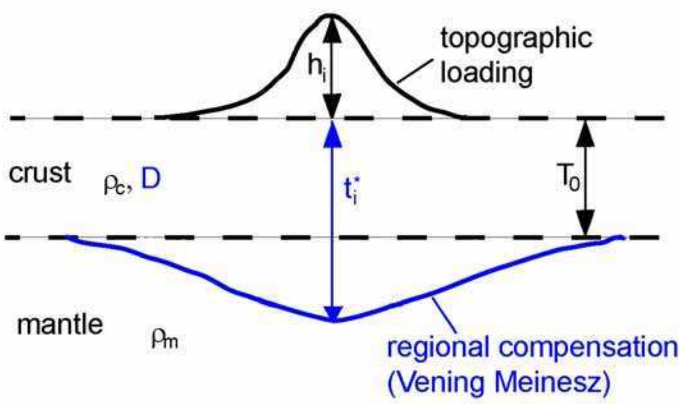

c)

Figure 2.1: The three different isostatic compensation models. a) the Airy model; b) the Pratt model; c) the Vening-Meinesz model. After Suppe (1985).

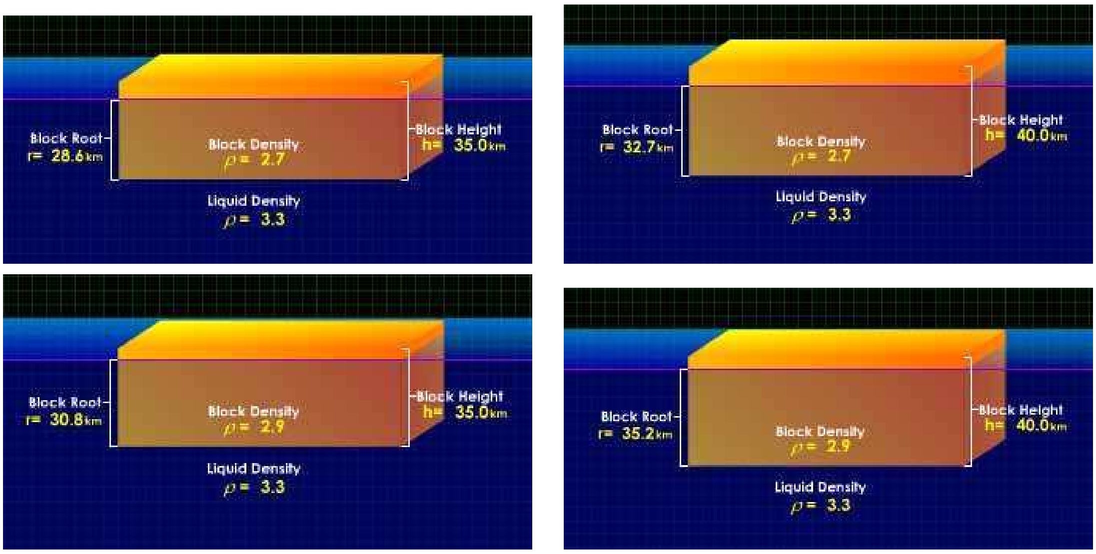

Figure 2.2: Different examples of configurations and its isostatic equilibrium.

still valid, but the strength of the upper crust makes it behave like an elastic plate overlying a weak fluid. Thus, the load of a surface feature can be distributed over a wider horizontal distance compared with the feature (see figure 2.1.c).

The mechanism is more complex than in the Airy and Pratt models. In the first place, the topographic load bends the elastic plate downward into the substratum, which is moved aside. Due to this sinking, the displaced *fluid* exerts an upward force equivalent to its mass. The support, distribution and efficiency given by the upward *restoring* force depends exclusively on the elastic characteristics of the plate, namely the upper crust or lithosphere. Thus, this theory is known as the *regional compensation isostasy* (Vening-Meinesz, 1941).

In section 3.3.3 are given more details about the elastic characteristics of the lithosphere and the problems related to calculating a proper flexural rigidity parameter for the plate.

2.2 Continental drift: A resisted theory

The fixist paradigm had to face many problems in the beginning of the 20^{th} century. One of them was that there was no suitable way to explain the large amount of shortening[1] exhibited in the Alps.

By that time, a meteorologist called Wegener (1915) proposed an alternative hypothesis called *continental drift*. He thought that all the continents had been joined in a supercontinent called *Pangea* and drifted apart until present configuration. This provided a good and feasible explanation to the fitting of the coastlines of the Atlantic as well as its flora and fauna provinces.

The plate motion history as proposed by Wegener (1915) is shown in figure 2.3. It can be seen that the continents were joined in the single Pangea continent and the direction of the displacements through the time.

Although the hypothesis was superior to the fixist one, it was probably too revolutionary for its time, as it was received with great skepticism by many geologists (particularly in North America). The climax of the controversy occured in 1928 in a symposium at the American Association of Petroleum Geologists in New York, where there was consensus to reject the theory (Wegener being present) because no driving mechanism was able to explain the movement of the continents through the oceanic crust (Moores and Twiss, 1995).

2.2.1 Wadati-Benioff zone

At the same time a Japanese seismologist called Kiyoo Wadati showed evidence about the existence of deep earthquakes (at a depth of more than 300 km) (Wadati, 1928). In successive papers, he gave details of earthquakes whose foci were located at different depths, specifying their main characteristics and trying to classify them. Finally, he wrote an article with a compilation of the earthquakes recorded showing that the earthquakes beneath Japan were located mainly along a planar zone that goes from the

[1] A definition of *shortening* can be found later in this chapter.

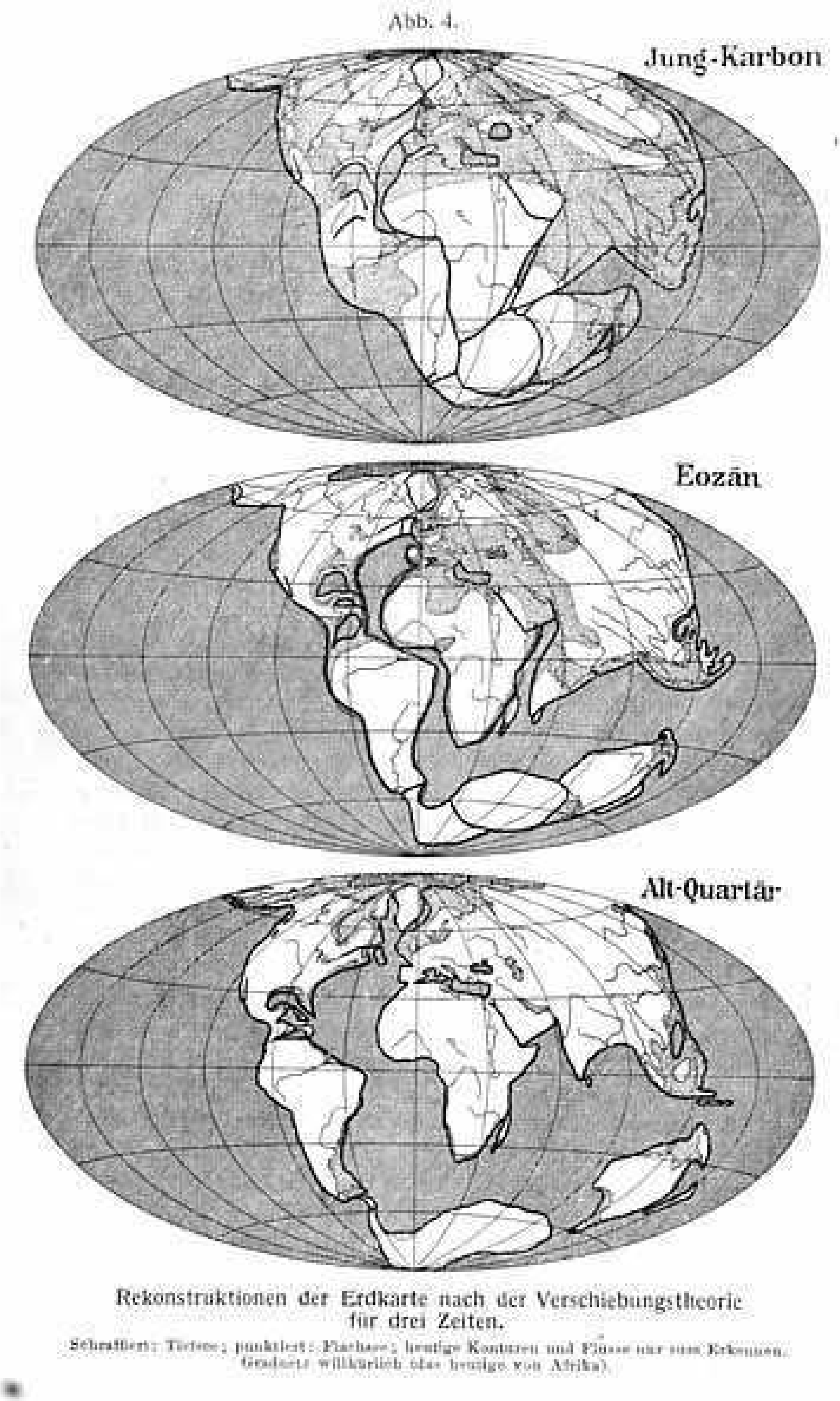

Figure 2.3: The continental drift theory as proposed by Wegener (1915).

eastern trench westwards under the islands (Wadati, 1935).

The graphic originally published by Wadati can be seen in figure 2.4. The lines of equal focal depth were shown, at which intermediate and deep earthquakes occurred frequently. This gave the idea of the inclined planar zone going from the coastline towards the islands. He also noticed that the volcanic zones running along the Japanese Islands were found to coincide with the intermediate earthquakes' lines of equal focal depth. Later, he related this coincidence to the existence of a region of weakness in the intermediate zone and some common force giving rise to the earthquakes and the volcanism, judging from the close relationship between intermediate earthquakes and volcanic zones (Suzuki, 2001).

The scientific community did not pay attention to these articles and it was only in the early 1950's when Hugo Benioff (re)discovered the presence of dipping seismic zones extending deep into the mantle, but this time around the Pacific (Benioff, 1954). The zone was called *Benioff zone*, but many years later was renamed as the *Wadati-Benioff zone*.

2.2.2 Sea-floor spreading

World War II interrupted the normal research of the scientific community. However, two inventions from these years were determinant in the oceanographic investigations: the sonar (to determine the ocean's depth) and the radar (to determine accurately the position of ships).

The huge amount of information collected in the oceans during and after the war caused serious problems to the reigning geological paradigm, which was based mainly in continental studies.

Mountain ranges, that trended north-south, were located in the middle of the oceans (later called *mid-ocean ridges*). These seemed to surround the world and a few years later evidences of great extension along their main axes were reported.

Another Japanese scientist geophysicist called Matuyama (1929) had found that the

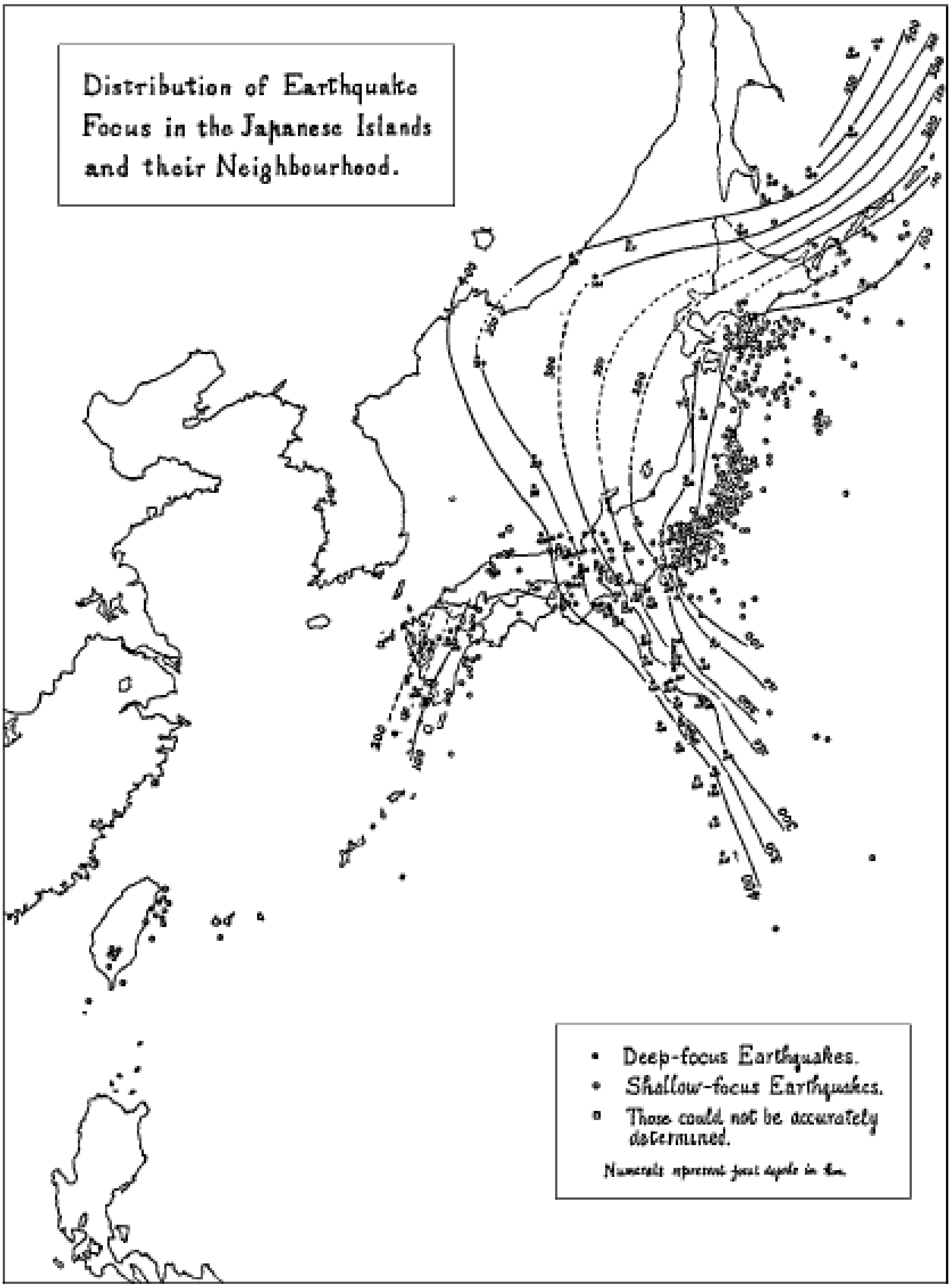

Figure 2.4: Distribution of earthquakes and lines of equal focal depth for intermediate and deep earthquakes. After Wadati (1935).

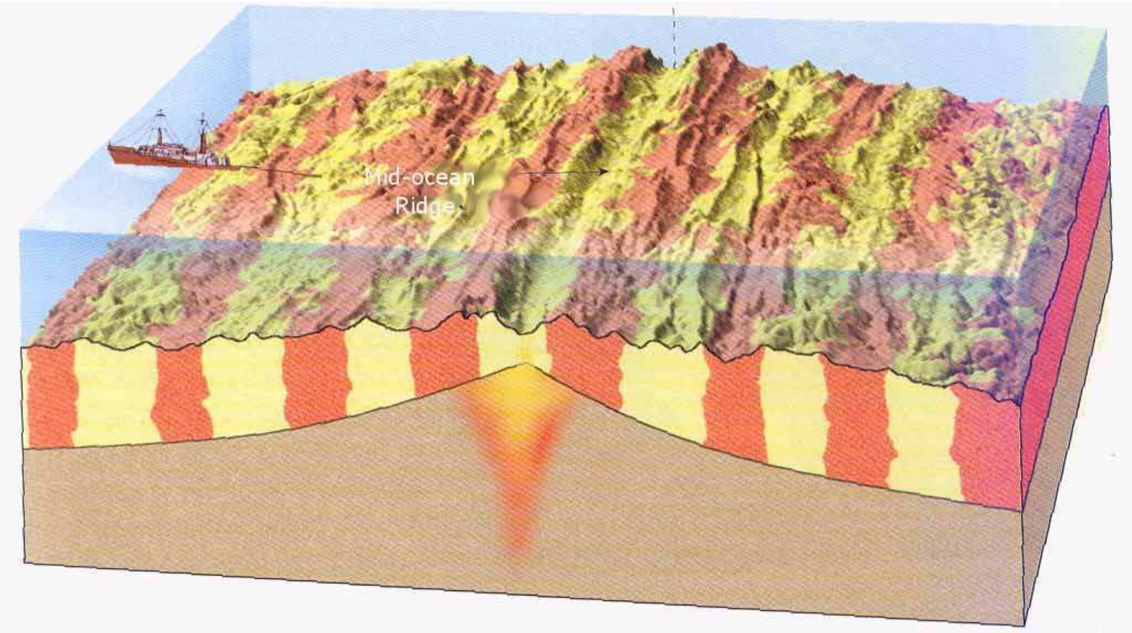

Figure 2.5: View of a mid-ocean ridge with the striplike magnetic anomalies around its main axis. Zones painted with yellow have a normal polarity and the ones in red have a reversal polarity. After Tarbuck and Lutgens (1999).

magnetite contained in some older lavas in Japan pointed to the opposite direction and proposed that the Earth's magnetic field was reversed during the Quaternary. In 1960, a series of long striplike magnetic anomalies were found aligned with respect to the ocean ridges, where a heat flow higher than the average in the ocean was measured. One can see in figure 2.5 how is the usual symmetrical distribution of the anomalies on both sides of the mid-ocean ridge, that has a higher temperature gradient than the rest of the ocean.

The beginning of the paradigm shift finally came in 1963, when L. Morley (in a rejected article)[2] and Vine and Matthews (1963) proposed that the seafloor spreading acted like a recorder preserving the polarity reversals of the Earth and are symmetrically arrayed at both sides of the ocean ridges. A schematic view of this idea is shown in figure 2.6. The seafloor is generated at the mid-ocean ridge and pushes aside the older seafloor.

[2]The original article from Morley was rejected by Nature, stating that they did not have room to print it, and, later, so did the Journal of Geophysical Research, just a couple of months before Vine and Matthews published their paper in Nature. The rejected article was presented one year later with some improvements in a book of the Royal Society of Canada (Morley and Larochelle, 1964).

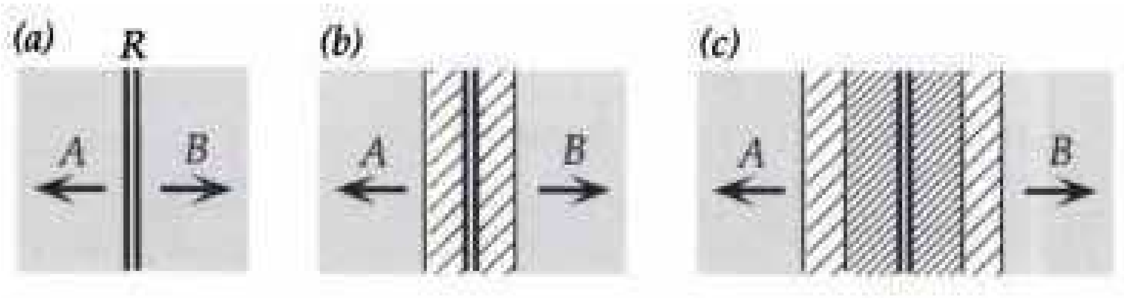

Figure 2.6: Schematic map view of the spreading of seafloor and the reversal fields distribution in striplike anomalies. After Davies (1999).

This way, the magnetic anomalies offset from the ridge with striplike shape.

This was one of the key facts that motivated the acceptance of the seafloor spreading theory. But if the new seafloor is generated at the mid-ocean ridges, it should be destroyed somewhere else due to a lack of space. Hess had proposed that it could be destroyed in the deep ocean trenches like the one in the Peru-Chile coast, but it wasn't until 1968 that Isacks, Sykes, and Oliver (1968) found, by means of seismic studies, that the Wadati-Benioff zone was the expression of a 100 km wide oceanic slab going down from a trench and extending under some volcanic arcs in the Pacific. This was the first recognition of the role of subduction as complementary to the role of seafloor spreading at ocean ridges.

In 1969 there was a worldwide consensus about reinterpreting the continental geology under the new light of plate tectonics, due to the key role and influence that this had in relation to the evolution not only of the oceans but also of the continental part of the Earth.

2.3 Tectonic concepts

In the theory of plate tectonics, the outer part of the Earth (see figure 2.7) consists of two different layers called *lithosphere* and *asthenosphere*. Basically, it can be considered that the lithosphere floats over the asthenosphere. The lithosphere is divided into a reduced number of *plates*, each one of those having different displacements compared to

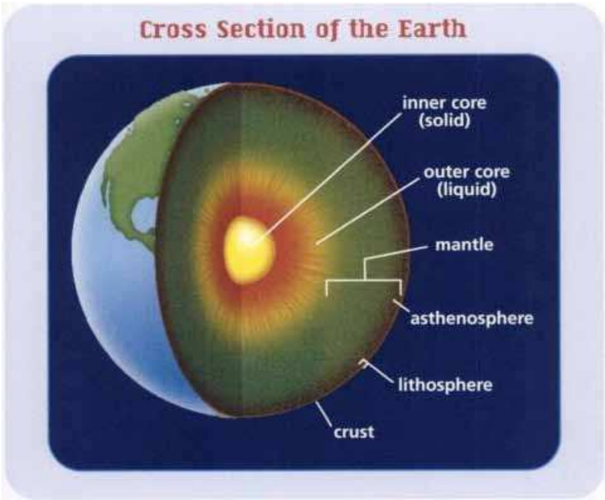

a)

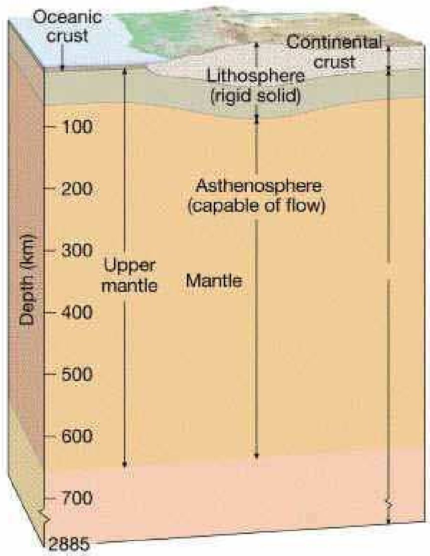

b)

Figure 2.7: a) Schematic view of the inner part of the Earth; b) Detail of the first hundreds of kilometers.

the others.

The difference between lithosphere and asthenosphere is exclusively mechanical and related to the way by which heat is transferred. The lithosphere contains both crust *and* mantle and at different moments a piece of mantle can be part of the lithosphere and the asthenosphere, depending on its temperature. The isotherm that works as a limit between both is approximately at 1300°C.

The cool and rigid lithosphere looses heat by conduction while the hot and mechanically weaker asthenosphere transfers heat by convection and has almost an adiabatic gradient.

The lithosphere covers the whole surface of the planet and the boundary of any pair of plates can be classified into one of the following three definitions (see figure 2.8):

transform: both plates slide past one another,

divergent: both plates move away from each other,

convergent: both plates push against one another.

The present situation of the Earth related to the configuration and distribution of the major plates can be seen in figure 2.9. It should be noted that the Nazca plate is pushing against the South American plate and viceversa. The border between these two plates is an example of a *convergent margin*.

2.3.1 Subduction process

As it was explained in the last section, the Nazca plate is basically the seafloor that was generated in the Pacific mid-ocean ridge and was pushed towards the trench in the coast of Peru-Chile. The trench is the eastern boundary of the Nazca plate and, in general, is the place where oceanic lithosphere bends downward and sinks into the asthenosphere beneath the overriding plate. The name of this process is called *subduction*.

One can see in figure 2.10 a simplification of the subduction of an oceanic plate below a continental one. When the upper part of the subducting oceanic slab has sunk to a depth of 100 km approximately, it contacts the asthenosphere and releases part of its fluids, which migrate upwards. Due to this dehydration, the melting point of the rocks is reduced and starts a process of magma formation which migrates upward forming in the surface a line of volcanoes, called *volcanic arc*.

From a simple and general geometrical point of view, it can be deduced that a higher angle of subduction will imply a shorter distance between the trench and the volcanic arc and viceversa.

The increased heat flow in the volcanic arc will have important mechanical conse-

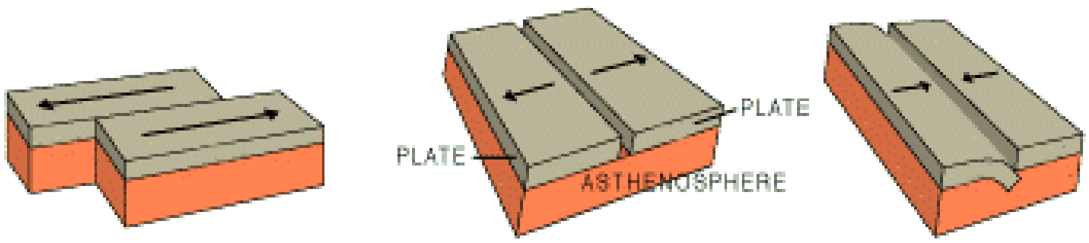

Figure 2.8: Different types of boundary between two plates. From the left: transform, divergent and convergent. Modified from the United States Geological Survey.

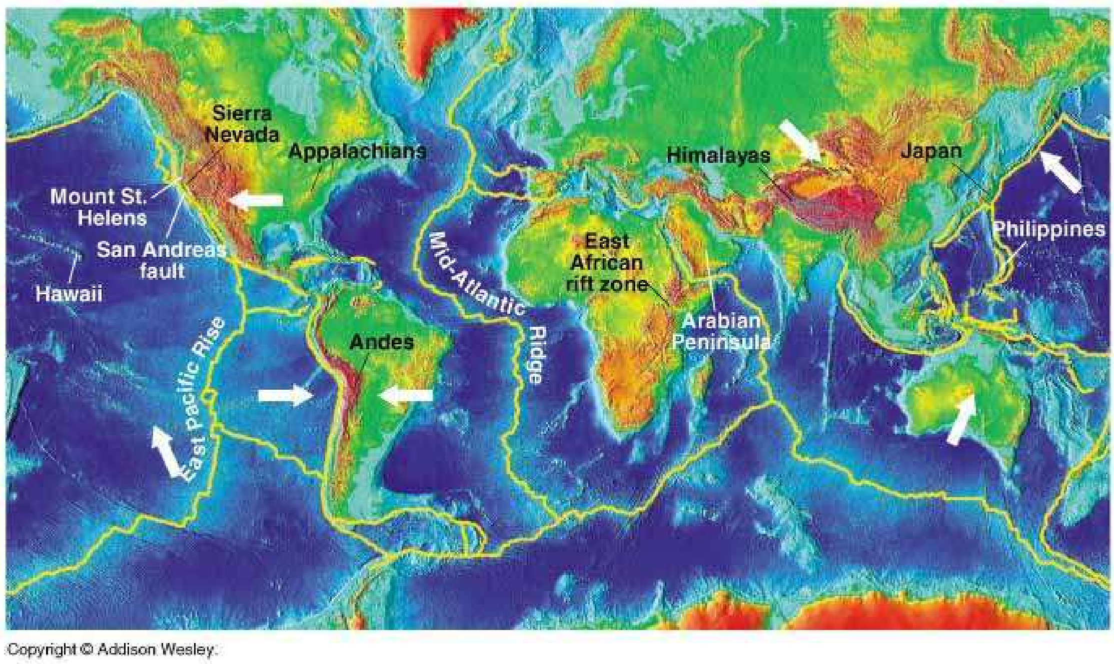

Figure 2.9: Simplified version of the present situation of the tectonic plates

quences. Firstly, the limit between the lithosphere and asthenosphere will be shallower and, due to this reason, the most important consequence is that the rising of the temperature will reduce the viscosity of the rocks turning the vertical column into one of the weakest parts of the lithosphere; thus, increasing the motion of the rocks and concentrating the deformation. Secondly, as the asthenosphere is lighter than the lithosphere, the volcanic arc will isostatically uplift.

On the other hand, the subduction of a cold oceanic slab in the trench implies that the temperature will be colder near this region and thus, the heat flow will be smaller that the average, increasing the viscosity and the density of the rocks, and therefore will isostatically sink.

Considering that at two different moments the amount of material in a vertical section is the same and that it is under compression, the *tectonic shortening* can be defined as the difference between the length at the first moment (Li) and at the second one (Lf), as can be seen in figure 2.11 (Suppe, 1985). Thus, if the mass is conserved, it must happen

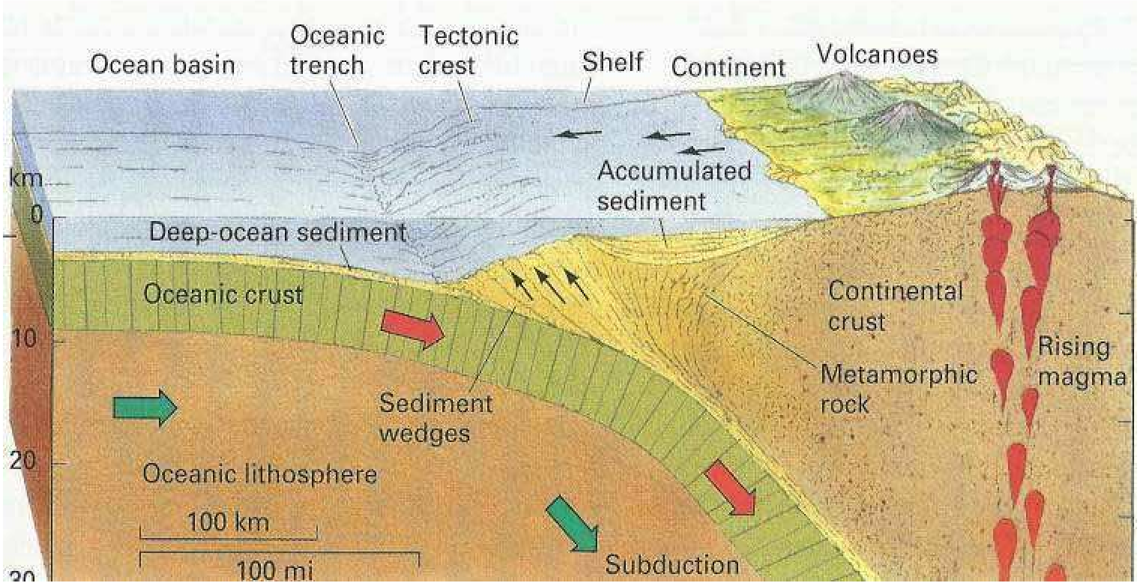

Figure 2.10: Schematic view of the subduction of an oceanic slab below a continental plate.

that the crust thickens at some place of the section considered. This process is known as *crustal thickening* (Cox and Hart, 1986).

At this point, a concept introduced in the beginning of the chapter becomes fundamental. The crustal thickening in the volcanic arc (particularly under compression) will cause the lithosphere to subside due to the isostatic compensation. The space created by the deflection of the lithosphere can be filled with sediments, that are mechanically weaker than the crustal rocks. The crust below the sediments is also weaker due to the increased heat flow, a situation that can lead to a migration of the deformation far away from the trench by developing a *fold and thrust belt*, specially when the extra mass in the volcanic arc and the compression increase the pressure.

In addition, at some particular conditions, the lowest part of the crust can be heated enough as to reduce its viscosity and be pushed towards the previously undeformed foreland in a ductile way. This process is known as *crustal flow* and is more related to viscous channels below the upper crust than to the brittle deformation of the latter (Isacks, 1988).

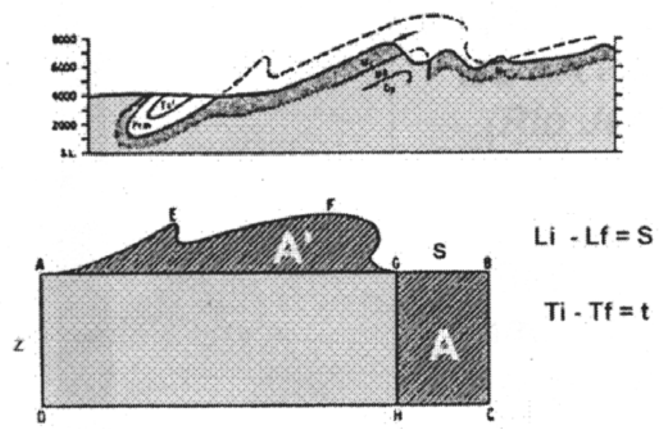

Figure 2.11: Schematic view of a vertical section under tectonic shortening. After Suppe (1985).

2.3.2 Superficial and crustal erosion

The orogen is not only deformed by the stresses resultant from the motion of the plates and their relationship. There are some processes that can modify the evolution of the orogen without the application of external forces. Basically, the removal and transference of material by means of some kind of erosion process. Two different types of erosion can be identified.

Firstly, whenever the orogen rises, it acts as a natural barrier for the humid winds; thus, concentrating the precipitations on one side of the topographic barrier (Ruddiman et al., 1997). There is also consensus about the fact that, the higher the orogen, the more effective is the erosion under the presence of humid winds (Montgomery et al., 2001). Examples of this type of erosion are landslides and wind, that can be considered short range processes, or precipitation and the establishment of a natural drainage, that are considered long range processes (Beaumont et al., 1992).

Again, the isostasy plays a fundamental role as a response to the disequilibrium caused by the lack of material on the sides of the mountain. It is known that the uplift will increase due to the restoring forces related to isostatic compensation.

Secondly, there is another erosion process that does not occur in the surface of

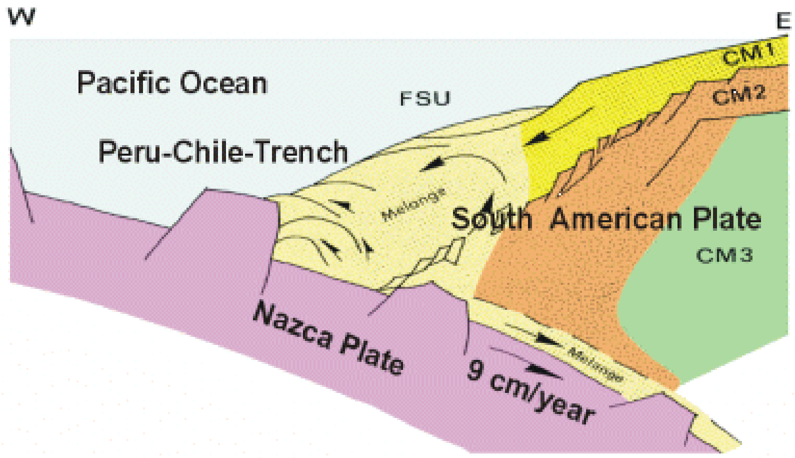

Figure 2.12: Schematic view of a crustal erosion process caused by an oceanic slab with an uneven surface being subducted. The sediments removed from the crust are carried deep into the mantle inside the depressions of the oceanic lithosphere.

the lithosphere, but deep inside. It is called *subduction erosion* (e.g. von Huene and Scholl, 1991). Under certain circumstances, the oceanic plate being subducted can have an uneven surface made of a succession of elevated and depressed parts. Due to the strength of the oceanic lithosphere (stronger than the continental), this can lead to the removal of crustal material from the contact between both plates. One can see in figure 2.12 how the oceanic slab, with a rough surface, carries removed material from the crust deep into the mantle.

No compensation usually occurs in this case, due to the buoyancy of the subducted slab, that *holds* the overriding plate causing important gravitational anomalies near the trench. In addition, the low temperatures associated with the subduction zone make the section to have a regional compensation more than a local one.

In order to couple some of the concepts introduced that are related to the motion of the different morphological units in a subduction zone, Vietor and Echtler (2006) propose the relationship shown in figure 2.13 to achieve a kinematical balance of the plate motions. One can see there that the velocity of overriding (v_o) or absolute velocity of the South American plate is split into three different velocities. Firstly, shortening velocity (v_s) that is associated with the tectonic stacking and the crustal thickening. Secondly,

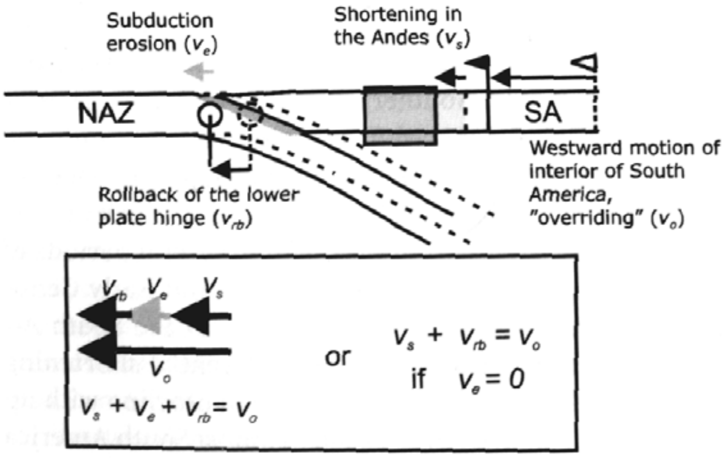

Figure 2.13: Kinematical balance of the plate motions by splitting the overriding velocity into three different ones. After Vietor and Echtler (2006).

the subduction erosion velocity (v_e), that is associated with the material removed from the contact between the oceanic slab and the continental plate. And finally, the trench roll-back velocity (v_{rb}), that is related to the westward motion of the oceanic slab hinge.

Federzoni: *June 22, 1633: dawn of the age of reason! I wouldn't have wanted to go on living if he had recanted. [...] It would have turned our morning to night.*

Andrea: *It would have been as if the mountain had turned to water.*

Bertolt Brecht, Galileo (1938)

3

Initial formulation by means of fluid dynamics equations[1]

The uplift and evolution of a non-collisional orogen developed along a subduction zone, like the Andean system, is a direct consequence of the interrelation between plate tectonic stresses and erosion. Tectonic stresses are related to the convergence velocity and thermal state, among other causes. In this chapter, a new model designed to investigate the evolution of the topography and the upper crustal deformation of non-collisional orogens in a subduction zone produced by the oceanic crust being subducted is presented. The mechanical behaviour of the crust was modelled by means of the finite element

[1]A substantial part of this chapter has been already published in the Journal of Applied Mechanics (Quinteros et al., 2006a).

method (FEM) to solve Stokes equations for a strain-rate dependent visco-plastic rheology. The model takes into account erosion effects using interface tracking methods to assign fictitious properties to non-material elements.

3.1 Objectives

The modelling of the processes related to crustal deformation, due to compression or extension, has been approached in a number of different ways in the last decade. On one side, models that analyze small scale crustal deformation have reached accurate and satisfactory results using mainly formal numerical methods (see for instance Suppe, 1985, Cristallini and Allmendinger, 2001). On the other side, the development of numerical models to study the large scale crustal deformation is continuously evolving because of the multiplicity of processes that take part in the whole evolution of the deformation. Some of these are models based in geometrical properties, considering isotropic rocks (Hindle et al., 2000) while others try to represent more complicated mechanical and rheological properties (Pysklywec and Beaumont, 2004, Babeyko et al., 2002, Gemmer et al., 2003). In the last few years, many authors (see for instance Willett, 1999b, Pysklywec and Shahnas, 2003, Behn et al., 2002) have used the method proposed by Fullsack (1995) for the study of orogens formed by the collision of two plates. In this chapter, a model for non-collisional formed mountain belts (orogens) and well-suited for subduction zones is developed.

3.2 Processes related to subduction

In the last years, several authors have discussed the importance of the different factors that control the uplift of an orogen like the Andes. Some of them suggest that the absolute motion and direction of the plates movement and its convergence velocity are the main causes for the development of an orogen (Pardo-Casas and Molnar, 1987), while others relate it to the amount of sediments in the trench (Lamb and Davis, 2003) or the absolute velocity of the plates (Silver et al., 1998, Sobolev and Babeyko, 2005). Anyway, there is actually consensus on the idea that, in an orogen like the Andes, all these factors can contribute to the generation of stresses along the plate interface. This fact controlls the development of the general tectonics of an Andean orogen. The deformation will also be strongly conditioned by the position of the magmatic arc, which implies a higher thermal flux in the zone and the consequent strong variation in the mechanical properties of the rocks.

In some subduction systems, depending on the coupling between both plates and its features, friction may imply huge quantities of material removal from the overriding plate. This process is known as *subduction erosion* (e.g. von Huene and Scholl, 1991) and has been proved to be one of the main causes of the magmatic arc shifting. The reason is that if the angle of subduction is kept unchanged, the magmatic arc should always be at the same distance from the trench. But, as the trench has moved into the overriding plate, because of the material eroded, the magmatic arc shall migrate in order to keep the distance (e.g., Kay et al., 2005).

At the same time that tectonic stresses deform the upper crust and the orogen develops, erosion can affect the surface, resulting in deeper rocks being exhumed. One of the main causes of erosion is precipitation. It is common that when the orogen reaches a certain yield altitude, precipitation concentrates on the side where the humid winds come from (Ruddiman et al., 1997). When the difference in precipitation is considerable the phenomenon is known as *orographic rain shadow*.

3.3 Overview of the model

The model presented in this chapter consists of three different parts. First, a tectonic model was developed to predict the upper (continental) crustal deformation as a result of the forces applied by the oceanic slab being subducted. In the second place, a surface and subduction erosion model was implemented. Finally, an isostatic compensation model takes into account the flexural behaviour of the lithosphere. All these models are

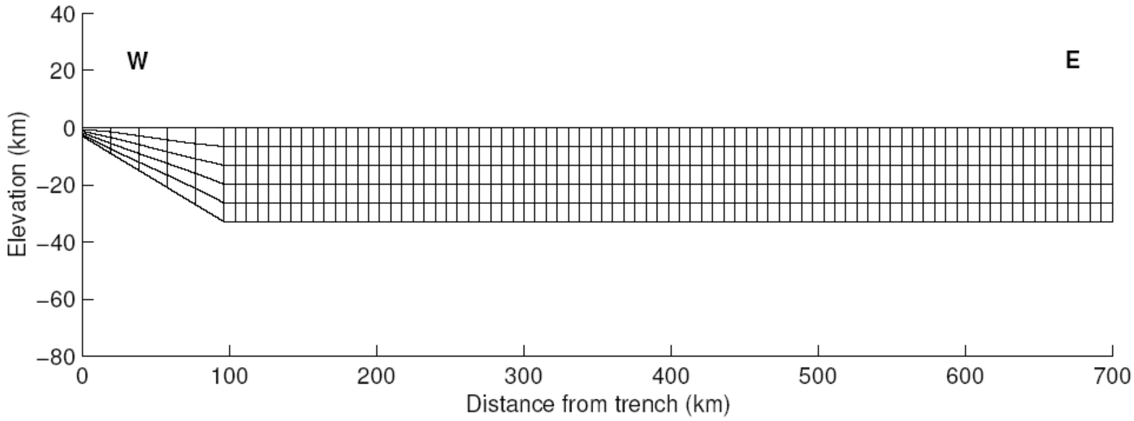

Figure 3.1: Geometry of the vertical section and mesh defined.

coupled at each time step modifying the deformation produced by the compression.

3.3.1 Tectonic model

Although the upper crust is made of rigid solid material, large-scale long-term deformation (tens of thousand years) can be modelled by means of fluid dynamics equations (Fullsack, 1995). In this case, Stokes equations were employed because the process is considered quasi-static and inertial terms are negligible (Beaumont et al., 1992). Dimensionless Reynolds number was considered to be zero in order to model the fluid as laminar and without turbulence. The problem was posed as 2-D and in plane-strain state. The transect (vertical section) was designed with a 700 km long two-dimensional mesh consisting of 1881 nodes (Fig. 3.1).

Finite elements employed are $Q_2 - P_1$ type (Girault and Raviart, 1986), capable of bi-quadratic interpolation for velocities (9 nodes) and linear interpolation for pressures (3 nodes). It has been proved that this element satisfies the inf-sup condition (Brezzi and Fortin, 1991, Bathe, 1996), the basic mathematical criterion that determines whether a finite element discretization is stable and convergent, and avoids side effects as the checkerboard distribution of pressure (Bathe, 1996).

Finite element formulation

The Cauchy stress tensor (σ) is defined as

$$\sigma_{ij} = S_{ij} + P.\delta_{ij} \tag{3.1}$$

where S is the deviatoric stress tensor, P is the trace of the stress tensor or hydrostatic component and δ is the Kronecker delta function. The governing differential equations are the incompressibility equation

$$\nabla.\underline{v} = 0 \tag{3.2}$$

and the equilibrium equation

$$\nabla.\sigma + \rho\underline{g} = 0. \tag{3.3}$$

The constitutive relation is

$$S_{ij} = 2.\mu.\dot{\varepsilon_{ij}}. \tag{3.4}$$

Here $\underline{v}$ is the velocity of the fluid, ρ is the density, $\underline{g}$ is the gravity acceleration, μ is viscosity and $\dot{\varepsilon}$ is the strain-rate. The latter is defined as

$$\dot{\varepsilon_{ij}} = \frac{1}{2}\left[\frac{\partial v_i}{\partial x_j} + \frac{\partial v_j}{\partial x_i}\right] \tag{3.5}$$

where v_i is the velocity of the fluid in the i direction.

Starting with the virtual work principle

$$\int_V \sigma_{ij}.\delta\dot{\varepsilon_{ij}}\partial V = \int_V f_i^B.\delta v_i \partial V + \int_\Pi f_i^S.\delta v_i \partial\Pi \tag{3.6}$$

and splitting strain-rate in a deviatoric and a volumetric part

$$\dot{\varepsilon_{ij}} = \dot{e_{ij}} + \frac{\dot{\varepsilon_v}}{3}.\delta_{ij} \tag{3.7}$$

equations 3.1 and 3.7 can be replaced into equation 3.6, namely

$$\int_V (S_{ij}.\delta \dot{e_{ij}} + P.\delta \dot{\varepsilon_v})\partial V = \int_V f_i^B.\delta v_i \partial V + \int_\Pi f_i^S.\delta v_i \partial \Pi. \tag{3.8}$$

Including the constitutive relation (equation 3.4) it can be rewritten as

$$\int_V \delta \dot{\varepsilon^T}.[I-\frac{1}{3}.m.m^T]^T.2.\mu.[I-\frac{1}{3}.m.m^T].\delta\dot{\varepsilon}\partial V+\int_V \delta\dot{\varepsilon^T}.m.P\partial V = \int_V f_i^B.\delta v_i\partial V+\int_\Pi f_i^S.\delta v_i\partial\Pi \tag{3.9}$$

where $m = [1, 1, 0, 1]$.

After discretization and some algebraic simplification,

$$\left[\int_V B^T[I - \frac{1}{3}.m.m^T]^T.2.\mu.[I - \frac{1}{3}.m.m^T].B\partial V\right] U + \int_V B^T.m.H_P P\partial V = \left[\int_V Hb\partial V + \int_\Pi H^S t\partial\Pi\right]$$

is derived, where H is the velocity shape functions matrix, B is the velocity derivative functions matrix and H_P is the pressure shape functions matrix.

Finally, the following system of equations:

$$K_{uu}.U + K_{up}.P = R \tag{3.10}$$

is obtained, where

$$K_{uu} = \int_V B^T[I - \frac{1}{3}.m.m^T]^T.2.\mu.[I - \frac{1}{3}.m.m^T].B\partial V, \tag{3.11}$$

$$K_{up} = \int_V B^T.m.H_P\partial V, \tag{3.12}$$

$$R = \int_V Hb\partial V + \int_\Pi H^S t\partial\Pi. \tag{3.13}$$

Rewriting equation 3.2,

$$\int_V \delta P(\nabla.v)\partial V = 0, \tag{3.14}$$

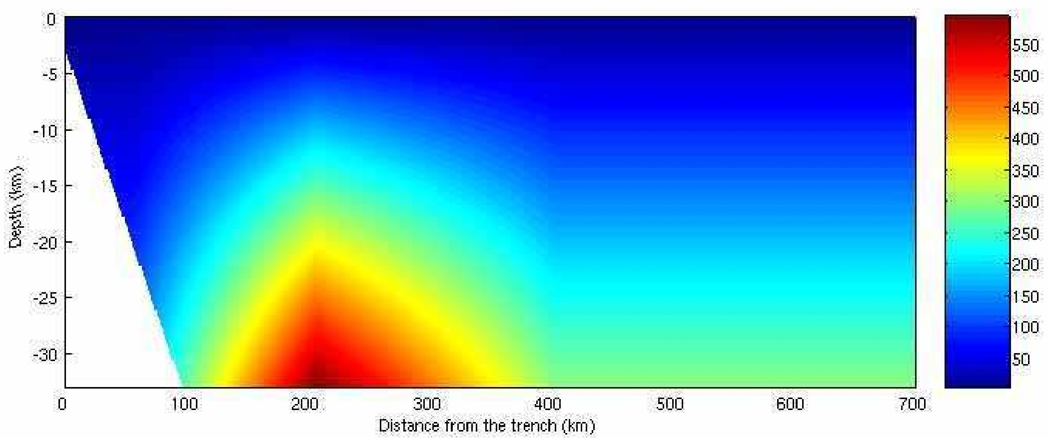

Figure 3.2: Temperature distribution at the beginning of simulation.

$$\int_V \delta P^T H_P^T \dot{\varepsilon_V} \partial V = 0, \tag{3.15}$$

$$\delta P^T \left[\int_V H_P^T . m^T . B \partial V \right] U = 0, \tag{3.16}$$

where

$$\int_V H_P^T . m^T . B \partial V = K_{up}^T . \tag{3.17}$$

Finally, the system given in equations 3.10 and 3.16 can be expressed as

$$\begin{bmatrix} K_{uu} & K_{up} \\ K_{up}^T & 0 \end{bmatrix} . \begin{bmatrix} U \\ P \end{bmatrix} = \begin{bmatrix} R \\ 0 \end{bmatrix} . \tag{3.18}$$

Rheology: dependence and numerical resolution

Temperature in a subduction zone is highly variable from the spatial point of view but quite stable through time, specially when considering large scale modelling. As the viscosity of a rock (μ) is related to the composition of materials and the temperature to which it is exposed, the variation in viscosity can be of several orders of magnitude between minimum and maximum values. Penalization techniques were avoided because of this reason, as it is probable that the precision needed turns the matrix ill-conditioned. Mixed elements are used instead in order to achieve the totally incompressible solution.

Parameter	Definition	Value	Units
A	Material strength constant	$2.91 * 10^{-3}$	MPa^{-1} s^{-1}
Q	Molar activation energy	151	kJ mol^{-1}
n	Power law exponent	1.8	
R	Universal gas constant	8.3144	J mol^{-1} K^{-1}
T	Temperature		K
$\dot{\varepsilon_o}$	Reference strain rate	10^{-14}	s^{-1}
σ_0	Frictional cohesive strength	50	MPa
Θ	Angle of internal friction	15	$\circ$
S_w	Initial atmospheric water (vapour) flux	$8 * 10^{11}$	mm^2 yr^{-1}
Δt	Time step	10^4	yr
hs	Altitude scale		
mpc	Minimum precipitation coefficient		
apc	Available precipitation coefficient		

Table 3.1: Parameters of the model based on Stokes equations.

Temperature is considered to have a two-dimensional distribution as can be seen in figure 3.2 and is based on the classical study of Ernst (1975). The magmatic arc position (the warmest part) is consistent with the subduction angle, the supposed depth where the magmas were produced and the geological evidence.

In the uppermost part of the lithosphere, temperature and pressure are relatively low and fractures and frictional sliding define the mechanical behaviour. That is known as *brittle regime*. When depth increases, and also temperature and pressure, viscous flow is the default mechanical behaviour (Kohlstedt et al., 1995). That process is the *ductile regime*.

Many authors have studied the behaviour of the different rocks varying temperature and pressure conditions to which they are exposed (Jaoul et al., 1984, Mackwell et al., 1998). Although sometimes exclusively temperature dependent viscosity is used in modelling (Pysklywec and Shahnas, 2003), it is usual to consider more than one variable for rheology that has to be employed in large scale modelling, particularly strain rate ($\dot{\varepsilon}$), material rigidity (A), temperature (T), activation energy (Q) and a power law exponent (n), among others (equation 3.19). Many of these constants can be seen in table 3.1. The viscosity is defined as

$$\mu = A^{-\frac{1}{n}}.\dot{\varepsilon_{II}}^{\frac{1-n}{n}}.e^{\frac{Q}{nRT}} \tag{3.19}$$

where $\dot{\varepsilon_{II}}$ is the square root of the second invariant of the strain-rate tensor and R is the universal gas constant (Tsenn and Carter, 1987).

In order to be consistent with the *brittle regime*, shear stress at any point cannot be greater than the maximum shear stress supported by rocks (σ_y) (Byerlee, 1978), that can be expressed as

$$\sigma_y = \sigma_0 + \frac{\Phi - 1}{\Phi}.\rho g z \tag{3.20}$$

where σ_0 is the frictional cohesive strength, $\frac{\Phi-1}{\Phi}$ is the coefficient of friction,

$$\Phi = \left[(1+\eta^2)^{\frac{1}{2}} - \eta\right]^{-2} \tag{3.21}$$

and

$$\eta = \tan(\theta), \tag{3.22}$$

being θ the angle of internal friction considered.

Because of the non-linearity produced due to the strain-rate dependence, an iterative algorithm (table 3.2) is used until a desired level of convergence is achieved.

For the first iteration, the viscosity (μ) is calculated as a function of temperature (T) and a reference strain-rate ($\dot{\varepsilon_0}$). The viscosity distribution calculated is employed to assemble the finite element matrix and to calculate the pressures and velocities. Later, the strain-rate is recalculated using the velocity and the viscosity is updated based on the resulting strain-rate.

For elements in which the resulting shear stress (equation 3.4) is greater than the

procedure STOKES
  $\mu_0 \leftarrow f(T, \dot{\varepsilon_0})$ ▷ Start with a reference strain-rate
  repeat
    $K \leftarrow K(\mu_k)$ ▷ Assemble stiffness matrix
    $P = \left(K_{up}^T K_{uu}^{-1} K_{up}\right)^{-1} K_{up}^T K_{uu}^{-1} R$ ▷ Calculate pressure
    $U = K_{uu}^{-1}\left[R - K_{up}\ P\right]$ ▷ Calculate velocity
    $\dot{\varepsilon}_{ij} = \frac{1}{2}\left[\frac{\partial v_i}{\partial x_j} + \frac{\partial v_j}{\partial x_i}\right]$ ▷ Calculate strain-rate
    $k++$ ▷ Go to the next step
    $\mu_k \leftarrow f(T, \dot{\varepsilon_{II}})$ ▷ Recalculate viscosity
    if $S > \sigma_y$ **then** ▷ If stress > failure criterion
      $\mu_k = \frac{\sigma_y}{2\ \dot{\varepsilon}_{II}}$ ▷ Reset viscosity
    end if
  until $\|\mu_k - \mu_{k-1}\| < TOL$ ▷ Iterate until convergence is achieved
    return μ_k and U ▷ Viscosity distribution and velocities are returned
end procedure

Table 3.2: Algorithm to calculate deformation due to tectonic compression.

frictional failure criterion (equation 3.20), the effective viscosity (μ) is reset to

$$\mu = \frac{\sigma_y}{2.\dot{\varepsilon_{II}}}. \tag{3.23}$$

Thus, shear stress remains on the plastic yield by reducing the viscosity.

Once the viscosity difference between two iterations is considered to be small enough (lesser than a tolerance TOL), iteration ends.

Interface tracking and numerical treatment

In this model, two interfaces are defined (Fig. 3.3):

- a surface interface, that tracks the shape of the topography resulting from the

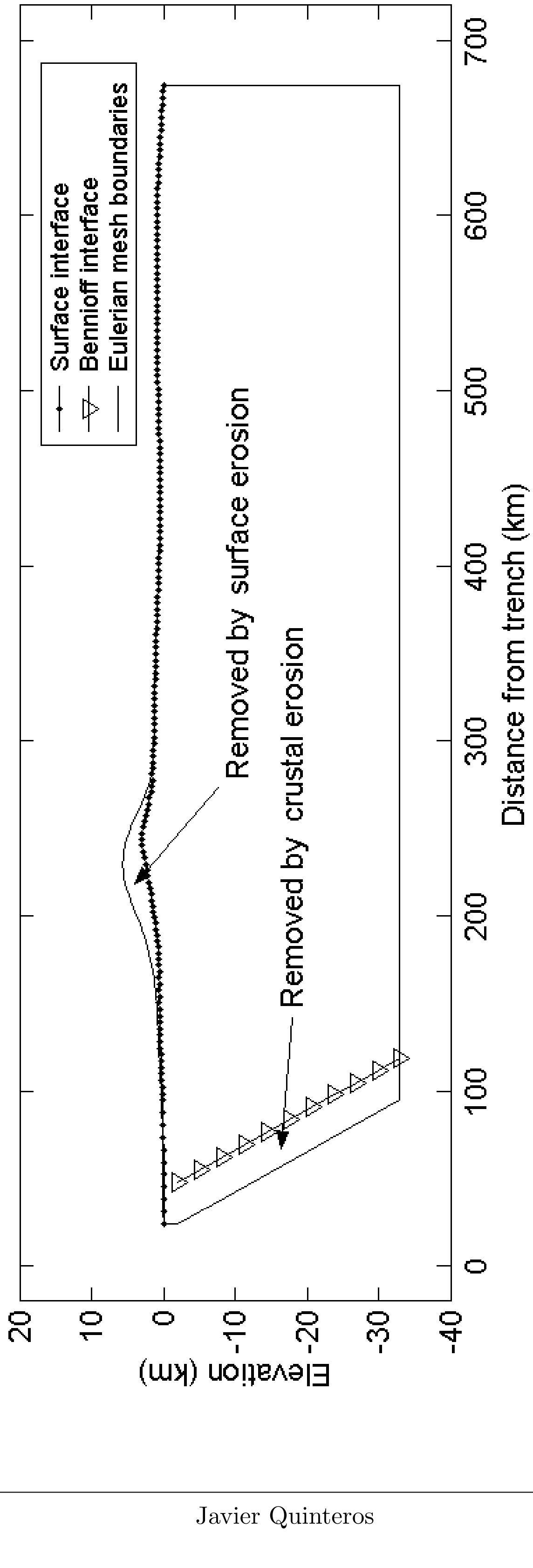

Figure 3.3: Interfaces defined in the model to represent the surface and the Benioff zone.

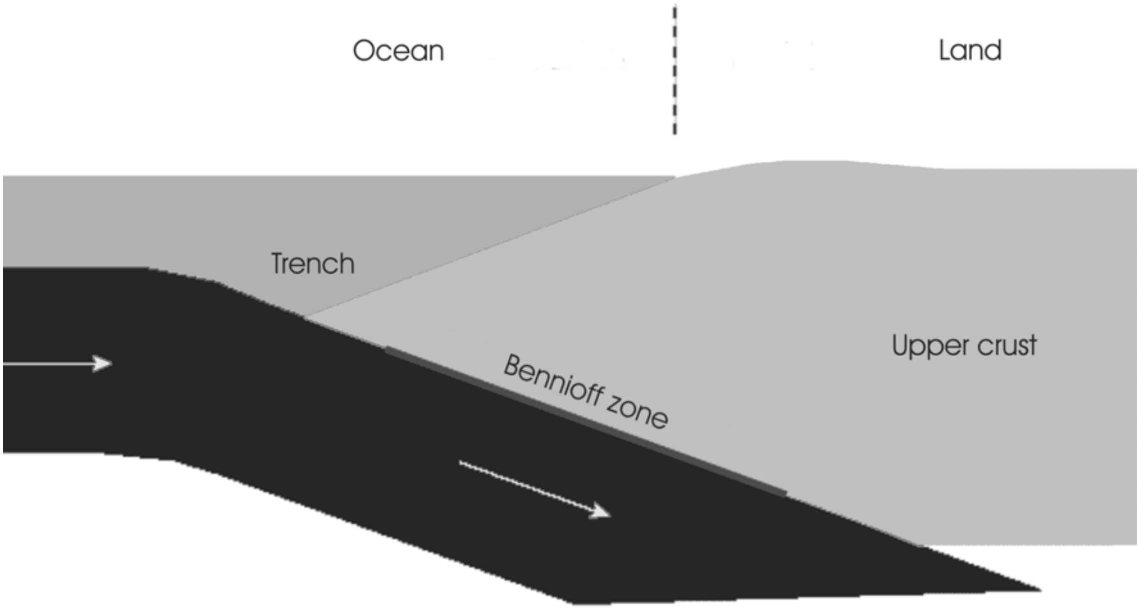

Figure 3.4: Schematic graphic of a subduction zone. After Brooks et al. (2003).

tectonic deformation and the erosion produced by the precipitation. This divides the material that has been eroded, and should actually be considered out of the domain, from the one that is still part of the crust.

- a Benioff interface, that separates the crust removed by subduction erosion from the remaining one.

Both interfaces are defined by several particles (an arbitrary number) whose movement through time is interpolated from the velocities calculated in the procedure defined in table 3.2 or from predefined velocities known from geological evidences.

The surface interface is defined at the beginning of the model in the same position as the upper limit of the domain. The Benioff interface is defined as the western limit of the domain (Fig. 3.4). The model keeps record of the element to which every point of the interfaces belongs. Once the velocity of each Eulerian node is calculated, we check whether the point still belongs to the same element by means of the inverse of the affine transformation employed in the element matrix calculation step. Otherwise, we find to which element the point has moved.

Later, in the case of the surface interface, the velocity of the interface point (v_p) is calculated interpolating the velocities from the four corner nodes (v_i) of the element using the shape functions (h_i) of a 4-node quadrilateral element (equation 3.24), namely

$$v_p = \sum_{i=1}^{4} h_i.v_i. \tag{3.24}$$

After that, the amount of erosion is calculated for every point (see Section 3.3.2) in the interface and its position corrected.

Both interfaces will be fully inside the domain in a few time steps because of the acting erosion processes. That means that there will be material that has been eroded but it is still part of the domain. Different numerical treatments need to be implemented for the material eroded by precipitation and subduction.

At every Gauss point that belongs to material removed by precipitation, two things have to be addressed when the stiffness matrix is assembled: it should have zero density

$$\rho_{rem} = 0 \tag{3.25}$$

and a fictitious viscosity several orders of magnitude lower than the minimum value found in natural conditions

$$\mu_{rem} << \min(\mu). \tag{3.26}$$

This way, the material can be numerically *removed*, ensuring that the results are in accordance with the actual mechanical situation. Namely, the eroded material does not add fictitious weight and shows almost no resistance to deformation.

In the case of the Benioff interface, tracking is not done based on the velocities resulting from the FEM calculations, because the velocity of the interface is known *a priori*. It moves with a constant horizontal velocity that has been determined by previous studies based on geological evidence[2]. This velocity is obviously greater than the boundary condition imposed by the subduction compression over the contact with the oceanic slab.

All the material eroded (located to the left of the Benioff interface) is considered to be *rigid* material. Rigidity is approached by assigning viscosity values several orders of magnitude greater than the maximum found in natural conditions

$$\mu_{rem} >> \max(\mu) \tag{3.27}$$

so the boundary conditions can *bypass* the material and be virtually imposed at the Benioff interface.

The time tracking of the problem is treated through the deformation of the mesh at each time step (table 3.1), based on the velocities calculation. The mesh is checked before any calculation in case that an element has been affected by a large deformation that makes it ill-suited for the numeric resolution, although that never happened in the experiments of this thesis. Basically due to the boundary conditions employed and the mesh resolution.

3.3.2 Erosion model

In addition to the tectonic processes, the topography is modified by erosion in different ways. Wind erosion and landslides can be considered as short range processes (Flemings and Jordan, 1989) while precipitation and the establishment of a natural drainage are long range processes. As the main objective is to develop a coarse large-scale evolution of the topography, the erosion due to precipitation was considered a first order approximation to the surface acting processes.

In order to estimate the erosion rate, the analysis is focused in three factors that favour erosion efficiency: millimeters of rain precipitated (R), altitude (h) and slope (sl). Howard and Kerby (1983) proposed a quantitative erosion law, based on empirical

[2] A deeper explanation on the velocity of this interface is given in the beginning of chapter 6.

results, that includes all these factors. Recently, Willett (1999a) expressed that the linear form of this law is able to capture the most important physical processes and provides the feedback mechanisms between orogen growth and erosion. In this way, erosion rate (k) could be expressed as

$$k(x) = R(x).h(x).sl(x). \tag{3.28}$$

An initial atmospheric water (vapour) flux (S_w) is considered to be transported by the humid winds from the west (Beaumont et al., 1992). Elevation determines how much of the available water is precipitated at every point, namely

$$R(x) = \left(\frac{h(x)}{hs} + mpc\right)^2 . \frac{S_w(x)}{aps}. \tag{3.29}$$

Appropriate values for the different parameters (hs, mpc, aps) were calibrated taking into account present-day topography and precipitation distribution.

Surface slope ($sl(x)$) is included as a factor in equation 3.28 because is supposed to determine the effectiveness of the erosion in a linear way (Willett, 1999a).

After that, the water precipitated, taking into account the distance to the next node (c_L), is discounted from the total water flux (equation 3.30) and the latter is moved towards the east.

$$S_w(x+1) = S_w(x) - R(x).c_L(x) \tag{3.30}$$

The complete algorithm can be seen in table 3.3.

3.3.3 Isostatic compensation model

The behaviour of the lithosphere under conditions of tectonic uplift is similar to the behaviour of a beam under load. Whenever a mountain rises, the deflection of the lithosphere occurs because of tectonic stacking of the crust that produces relief and consequent extra weight (Turcotte and Schubert, 1982). It is known that lithosphere is in a state of equilibrium whenever it is at sea level height, which means that its thickness is about 33 km (Allen and Allen, 1990). More (or less) than 33 km of thickness must be

procedure PRECIPITATION(initwater)
  $S_w(1) \leftarrow$ initwater ▷ Initialize available water
  for $x \leftarrow 2,$ interfacenodes **do**
    $R(x) \leftarrow \left(\frac{h(x)}{hs} + mpc\right)^2 . \frac{S_w(x-1)}{aps}$ ▷ Calculate precipitation
    if $R(x) < 0$ **then**
      $R(x) \leftarrow 0$ ▷ Precipitation cannot be negative
    end if
    $S_w(x) = S_w(x-1) - R(x).\,[pos(x) - pos(x-1)]$ ▷ Discount water precipitated
  end for
end procedure

Table 3.3: Algorithm to calculate the precipitation distribution considering the topography of the orogen.

compensated, which means that it will bend until the system reaches equilibrium again.

The mechanical behaviour of a beam can be expressed by means of the Timoshenko's theory. Under this theory, a section of the beam that is initially normal to the neutral plane, remains as a plane and with the same length after deformation. Because of the shear deformations, this section does not remain normal to the neutral axis. Then, the total rotation of the plane (β) is given by the rotation of the tangent to the neutral axis ($\frac{\partial w}{\partial x}$) and the shear deformation (γ), namely

$$\beta = \frac{\partial w}{\partial x} - \gamma \tag{3.31}$$

being w the vertical deflection.

The deformation of a cross section of the beam and the different angles of equation 3.31 can be seen in figure 3.5.

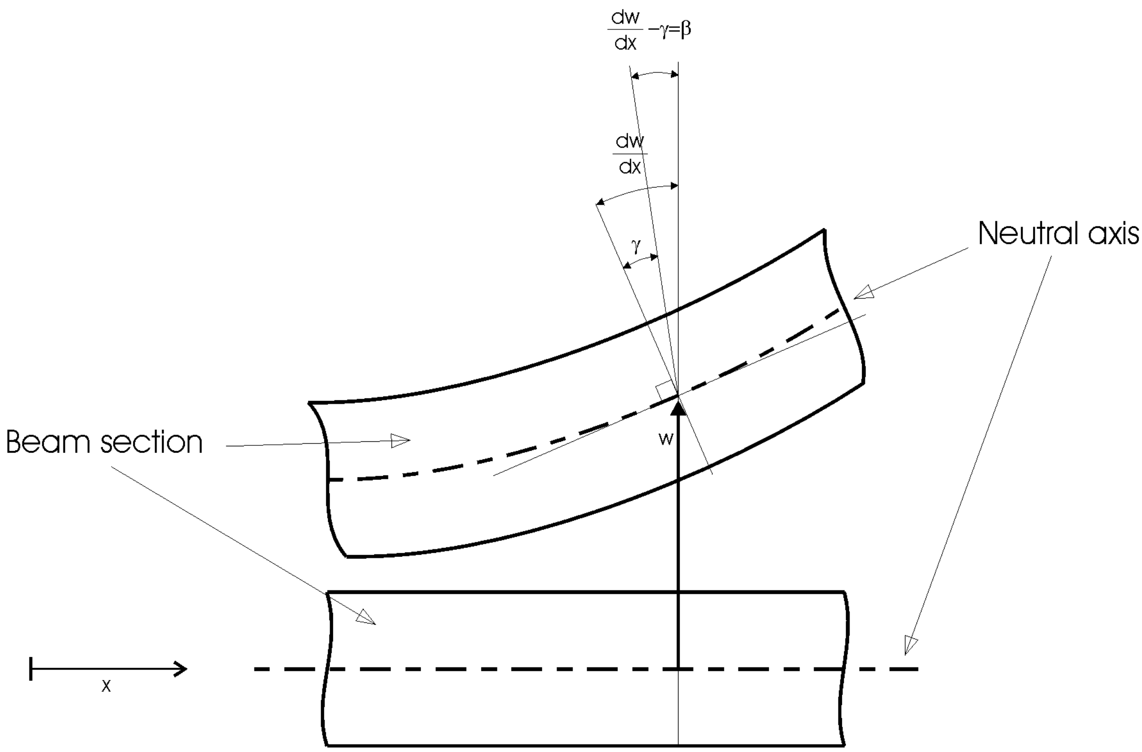

Figure 3.5: Deformation of a beam cross section. Modified from Bathe (1996).

The deflection of a beam can be expressed as

$$D.\frac{\partial^4 w}{\partial x^4} + P.\frac{\partial^2 w}{\partial x^2} = q(x), \tag{3.32}$$

where D is the flexural rigidity, P the horizontal forces exerted on the plate and $q(x)$ the load applied. Anyway, for this type of geodynamical problems, horizontal forces are usually considered to be negligible ($P = 0$) (Allen and Allen, 1990), so the second term of the equation is discarded, namely

$$D.\frac{\partial^4 w}{\partial x^4} = q(x). \tag{3.33}$$

Finite element approach

In the way the problem is posed, and under the assumptions of the Timoshenko's beam theory, the following variational formula can be derived from the virtual work principle (equation 3.6):

$$E.I \int_0^L \left(\frac{\partial \beta}{\partial x}\right) . \delta \left(\frac{\partial \beta}{\partial x}\right) \partial x + \kappa.G.A \int_0^L \left(\frac{\partial w}{\partial x} - \beta\right) . \delta \left(\frac{\partial w}{\partial x} - \beta\right) \partial V - \int_0^L p.\delta w + m.\delta\beta\partial x = 0 \tag{3.34}$$

where E is the Young's modulus, G is the shear modulus, A is the area of the yz cross section, p and m are the transverse and moment loading per unit length respectively and $\kappa = \frac{5}{6}$ is a shear correction factor based on equating the shear strain energy yield by the constant shearing stress across the section and the actual shearing stress (Crandall et al., 1978).

Displacements and rotations vector is defined as

$$U^T = [w_1, w_2, \ldots, w_N, \beta_1, \ldots, \beta_N] \tag{3.35}$$

where w_i is a displacement associated with vertical deflection of node i, β_i is the rotation at the node and N is the number of nodes.

Then, all the usual isoparametric formulations are employed in order to interpolate, namely

$$w = H_w.U, \tag{3.36}$$
$$\frac{\partial w}{\partial x} = B_w.U, \tag{3.37}$$
$$\beta = H_\beta.U, \tag{3.38}$$
$$\frac{\partial \beta}{\partial x} = B_\beta.U. \tag{3.39}$$

Replacing into equation 3.34 and after some algebraic steps, we get

$$\left[E.I \int_0^L B_\beta^T B_\beta \partial x + G.A.\kappa \int_0^L (B_w - H_\beta)^T (B_w - H_\beta) \partial x\right] .U = \int_0^L H_w^T p \partial x + \int_0^L H_\beta^T m \partial x. \tag{3.40}$$

The system of equations can be expressed as

$$K.U = R \tag{3.41}$$

where

$$\begin{aligned} K &= E.I \int_0^L B_\beta^T B_\beta \partial x + G.A.\kappa \int_0^L (B_w - H_\beta)^T (B_w - H_\beta) \partial x, & (3.42) \\ R &= \int_0^L H_w^T p \partial x + \int_0^L H_\beta^T m \partial x, & (3.43) \end{aligned}$$

and where the terms of K are related to flexure and shear stress respectively.

But in the context of an elastic plate overlying a fluid-like mantle, there is one process that has to be included in the equation: the isostatic restoring force (buoyancy) (Turcotte and Schubert, 1982). When the material added as tectonic load above the crust causes the lithosphere to bend, material from the mantle is displaced beneath the crust. The resistance of the underlying mantle related to the load can be addressed including another term in the equation.

This way, the governing equation can be expressed as

$$D.\frac{\partial^4 w}{\partial x^4} + \Delta\rho g w = q(x), \tag{3.44}$$

where $\Delta\rho$ is the density contrast between the load (upper crust or sediments) and the upward restoring mantle and g is the acceleration of gravity.

So, K is modified in order to include this term in the system of equations, namely

$$K = E.I \int_0^L B_\beta^T B_\beta \partial x + G.A.\kappa \int_0^L (B_w - H_\beta)^T (B_w - H_\beta) \partial x + \int_0^L \Delta\rho.g.H_w \partial x. \tag{3.45}$$

One can see in figure 3.6 an example of the resulting deflection of a 1-D Timoshenko's beam under load calculated by means of the modified equation presented in this section. Note the presence of a *forebulge* as a result of the acting restoring forces.

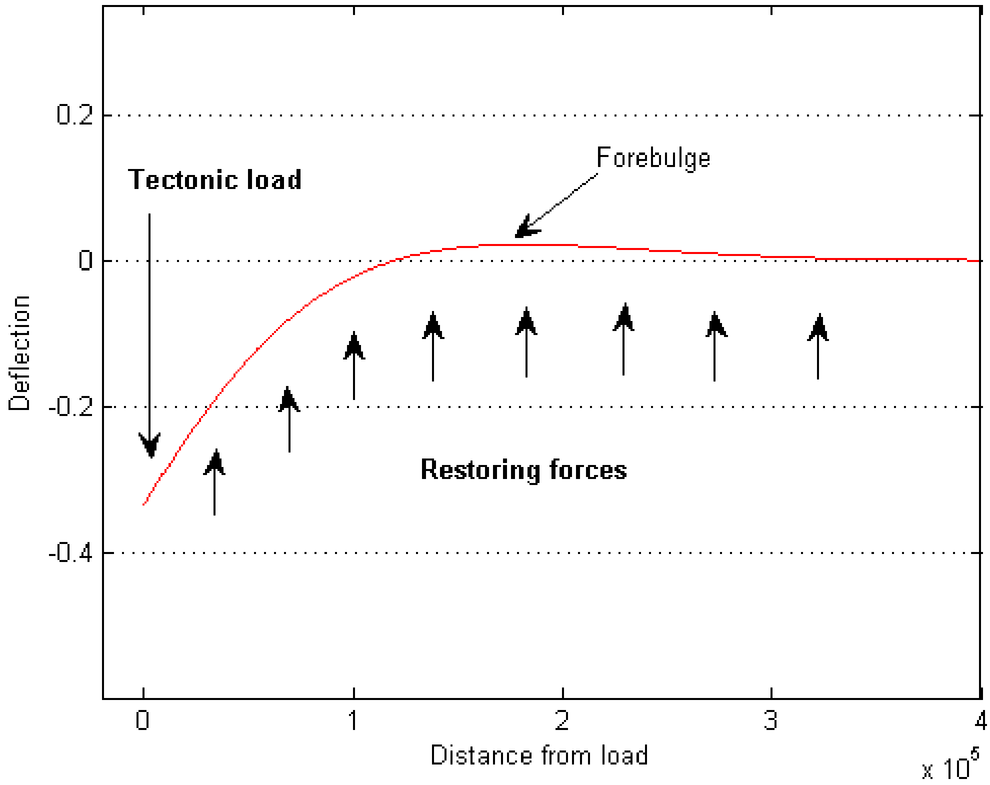

Figure 3.6: Example of a 1-D Timoshenko's beam deflection calculated with the extra term representing the restoring forces. After Ghiglione et al. (2005).

From the beam to the crust

The continental lithosphere is considered as a beam whose deflection under a certain load can be described by equation 3.44. As the lithosphere is in a state of equilibrium when its thickness is approximately 33 km, the tectonic load will be considered as the real thickness of the lithosphere minus the thickness of equilibrium state (33 km) (Allen and Allen, 1990).

Finding the correct flexural rigidity parameter (D) is not trivial and is a specific issue that must be addressed. In many cases, the lithosphere is not completely homogeneous and there can be zones of weakness due to temperature anomalies or to the history of the crust, among other factors. In this case, the temperature is considered to be the most important factor. It is known that the higher the thermal flux, the weaker the zone is, which results in a locally compensated load (Burov and Diament, 1995).

These variations are treated through the correct setup of the effective elastic thickness (T_e). Geodynamic researchers agree that this is not the real depth of the crust but a *mechanical* property related to its behaviour when loaded (Burov and Diament, 1995). It is the depth that must be used in order to calculate the deflection because it reflects the strength of the crust.

In this direction, we follow the guidelines of previous works (see for instance Karner et al., 1983) that establish that the effective elastic thickness of the lithosphere is the depth at which the isotherm of $450°C$ is located. This way, flexural rigidity (D) can be expressed as

$$D = \frac{E.a.T_e^3}{12}, \tag{3.46}$$

where T_e is the effective elastic thickness an a is the width of the beam. So, in warmer zones, the isotherm is near the surface, T_e is smaller and the beam is weaker.

At each time step, the deflection of the base of the upper crust is calculated by defining a 1-D beam with the same length as the lower boundary of the domain. The beam is considered to have neither deflection nor rotation at both boundaries. The load is calculated from the tectonic model topography. The density difference between the load applied and the material displaced by the deflection is calculated taking into account how much of the deflection is filled. Namely, the density considered for the load is proportional to the infill of the deflection.

Once the deflection is calculated for the nodes of the beam, only the incremental deflection, considering the previous time step, is added to the vertical component of the tectonic velocity for each node in the domain.

Once the section is compensated, the position of the nodes over the bottom boundary of the domain is saved in order to be used in the next time step. Later, for the tectonic model, the boundary is considered to have the same shape (straight) of figure 3.1.

An example of the topography calculated by the tectonic model and the resulting

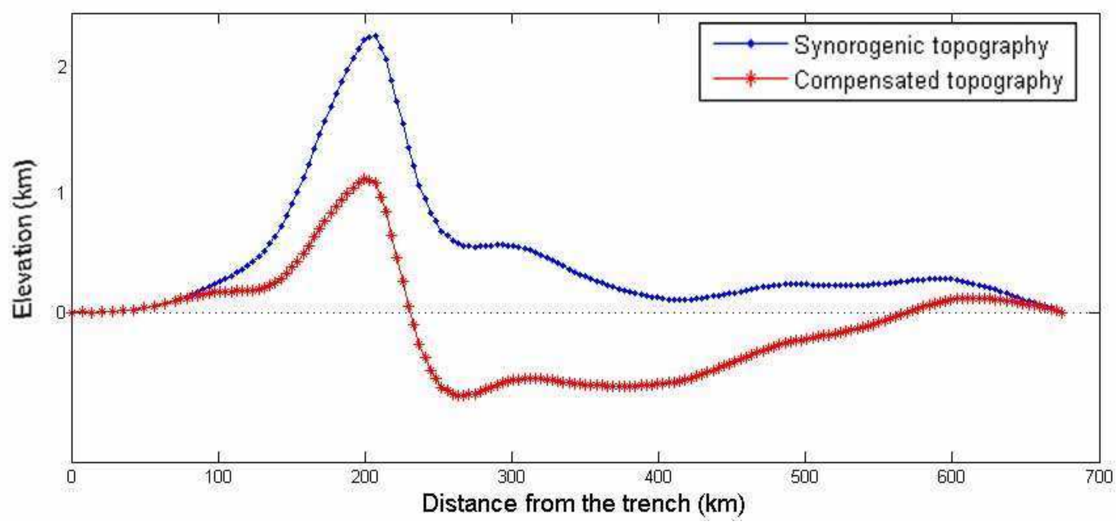

Figure 3.7: Example of topography calculated by tectonic stresses before and after the isostatic compensation.

topography after the compensation is shown in figure 3.7.

3.4 Other considerations

The model described in this chapter was designed during the first two years of research and development of the PhD activities. It was programmed in MATLAB, an interpreted programming language that allowed the codification of an early prototype. This was later enhanced and real cases were simulated.

Some important and satisfactory results about the evolution of the Patagonian Andes during the Miocene were obtained by means of this model and are shown in chapter 6.

Naturalmente, las cuatro operaciones de sumar, restar, multiplicar y dividir eran imposibles. Las piedras se negaban a la aritmética [...] Al manejar las piedras que destruyen la ciencia matemática, pensé más de una vez en aquellas piedras del griego que fueron los primeros guarismos y que han legado a tantos idiomas la palabra "cálculo". Las matemáticas, me dije, tienen su origen y a hora su fin en las piedras. Si Pitágoras hubiera operado con éstas...

Jorge Luis Borges, La rosa de Paracelso (La memoria de Shakespeare - 1983)

4

Final formulation by means of a solids deformation approach

Many different processes can affect the evolution of an orogen like an Andean System. The influence of each process can vary depending on the spatial or time scale that is studied. Orogen scale deformation encompasses extensions up to hundreds of kilometers deep and wide.

In this chapter, a novel numerical model based on solid deformation is presented. This model can simulate the tectonic evolution of the crust and the (lithospheric and asthenospheric) mantle under different conditions. Its mechanical behaviour is modelled by means of the finite element method (FEM) in order to solve the equations that define it. As a Lagrangian approach is employed, a remeshing technique is implemented to avoid distortion problems when a certain deformation threshold is reached. Some mineralogical changes that rocks can suffer due to high pressure and temperature conditions are also included in the model.

The model is able to represent elastic, viscous and plastic behaviour inside the studied domain. Several test cases with known solutions were run to validate the different aspects of the model.

In chapter 6, a real example related to a "delamination" process and its consequences is studied. *Delamination* is a process that can take several million years and occurs at the base of the lower crust. However, its consequences can influence seriously the evolution of the topography. It should be remarked that at this very moment, the magnitude of the influence of delamination is still not known accurately.

4.1 Purpose of this model

In the last two decades, the development of models to reproduce the processes related to plate tectonics became a powerful tool to achieve a detailed understanding of geodynamics.

On one hand, the deformation and evolution of the very first kilometers of continental crust have been analyzed with satisfactory results by means of a lot of different techniques (see for instance Cristallini and Allmendinger, 2001, Strayer and Suppe, 2002). This type of modelling has a huge advantage associated with the possibility to compare the results with analog models and, sometimes, field work.

On the other hand, orogen or regional scale modelling should be constrained with other type of evidence, usually less trustworthy. Also, analog models are difficult to scale in order to reproduce the processes that occur at a depth of hundreds of kilometers, where the pressure and temperature conditions play an important role. In the last few years, magnetoteluric and seismic studies allowed a better knowledge of the crust and mantle features.

In the last decade, several researchers proposed variations of the model developed by Fullsack (1995) (see for instance Willett, 1999a, Pysklywec, 2001, Quinteros et al., 2006a), that is based mainly on fluid dynamics equations as an analogy to model the behaviour of the crust. An improved variant of this model was presented earlier in the previous chapter. However, new models tend to be based on equations that describe the behaviour of solids (Sobolev and Babeyko, 2005). The complexity of these models will be directly related to the number of processes that simulate and the necessary definition to capture the solution.

Through the development of the model presented in this chapter, an accurate tool for the analysis of the crust and mantle in the first hundreds of kilometers of depth under different conditions is provided. To achieve this, the model includes the main laws that describe the thermo-mechanical behaviour of the domain to be modelled.

4.2 Essentials of the model

The model presented in this chapter is able to predict the mechanical response of the crust and lithosphere under different conditions such as compression, extension or other cases where only the isostatic compensation is the triggering cause.

The different layers have very different mechanical behaviour, even between parts of the same material. In the upper part of crust, temperature and pressure are relatively low and that is the reason why the mechanical behaviour is driven by friction and fracture sliding. This type of behaviour is known as "brittle regime" and could be related to plastic behaviour.

Deeper, where pressure and temperature are higher, the material turns to a viscous behaviour that is called "ductile regime". Between these regions is located the "brittle-ductile transition", a zone with the highest component of elastic behaviour.

A conceptual representation of the rheological model can be seen in Fig. 4.1. The

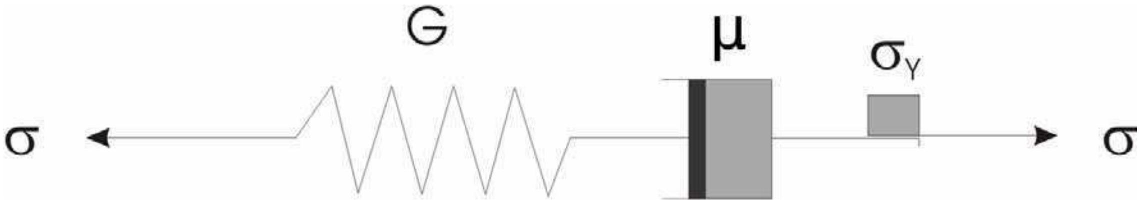

Figure 4.1: Conceptual representation of the elasto-visco-plastic model.

splitting of the deviatoric component of the strain rate can be expressed as

$$\dot{e} = \dot{e}^e + \dot{e}^v + \dot{e}^p = \frac{1}{2G}\hat{s} + \frac{1}{2\mu}s + \dot{\gamma}\frac{\partial g}{\partial s} \quad , \tag{4.1}$$

where s is the deviatoric part of the Cauchy stress tensor, G is the shear elastic modulus, μ is viscosity, $\dot{\gamma}$ is the plastic strain rate and g is the plastic potential function.

A stress threshold f is defined as

$$f = \|s\| - \sigma_Y(k) \quad , \tag{4.2}$$

where $\|(.)\|$ is the Euclidean norm and k is the accumulated plastic deformation. The plastic flow in this model is assumed to be associative and the plastic potential function is exactly the stress threshold ($g = f$). In case of plasticity $f = 0$.

The volumetric part is considered to be always purely elastic and the pressure can be expressed as

$$P = K\Phi \quad , \tag{4.3}$$

where K is the bulk elastic modulus and Φ is the volume change.

The Maxwell relaxation time is defined as

$$\tau_m = \frac{\mu}{G} \tag{4.4}$$

and the viscous stress relaxation coefficient since the last time step is

$$\alpha = \frac{1}{1 + \frac{\Delta t}{\tau_m}} \quad , \tag{4.5}$$

where Δt is the time step.

Also, the effective visco-elastic modulus is defined as

$$G^{ve} = \alpha G \quad . \tag{4.6}$$

In this way, the prediction-correction stress update algorithm can be expressed by means of

$$s_{n+1} = 2G^{ve}\Delta e_{n+1} + \alpha s_n - 2G^{ve}\Delta\gamma_{n+1}n_{n+1} \quad , \tag{4.7}$$

where s_{n+1} is the deviatoric stress at the $(n+1)-th$ time step, Δe_{n+1} is the strain increment at the $(n+1)-th$ time step and $\Delta\gamma_{n+1}$ is the effective plastic strain increment at the $(n+1)-th$ time step, which is defined as

$$\Delta\gamma_{n+1} = \frac{\|s^{pr}_{n+1} - \sigma_y\|}{2G^{ve}} \quad , \tag{4.8}$$

and where predicted visco-elastic stress is

$$s^{pr}_{n+1} = 2G^{ve}\Delta e_{n+1} + \alpha s_n \quad . \tag{4.9}$$

In order to achieve a high convergence rate of the Newton-Raphson algorithm, an appropriate stress update algorithm linearization is fundamental. In this model, a consistent tangential operator proposed by Simo and Taylor (1985) is employed. This is defined as

$$C^{tg}_{ijkl} = K\delta_{ij}\delta_{kl} + A\left[\frac{1}{2}\left(\delta_{ik}\delta_{jl} + \delta_{il}\delta_{jk}\right) - \frac{1}{3}\delta_{ij}\delta_{kl}\right] - B\left(n^{pr}_{n+1}\right)_{ij}\left(n^{pr}_{n+1}\right)_{kl} \quad , \tag{4.10}$$

where

$$A = 2G^{ve}\left(1 - \frac{G^{ve}\Delta\gamma_{n+1}}{\|s^{pr}_{n+1}\|}\right) \quad , \tag{4.11}$$

$$B = 2G^{ve}\left(\frac{G^{ve}}{G^{*}} - \frac{G^{ve}\Delta\gamma_{n+1}}{\|s^{pr}_{n+1}\|}\right) \quad . \tag{4.12}$$

4.2.1 Resolution algorithm

A simplified pseudo-code of the steps executed to achieve the resolution of the non-linear problem is shown in table 4.1. The stiffness matrix and the external forces vector are cleared at the beginning of each iteration. It should be remarked that only the values of the stiffness matrix are cleared but its structure is kept. This way, the next assemblage is drastically improved from a time performance point of view, avoiding all the time-consuming insert operations.

One can see that `calc_evp` is the only method related to the `Element` class that is invoked. There is no reference to the actual element implemented, neither in the pseudocode nor in the real code. This allows the replacement of the element employed without changing the code.

The structure of the stiffness matrix is directly associated with the connectivity of the mesh used. If the mesh is not refined, the structure will remain. Thus, the use of the internal buffer of the stiffness matrix is inhibited after the first assemblage, because as the structure is conserved there will be no insertions that need to be optimized.

Later, the final solution is obtained as the addition of the increments of every iteration. The increment is compared with a tolerance defined by the user to consider that convergence was achieved.

The pseudocode related to the `calc_evp` method from the `Element` class is shown in table 4.2. As a Lagrangian approach was adopted for the transient problem, an algorithm presented by Hughes and Winget (1980) is implemented to take into account the finite rotations of the material in the stress update algorithm. By this, the gradient G is defined as

```
procedure Non-linear resolution
    convergence ← false
    while not convergence do                                   ▷ Iterate until convergence is achieved
        K.blank(false)                                         ▷ Clear the stiffness matrix but keep the structure
        F.blank()                                              ▷ Clear the external forces vector
        for elem ← Elements.begin(), Elements.end() do         ▷ Iterate through all the elements
            winklernodes ← Nodes with Winkler conditions
            totdisp ← m_totU(mapping)                          ▷ Get the total displacement of the nodes in this time step up to last iteration
            K_e, F_e ← elem → calc_evp(totdisp, winklernodes)  ▷ Calculate the stiffness element matrix of the
                elasto-visco-plastic model
            Apply boundary conditions in K_e, F_e              ▷ B. C. in the element matrices
            K.Assemble2D(mapping, K_e)                         ▷ Assemble the element matrix into the global one
            F.Assemble1D(mapping, F_e)                         ▷ Assemble the element vector into the global one
        end for
        K.flush()                                              ▷ Flush the values stored in the buffer into the matrix
        U ← K.solve(F)
        K.useBuffer = false                                    ▷ Do not use the buffer in the next iteration because the structure is already set
        m_totU ← m_totU + U                                    ▷ Update the solution with the increment of this iteration
        if U.maxabs() < TOLERANCE then                         ▷ If the increment is smaller than a certain TOLERANCE
            convergence ← true
        end if
    end while
end procedure
```

Table 4.1: Simplified pseudocode to calculate the solution of the non-linear problem.

procedure CALC_EVP(totdisp, winklernodes)
  for $gp \leftarrow gps.begin(), gps.end()$ **do** ▷ Iterate through all the Gauss points
    if uniformGradient **then** ▷ If the element is based on an uniform gradient, it is the same for any Gauss point
      $grad \leftarrow unifgrad()$
    else
      $localstate \leftarrow$ State based on the node values
      $grad \leftarrow GradientInGausspoint(gp)$
    end if
    $G \leftarrow grad * totdisp$ ▷ Start the Hughes and Winget (1980) algorithm
    $\gamma = \frac{G+G^T}{2}$ ▷ Calculate strain increment
    $\omega = \frac{G-G^T}{2}$ ▷ Calculate rotation increment
    $Q = (I - \frac{\omega}{2})^{-1}(I + \frac{\omega}{2})$ ▷ Rotate stress from the previous time step
    $localstate \rightarrow devStress \leftarrow Q * localstate \rightarrow devStress * Q^T$
    $Pressure \leftarrow localstate \rightarrow Pressure + Properties.K * trace(\gamma)/3$ ▷ Calculate pressure
    $Stress \leftarrow 2 * localState \rightarrow Gm * onlyDeviat(\gamma) + localstate \rightarrow Alfa * localstate \rightarrow devStress$ ▷ Stress prediction
    if $Stress > PlasticYield$ **then** ▷ Check for plasticity
      $C \leftarrow$ Consistent tangential operator proposed by Simo and Taylor (1985)
      $Stress \leftarrow$ Correction due to plasticity
    end if
    $K_{gp}, F_{gp} \leftarrow eval\_evp(gp, Stress, Pressure, C)$ ▷ Evaluation in the Gauss point
    $K_e \leftarrow K_e + K_{gp} * gp.weight$
    $F_e \leftarrow F_e + F_{gp} * gp.weight$
  end for
  Apply Winkler conditions to K_e and F_e if necessary
    return K_e, F_e
end procedure

Table 4.2: Simplified pseudocode of the calc_evp method in the Element class.

$$G_{ij} = \frac{\partial \delta_i}{\partial y_j^{n+\frac{1}{2}}} \tag{4.13}$$

and strain (equation 4.14) and rotation increments (equation 4.15) can be defined in terms of G.

$$\gamma = \frac{G + G^T}{2} \tag{4.14}$$

$$\omega = \frac{G - G^T}{2} \ . \tag{4.15}$$

The following definition is proposed for integrating the constitutive equation:

$$\sigma^{n+1} = \bar{\sigma}^{n+1} + \Delta\sigma \tag{4.16}$$

where

$$\bar{\sigma}^{n+1} = Q\sigma^n Q^T \ , \tag{4.17}$$

$$Q = \left(I - \frac{\omega}{2}\right)^{-1} \left(I + \frac{\omega}{2}\right) \ , \tag{4.18}$$

I is the identity matrix and $\Delta\sigma$ is the stress increment.

Almost no reference can be seen about the type of element that is being employed. The call to the method `eval_evp`, that belongs to the class that actually implements the element, works as an interface that allows the rest of the algorithm to be defined in a generic way.

Finally, the method `eval_evp` only needs to specify the matrices multiplications and additions needed to calculate K_{gp} and F_{gp} taking into account the particular features of the element. In this case, one of the features that need to be addressed can be seen in table 4.3, where the Taylor expansion of the B matrix should be implemented and employed to calculate K_gp and F_gp.

procedure EVAL_EVP(gp, Stress, Pressure, C)
  $detJ, invJ \leftarrow invJacobian(gp)$ ▷ Calculate the determinant and inverse of Jacobian
  $Btaylor \leftarrow$ Gradient with Taylor expansion
  $K_gp \leftarrow Btaylor^T * C * Btaylor * detJ$ ▷ Calculate stiffness matrix
  $gravity \leftarrow \begin{bmatrix} 0 \\ -9.8182 * Properties.Density \end{bmatrix}$ ▷ Body forces
  $fullstress \leftarrow Stress + \begin{bmatrix} Pressure \\ Pressure \\ 0 \\ Pressure \end{bmatrix}$ ▷ Stress state of the material
  $F_gp \leftarrow \left(gp.H^T * gravity - Btaylor^T * fullstress\right)$ ▷ Load vector
    return K_gp, F_gp
end procedure

Table 4.3: Simplified pseudocode of the eval_evp method in the Liu class.

4.2.2 Material rheology

Numerous researchers have studied the behaviour of the rocks under different pressure and temperature conditions (see for instance Jaoul et al., 1984, Mackwell et al., 1998). The viscosity is usually considered to be dependant on many variables. Particularly, on the material rigidity coefficient (A), the strain rate ($\dot{\varepsilon}$), the temperature (T), the energy activation coefficient (Q) and a power law exponent (n) among others (equation 4.19). Some of these parameters will be seen in one of the cases described later in this chapter.

In this model, viscosity can be calculated in several ways, depending on the rheology that one would consider appropriate. One of the possible definitions of viscosity is

$$\mu = A^{-\frac{1}{n}}.\dot{\varepsilon_{II}}^{\frac{1-n}{n}}.e^{\frac{Q}{nRT}} \quad , \tag{4.19}$$

where $\dot{\varepsilon_{II}}$ is the square root of the second invariant of the strain rate and R is the gas universal constant (Tsenn and Carter, 1987).

Three different types of creep can be included in the definition of the rheology to be used in this model, following the approach of Kameyama et al. (1999). These are the three competing creep mechanisms that are usually related to olivine: diffusion, dislocation and Peierls creep. In this approach, at a given temperature and stress, the mechanism that produces the highest viscous strain rate becomes the dominant creep mechanism (Babeyko et al., 2006):

$$\dot{\varepsilon}^{(v)}_{eff} = \dot{\varepsilon}_d + \dot{\varepsilon}_n + \dot{\varepsilon}_p \ . \tag{4.20}$$

Diffusion creep is defined as

$$\dot{\varepsilon}_d = B_d \tau_{II} e^{-\frac{E_d}{RT}} \ , \tag{4.21}$$

dislocation, power-law creep as

$$\dot{\varepsilon}_n = B_n \tau_{II}^n e^{-\frac{E_n}{RT}} \ , \tag{4.22}$$

and Peierls creep as

$$\dot{\varepsilon}_p = B_p e^{\left[-\frac{E_p}{RT}\left(1-\frac{\tau_{II}}{\tau_p}\right)^q\right]} \ , \tag{4.23}$$

where τ_{II} is the square root of the second invariant of the stress tensor.

Later, effective viscosity can be calculated as

$$\mu = \frac{\tau_{II}}{2\dot{\varepsilon}^{(v)}_{eff}} \ . \tag{4.24}$$

Some of these creep mechanisms can be avoided by a proper setting of the input parameters (e.g. B_p, B_d and others).

To be consistent with the *brittle regime*, the shear stress at any point cannot exceed the maximum shear stress as a function of depth (σ_y) calculated by Byerlee (1978). This is expressed as

$$\sigma_y = \sigma_0 + \frac{\Phi - 1}{\Phi}.\rho g z \ , \tag{4.25}$$

where σ_0 is the cohesion strength, $\frac{\Phi-1}{\Phi}$ is the friction coefficient,

$$\Phi = \left[(1+\eta^2)^{\frac{1}{2}} - \eta\right]^{-2} \tag{4.26}$$

and

$$\eta = \tan(\theta) \quad , \tag{4.27}$$

denoted with θ the considered friction internal angle.

4.2.3 Details about the elemental formulation

To apply the finite element method, a two-dimensional, quadrilateral element with four nodes (NN = 4) proposed by Liu et al. (1994) was implemented. This element uses selective reduced integration to avoid the volumetric and shear locking and to reduce the computational time needed. To perform some sort of control over the *hourglass modes*, it defines a stabilization operator by means of the partial derivatives of the generalized strain rate vector related to the natural coordinates.

Shape functions (h) are defined as usual for a quadrilateral element with four nodes. Spatial coordinates (x) and also velocities (v) are approximated by the following linear combination

$$x_i = \sum_{a=1}^{\mathrm{NN}} h_a(r,s) x_{ia} \tag{4.28}$$

and

$$v_i = \sum_{a=1}^{\mathrm{NN}} h_a(r,s) v_{ia} \quad , \tag{4.29}$$

where subindex i represents the dimension and a is the element number.

The strain rate is expressed as

$$\dot{\varepsilon}(r,s) = \sum_{a=1}^{\mathrm{NN}} B_a(r,s) v_a \quad , \tag{4.30}$$

where B_a is the gradient matrix that contains the shape functions derivatives.

If $\dot{\varepsilon}$ is expanded in a Taylor series that is centered on the element natural coordinates (0,0)

$$\dot{\varepsilon}(r,s) = \dot{\varepsilon}(0,0) + \dot{\varepsilon}_{,r}(0,0)r + \dot{\varepsilon}_{,s}(0,0)s \quad , \tag{4.31}$$

it can be approximated by

$$\dot{\varepsilon}(r,s) = \sum_{a=1}^{\mathrm{NN}} \bar{B}_a(r,s)v_a \quad , \tag{4.32}$$

where

$$\bar{B}_a(r,s) = B_a(0,0) + B_{a,r}(0,0)r + B_{a,s}(0,0)s \quad . \tag{4.33}$$

To diminish the volumetric locking, selective reduced integration is applied (Hughes, 1980). $\bar{B}_a(r,s)$ is split into its deviatoric and volumetric part

$$\bar{B}_a(r,s) = \bar{B}_a^{vol}(0,0) + \bar{B}_a^{dev}(r,s) \quad . \tag{4.34}$$

The volumetric part of the matrix is evaluated only at (0,0) point to avoid volumetric locking. $\bar{B}_a^{dev}$ can be expanded as in equation 4.33, namely

$$\bar{B}_a(r,s) = B_a(0,0) + B_{a,r}^{dev}(0,0)r + B_{a,s}^{dev}(0,0)s \quad , \tag{4.35}$$

where $B_a(0,0)$ is the gradient matrix evaluated at (0,0) with both volumetric and deviatoric parts.

The elemental formulation asserts the diminishing of the volumetric locking, even if it is integrated at just one Gauss point. However, this is usually not enough in the case that a plastic deformation front should be accurately detected in an elasto-plastic problem. That is the main reason to integrate at two Gauss points:

$$\text{Point 1} : \left(+\frac{1}{\sqrt{3}}, +\frac{1}{\sqrt{3}}\right) \qquad \text{Point 2} : \left(-\frac{1}{\sqrt{3}}, -\frac{1}{\sqrt{3}}\right) \quad . \tag{4.36}$$

4.2.4 Thermal model

The viscosity of the material is one of the most important factors to take into account when calculating a mechanical response. And the temperature is one of the most important variables on which viscosity depends. Thus, a thermal model was implemented to calculate the temperature over the whole domain (Ω) by means of the Poisson thermal equation (4.37). Taking into account the material conductive capacity (κ) and the heat generation (q), it can be expressed as

$$\kappa \nabla^2 T = -q(x, y) \quad . \tag{4.37}$$

Starting from the following variational principle (Bathe, 1996)

$$\Phi = \int_{\Omega} \frac{1}{2} \kappa \left[\left(\frac{\partial T}{\partial x} \right)^2 + \left(\frac{\partial T}{\partial y} \right)^2 \right] - qT\partial\Omega - \int_{S_q} \hat{q} T \partial S_q \quad , \tag{4.38}$$

and after discretization, the following expression can be obtained

$$\sum_{e=1}^{NELEM} \int_{\Omega_e} B^T \kappa B \partial\Omega_e . U_T = \sum_{e=1}^{NELEM} \int_{\Omega_e} q H^T \partial\Omega_e + \sum_{e=1}^{NELEM} \int_{S_{q_e}} \hat{q} H^T \partial S_{q_e} \quad , \tag{4.39}$$

where H is the one-dimensional interpolating matrix that contains the element shape functions (see section 4.2.3), B is the gradient matrix related to the same shape functions, U_T is the nodal temperature vector and $\hat{q}$ is the thermal flux imposed on boundary S_q.

It is known that the crust produces heat due to a process called *radiogenic heating* and that this modifies the temperature patterns in the upper part of the lithosphere. Even if sometimes the thermal effects are not remarkable, slight modifications in temperature can cause (at a shallow depth) the reduction of viscosity. From a mechanical point of view, this fact will inhibit the material to store high levels of stress through the time steps due to the decreasing Maxwell relaxation time (equation 4.4) and thus, retarding the arrival to the plastic yield.

4.3 Remeshing

In a Lagrangian formulation, the mesh is distorted every time step due to the deformation of the studied body. When the body accumulates too much deformation over a few elements, numerical issues may arise.

4.3.1 Node relocation

The main problem when calculating on a distorted mesh is the slow (or absence of) convergence. In this case, a new mesh without deformation should be generated. When boundaries are fixed and deformation is concentrated inside the body, the new mesh could be exactly the original one. This solution is optimum because it requires no computational time at all. However, this is not the general case in Lagrangian approaches to geological problems, where at least the boundary representing the topography is a stress free surface.

The position of the nodes in the boundary defines the domain; thus, these are considered to be *fixed* during the remeshing process. The internal nodes should be relocated in such a way that the elements are preferably not deformed.

A certain deformation threshold is defined, which is compared with the deformation of the elements at every time step. When the deformation for any element is above this threshold, the domain is remeshed.

A simple mesh is considered (e.g., the original mesh) and an appropriate mapping is defined to adapt it to the arbitrary positions of the boundary ($\partial\Omega$) nodes. The problem can be stated as

$$\Delta\phi = 0 \quad \text{in } \Omega \quad , \tag{4.40}$$

constrained by the Dirichlet conditions by which $\phi = x$ at $\partial\Omega$ and $\phi = y$ at $\partial\Omega$ (Carey and Oden, 1984).

A stiffness matrix (K) related to the Laplace equation is assembled with the original undeformed mesh. The pseudocode to accomplish this task can be seen in table 4.4.

```
procedure REMESHING MATRIX ASSEMBLAGE
    for elem ← Elements.begin(), Elements.end() do        ▷ Iterate through all the elements
        K_e ← elem → calc_laplace()    ▷ Calculate the stiffness element matrix for the Laplace equation
        Kremesh.Assemble2D(K_e)    ▷ Assemble the element matrix into the global one
    end for
    Kremesh.flush()    ▷ Flush the contents that could have remained in the buffer
    ofstream ofs( "mesh.evp")    ▷ Open a file to save the matrix in order to save memory
    Kremesh.Save(ofs)    ▷ Save the matrix
    ofs.close()    ▷ Close the file
end procedure
```

Table 4.4: Pseudocode to assemble the global stiffness matrix that describes the geometry of the mesh to be used in the resolution of the Laplace equation.

procedure REMESHING
    ifstream ifs("mesh.evp") ▷ Open the file with the stiffness matrix
    $Kremesh_x$(ifs) ▷ Loads the stiffness matrix into a variable to calculate the x coordinate
    $Kremesh_y = Kremesh_x$ ▷ and copy it into a variable to calculate the y coordinate
    Impose the Dirichlet boundary conditions on $Kremesh_x$, U_x and F_x
    Impose the Dirichlet boundary conditions on $Kremesh_y$, U_y and F_y
    $U_x \leftarrow Kremesh_x.solve(F_x)$
    $U_y \leftarrow Kremesh_y.solve(F_y)$
    Mapping() ▷ Map the state variables from the deformed mesh to the undeformed one
end procedure

Table 4.5: Pseudocode to solve the Laplace equation for both coordinates.

Later, when the deformation threshold is reached, the equation system is solved twice. Once for each coordinate (x and y) and in both cases with Dirichlet conditions (present position) for the degrees of freedom associated with the nodes on the boundary (see algorithm in table 4.5).

A simplified situation of a mesh after some time steps of deformation can be seen in figure 4.2.a. The resulting situation after the remeshing process is shown in figure 4.2.b.

4.3.2 Special cases

Usually, all the degrees of freedom associated with nodes over the boundary will be set as Dirichlet conditions, but for some special cases, if some of them are left free the remeshing process can be improved.

If we consider the case where the elements can experience some sort of slight *hourglass mode*, like the ones described in the previous section, a remesh process can enhance the

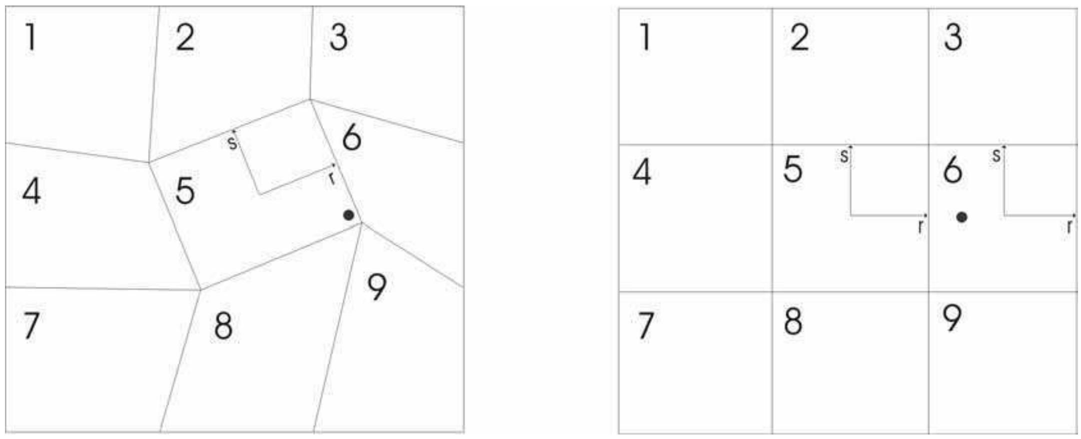

a) b)

Figure 4.2: Particle position before and after the remeshing process. a) Inside element 5 in the distorted mesh. b) Inside element 6 in the new undistorted mesh.

quality of the mesh where the deformation overpassed the threshold defined. However, due to the hourglassing, the deformation will also concentrate on the boundaries of the domain and, if all the degrees of freedom are set as Dirichlet conditions in the equation system, the artifact will accumulate until there is no way to further work with the distorted elements.

One can see in figure 4.3 how the hourglassing distorts the elements in the boundary. When the remeshing is applied the deformation of the element is distributed by means of the Laplace equation and the quality of the mesh improves. However, the width of the elements have changed and the new mesh will have half of the elements near the

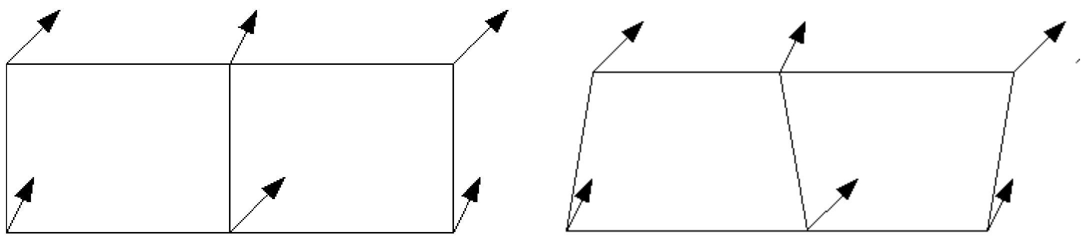

a) b)

Figure 4.3: Effect of the hourglass modes. The bottom part of the element is a domain boundary, while the upper side is considered to be *inside the domain*. a) Both elements are undeformed; b) Hourglassing shows as two crossed pairs of similar velocities.

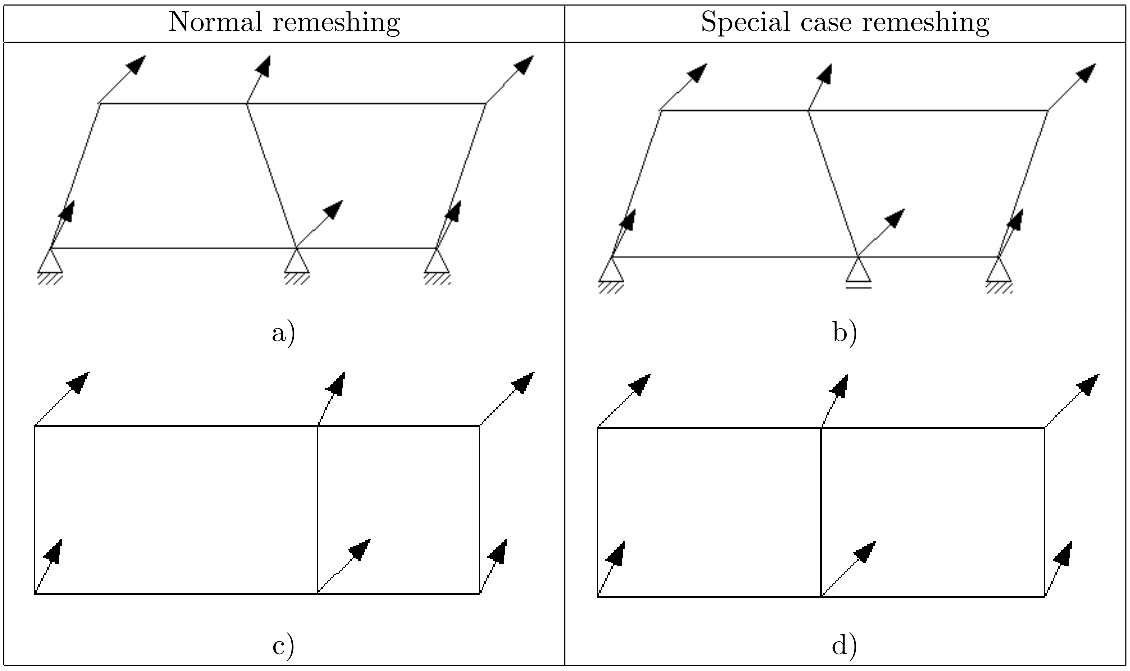

Figure 4.4: Two different ways to remesh. a) All the degrees of freedom are considered Dirichlet conditions; b) All the *vertical* degrees of freedom are considered Dirichlet conditions but only the leftmost and rightmost *horizontal* degrees of freedom are included in the Dirichlet conditions; c) Resulting remesh in the normal case. d) Remeshing to diminish hourglass effects.

boundary wider than the original ones and the other half narrower (figure 4.4.c).

A work-around to avoid this situation is to reduce the number of Dirichlet conditions. For these boundary nodes, if the coordinate y is constant, the coordinate x can be discarded from the Dirichlet conditions. Thus, the width of the elements will have exactly the same proportion among them as it was in the original mesh. In this case, the only two nodes of this boundary whose x coordinate should be set as Dirichlet conditions are the leftmost and the rightmost (figures 4.4.b and 4.4.d).

4.3.3 State mapping or translation

Another problem still exists after remeshing. All the variables that describe the state of the domain at a certain time step are associated with a node or element of the old mesh, a situation that is not valid in the new mesh. To deal with this problem, particles carrying information about all the variables that describe the domain state are incorporated. The state is reproduced by translating the information stored in the particles to each node and element of the new mesh (Harlow and Welch, 1965, Moresi et al., 2003).

The position of these particles is updated at every time step based on the displacements calculated by the finite element model. The shape functions h_n are evaluated at the particle position and multiplied by the nodal displacements. For example, in a four node element we can write

$$u_{i,p} = \sum_{n=1}^{4} h_n(r,s).x_{i,n} \quad , \tag{4.41}$$

where u is the displacement, i is the coordinate, n is the node number and p is the particle.

In the distorted mesh, each particle stores the information about the element to which it belongs. As in the new mesh, the element that contains the particle must be found, the old element is probably the best starting point to look for. An original algorithm based on the one proposed by Novoselov et al. (2002) was implemented. This way, the order of the search is reduced considerably.

To verify whether the particle belongs to a certain element, the inverse of the affine transform that is employed to translate from local *(r, s)* to global *(x, y)* coordinates is used. The particle is considered to be inside the element if

$$|r| <= 1 \quad \text{and} \quad |s| <= 1 \quad . \tag{4.42}$$

If the local coordinates of the particle are outside the element, the search algorithm uses the calculated coordinates to move towards the containing element.

In figure 4.2.a the position can be seen of a particle that, before the remeshing, belonged to element number 5. After remeshing, the new local coordinates related to element number 5 are calculated and, in this case, the variable r does not satisfy equation 4.42 (see figure 4.2.b). So, the neighbor element that shares the side associated with $r = 1$ condition is searched. This search requires almost no computational cost because of the nodes and elements connectivity list. It is quite difficult for the particle to be located far from the former element. To be stricter, there is a small probability that the new element is relocated far from its original position. A situation like this could happen if the mesh had suffered a great deformation, which is not probable considering the convergence needed. So, the number of particles that must be relocated at a distance greater than a few elements is completely marginal.

The amount of particles inside an element may vary due to this relocation. As the domain state in the new mesh is replicated exclusively by the particles, the number of particles inside an element cannot be under a defined threshold. To avoid this problematic situation, a new set of particles is inserted in case that an element contains less particles than the minimum threshold. The variables of the new particles are calculated based on the values of the existing ones.

A simplified version of the algorithm that maps the state variables from the particles to the new undistorted mesh is shown in table 4.6.

Figure 4.5 shows an example of the remeshing process and the mapping of a variable. There can be seen the stress and the mesh configuration at the time step when the

procedure MAPPING
  Check whether the state variables are stored in the elements or the nodes
  Iterate and clean all the stored states
  for $mark \leftarrow Markers.begin(), Markers.end()$ **do** ▷ Iterate through all the markers
    $reassign \leftarrow true$ ▷ Find the element that the marker belongs to
    while $reassign$ **do**
      $idN \leftarrow Elements[mark \rightarrow idElem].idNodes$

$$transf \leftarrow \begin{bmatrix} Nodes[idN[0]].x & Nodes[idN[0]].y & Nodes[idN[0]].x * Nodes[idN[0]].y & 1 \\ Nodes[idN[1]].x & Nodes[idN[1]].y & Nodes[idN[1]].x * Nodes[idN[1]].y & 1 \\ Nodes[idN[2]].x & Nodes[idN[2]].y & Nodes[idN[2]].x * Nodes[idN[2]].y & 1 \\ Nodes[idN[3]].x & Nodes[idN[3]].y & Nodes[idN[3]].x * Nodes[idN[3]].y & 1 \end{bmatrix}$$

$$a1 \leftarrow transf.inv() * \begin{bmatrix} 1 \\ -1 \\ -1 \\ 1 \end{bmatrix}$$

      $r \leftarrow a1(0) * mark \rightarrow x + a1(1) * mark \rightarrow y + a1(2) * mark \rightarrow x * mark \rightarrow y + a1(3) * 1$ ▷ Mapping from x to r

$$a2 \leftarrow transf.inv() * \begin{bmatrix} 1 \\ 1 \\ -1 \\ -1 \end{bmatrix}$$

      $s \leftarrow a2(0) * mark \rightarrow x + a2(1) * mark \rightarrow y + a2(2) * mark \rightarrow x * mark \rightarrow y + a2(3) * 1$ ▷ Mapping from y to s
      $reassign \leftarrow false$ ▷ We presume that it is located in the same element
      if $r > 1$ **then** ▷ If it is outside the element
        $mark \rightarrow idElem \leftarrow ?$ ▷ Find the element that shares local nodes 0 and 3
        $reassign \leftarrow true$ ▷ and try there in the next loop
      end if
      Do the same with the other three possibilities ($r < -1$; $s > 1$; $s < -1$)
      if Not $reassign$ **then** ▷ If we found the element
        Copy the properties of the marker to the proper element or node
      end if
    end while
  end for
end procedure

Table 4.6: Algorithm to map the state variables from the deformed mesh to the undeformed one.

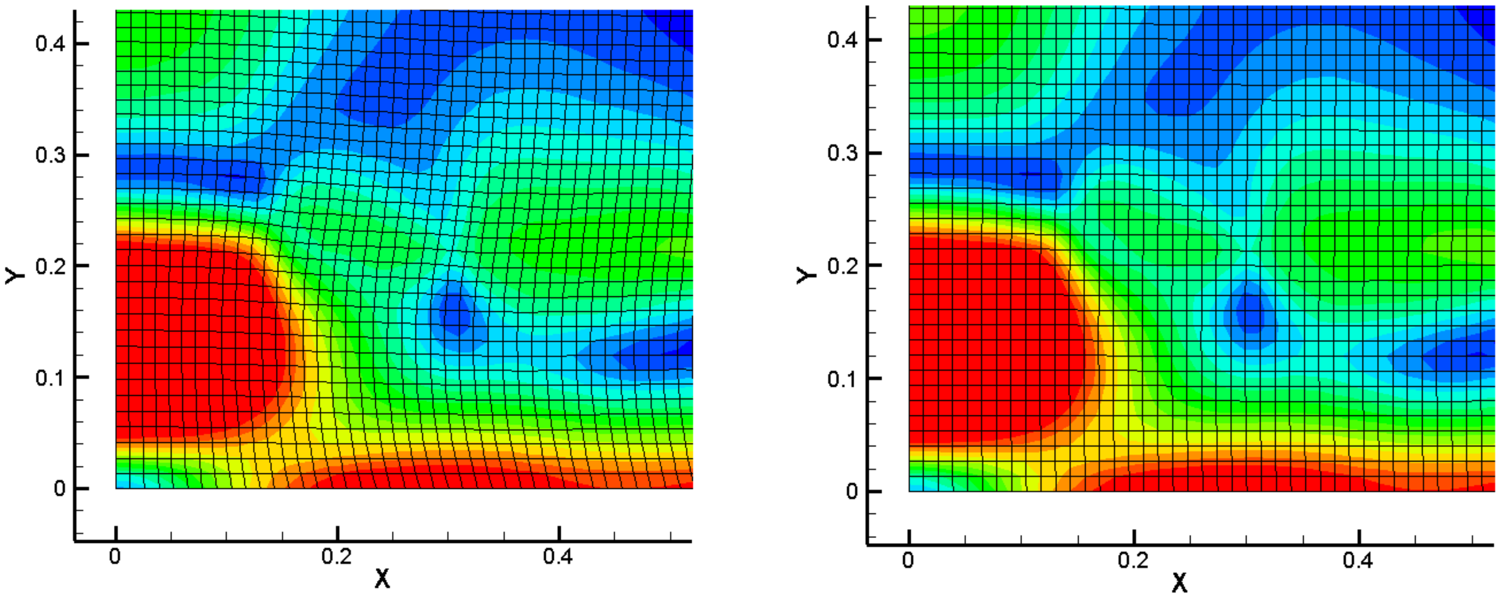

a) b)

Figure 4.5: Deviatoric stress state and mesh geometry in two consecutive time steps, (a) before and (b) after the remeshing.

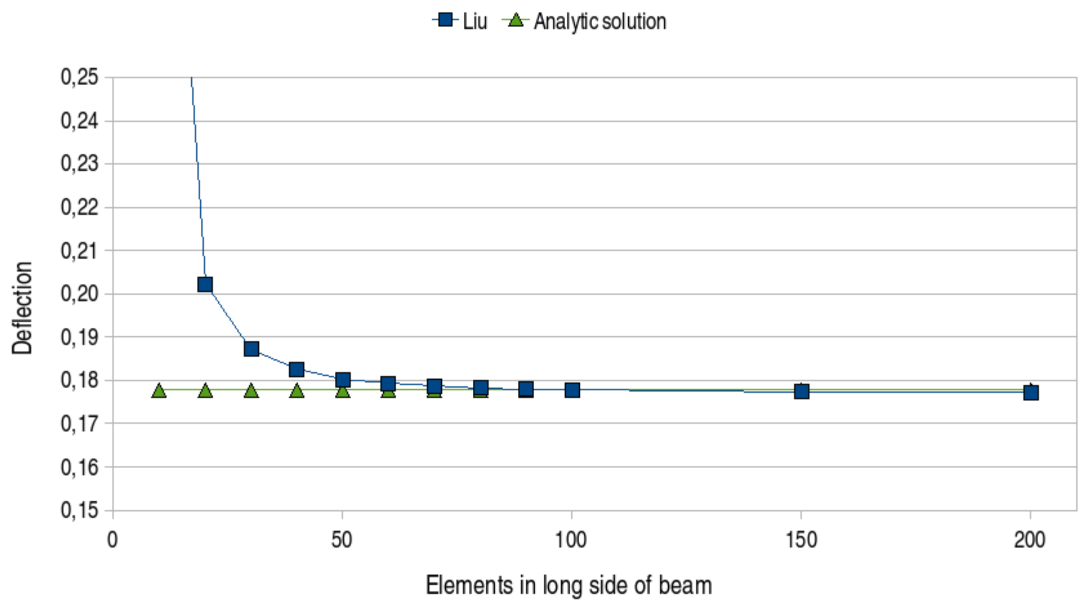

Figure 4.6: Convergence of the Liu element as a function of the number of elements on the long side of the beam.

remeshing is run and the next one.

4.4 Model validation

To validate the formulation and implementation of the model, a series of test cases with known results were run. In the following subsections, details are given about some of the cases that validate each behaviour mode simulated (elastic, viscous and plastic).

4.4.1 Clamped beam - Elasticity

Many test cases were run to validate the elastic behaviour. One of them is shown as an example.

A force is exerted over the right end of a horizontal beam that is clamped on its left end. One can see in figure 4.6 the analytical solution for a thin beam and the deflection calculated by the model as a function of the number of elements used on the long side of the domain. On the other figure (4.7), the deflection is shown as a function of the

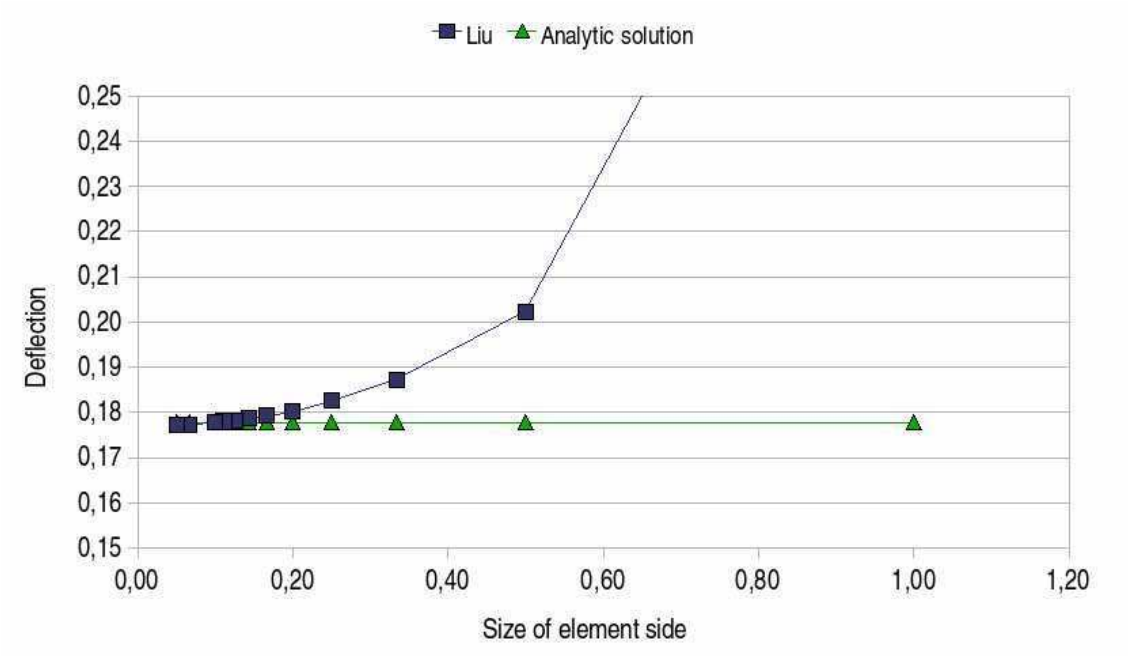

Figure 4.7: Convergence of the Liu element as a function of the length of the element.

length of the element.

4.4.2 Rayleigh-Taylor instability - Viscosity

The test case proposed by van Keken et al. (1997) was selected to validate the viscous behaviour. In this test, the evolution of a two-phase fluid that convects induced by gravity is tracked. The domain have bottom and upper boundaries of $0,9241$ m and left and right boundaries of 1 m. The two phases of the fluid have the same viscosity but different density ($\Delta\rho$). The lighter fluid (fluid 1) is on the bottom part of the domain and the denser one (fluid 2) is above. The limit between both fluids is located at 0.2 m from the bottom and with an initial deflection described by the expression

$$w = 0.02 \ \cos(\pi x/\lambda) \tag{4.43}$$

where λ is the width of the domain. A schematic view of the domain and the boundary conditions is shown in figure 4.8.

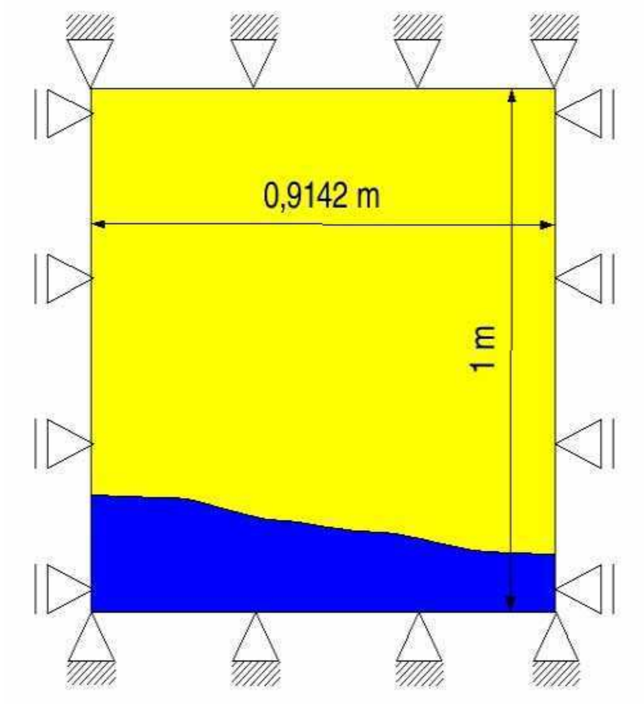

Figure 4.8: Schematic view of the boundary conditions for the test case analyzed by van Keken et al. (1997).

The specification of both fluids can be seen on the table 4.7.

Over the upper and bottom boundaries *non-slip* conditions are prescribed. Over the lateral walls vertical displacements are allowed but not horizontal ones (symmetric conditions). This way, the motion is strictly gravity driven. Gravity is considered to be 1m s^{-2}.

The evolution of the fluid can be seen in figure 4.9. Due to the contact geometry between both fluids, the left column in the domain is the lightest (figure 4.9.a). Thus, fluid number 1 starts uprising through this region, also favoured by the left boundary condition that implies no friction (figure 4.9.b). Fluid 1 increases its velocity as it goes up. However, due to the *non-slip* upper boundary condition, it stops the uprising and moves towards the right part slowly (figure 4.9.c). When the fluid reaches the right boundary, it stops completely (figure 4.9.d) and a smaller second column of ascendant fluid appears on the lower part of the right wall. The behaviour is similar to the first one.

Variable	Fluid 1	Fluid 2
Density (ρ)	1.3	1.0
Viscosity (μ)	1	1
Elastic Bulk modulus (K)	1000	1000
Elastic Shear modulus (G)	1000	1000
Cohesion strength (σ_0)	∞	∞
Gravity (g)	1	1

Table 4.7: Main features of the fluids from the isoviscous Rayleigh-Taylor instability problem.

When the second column reaches the top of the domain, it stops again and a downrising plume of fluid 2 appears in the center of the upper boundary (figure 4.9.f).

Different snapshots from the domain evolution that are shown in figure 4.9 were compared with the ones published by van Keken et al. (1997). The evolution shown in this chapter and in the vanKeken paper are identical for all the compared time steps. The only minor difference that could be found is located over the contact between both fluids near the bottom. This difference is explained by the uniform discretization performed previous to the simulation, that do not matched exactly the one proposed in equation 4.43.

It is very important to note that, due to the intense deformation that this case implies, not only the capability of the model to represent viscous behaviour is validated, but also the implementation of the remeshing algorithm.

4.4.3 Plastic deformation concentration - Plasticity

One of the aims when modelling plastic behaviour is to have a good localization of the plastic deformation. This means that the concentration of the plastic deformation when simulating fractures should not be wider than a couple of elements.

In this case, an isotropic solid is compressed. There is only one point of weakness,

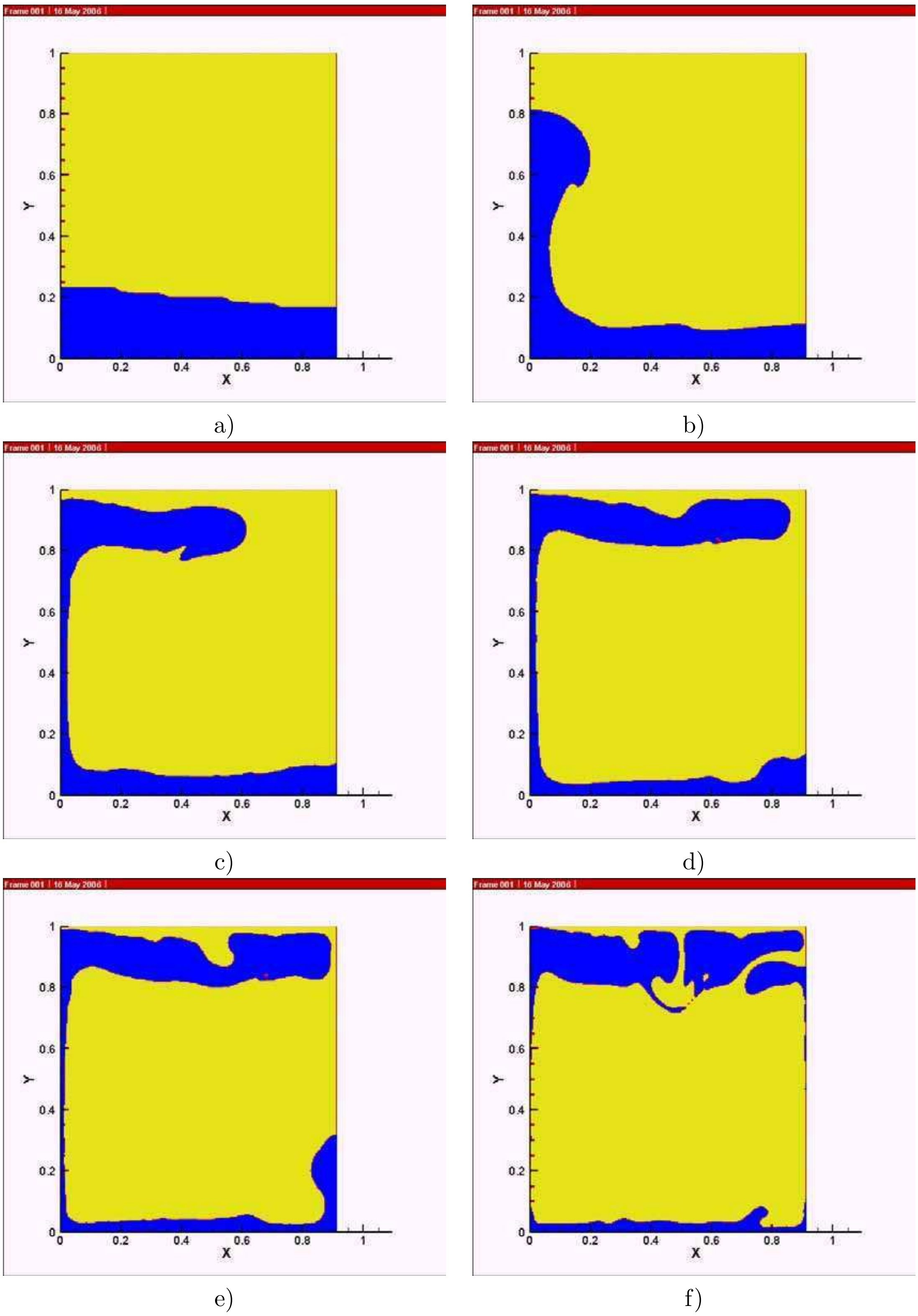

Figure 4.9: Validation of the viscous behaviour in the test case proposed by van Keken et al. (1997).

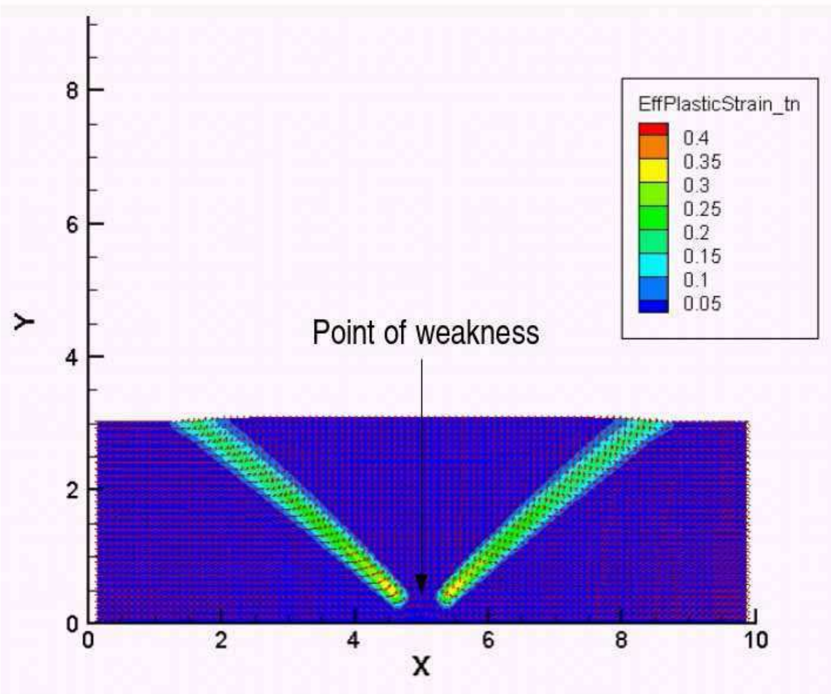

Figure 4.10: Plastic deformation concentration caused by compression in presence of a weakness point.

consisting of a few elements with a shear elastic modulus two orders of magnitude smaller than the rest of the domain. The remeshing algorithm was not run in order to verify that the plastic deformation would concentrate as expected.

The concentration of the deformation for the last time step is shown in figure 4.10. It can be seen that the deformation is completely concentrated over the two fractures and that this final configuration is composed of three rigid blocks with no internal deformation.

4.4.4 Stress profiles

When the crust and the lithosphere are modelled, it is important to assert a proper distribution of stress values. These values should be in agreement with the rheology of the materials belonging to the domain, the forces exerted over them and the temperature distribution, among others.

A domain 50 km deep and 500 km wide was considered. The upper crust is 25 km deep and is modeled as a wet quartzite (Gleason and Tullis, 1995). From 10 to 25 km the properties were *scaled* and the internal angle of friction was changed from 5° to 15°. The lower crust is 10 km deep and is modeled as a dry Maryland diabase (Mackwell et al., 1998). The lithospheric mantle is modeled by means of a *scaled* olivine flow law associated with a wet Aheim dunite (olivine) (Chopra and Paterson, 1984).

The domain is compressed at a constant velocity of 10 mm/yr, which gives the usual strain rates for an orogen like the Andes (10^{-14} - 10^{-16}). One can see in figure 4.11, the stress profile from the magmatic arc towards the foreland. The profiles start on the axis of the magmatic arc with an offset of 100 km each.

The stress pattern is in complete agreement with the one expected in a subduction zone. The bold arrows show the displacement of the material at each point belonging to a vertical profile. A big part of the uplift and tectonic shortening related to the compression is concentrated over the magmatic arc as it is expected.

The domain selected for this example and most of its features were published by Beaumont et al. (2006) in order to study the effects of crustal flow processes. Some parameters were modified in order to make it suitable for subduction zones. All the parameters used are shown in table 4.8.

4.5 Other considerations

After the experience of developing the model based on Stokes equations, it was clear that even if the MATLAB programming language were oriented to a rapid development of the application, the scalability was limited. The solutions obtained were difficult to refine due to the time needed to solve the problems. It was necessary to migrate the code to a more appropriate language that could run faster, manage memory in a more flexible way or even be run in a cluster environment if necessary.

Due to these limitations, the programming language employed to code this model was C++. The code was thoroughly tested in order to include as many optimizations

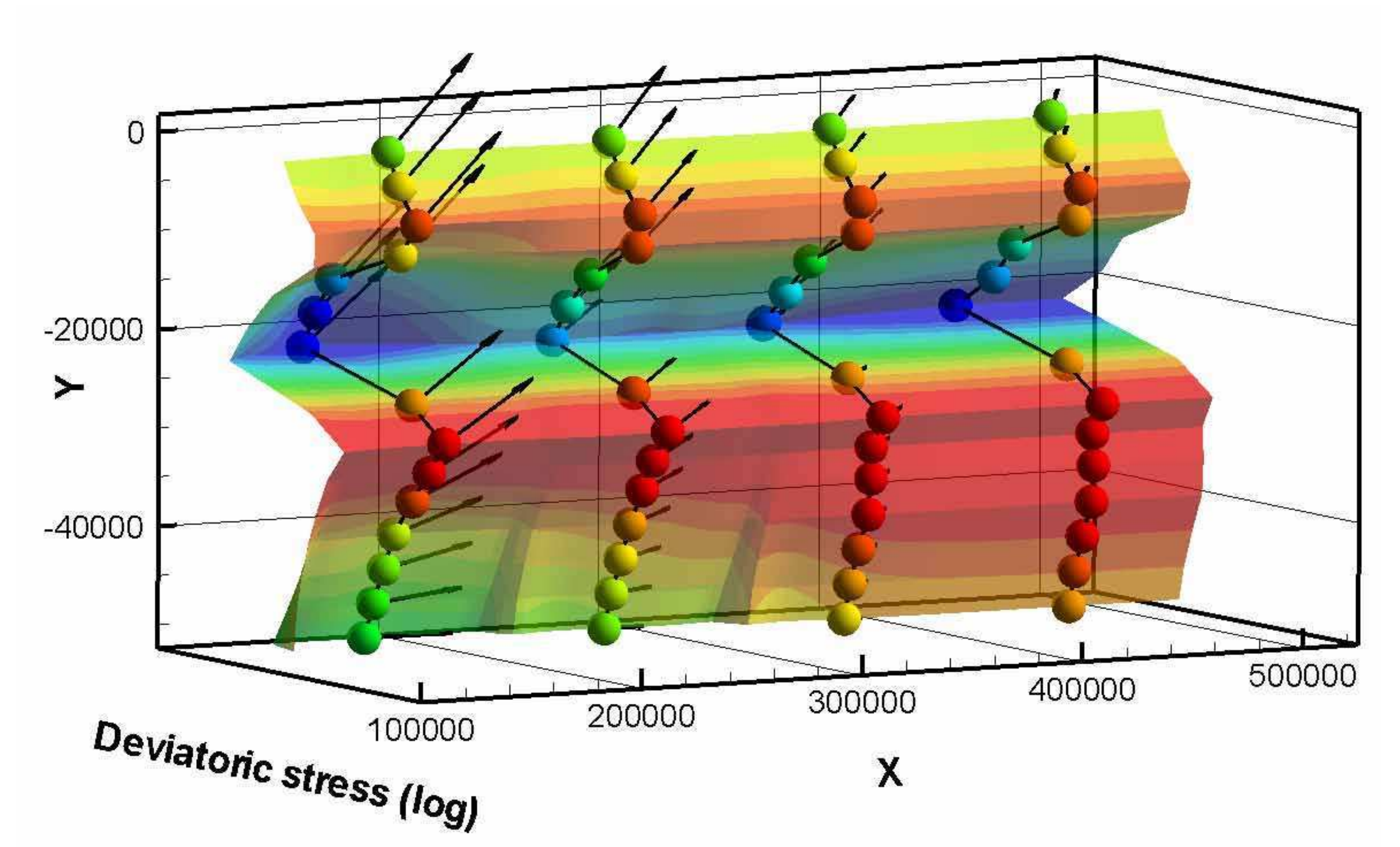

Figure 4.11: Distribution of stress and displacement every 100 km from the magmatic arc towards the foreland. The lithosphere is composed of upper crust, lower crust and lithospheric mantle.

Parameter	1	2	3	4
ρ / Density (kg m^{-3})	2700	2700	2900	3300
K / Bulk elastic Modulus (GPa)	55	55	55	122
G / Shear elastic modulus (GPa)	36	36	36	74
A / Material rigidity (MPa^{-1} s^{-1})	$1.4 * 10^{-26}$	$6.9 * 10^{-26}$	$1.5 * 10^{-25}$	$10^{-14.3}$
Q / Molar strength activ. (kJ mol^{-1})	223	223	485	515
n / Power law exponent	4.0	4.0	4.7	3.5
$\dot{\varepsilon_o}$ / Reference strain rate (s^{-1})	10^{-15}			
σ_0 / Cohesion strength (MPa)	10	10	10	40
Θ / Internal friction angle (°)	5	15	15	30
Δt / Time step (years)	10^3			
R / Gas universal const.(J mol^{-1} K^{-1})	8.3144			
κ / Heat conductivity (W/K/m)	2.0	2.0	2.5	3.3
q / Heat productivity (μW m^{-3})	2.0	2.0	0.75	

Table 4.8: Model parameters to calculate the stress profiles. 1) Upper crust (0-10 km); 2) Upper crust (10-25 km); 3) Lower crust; 4) Lithospheric mantle. After Beaumont et al. (2006).

as possible and to avoid memory leaks that could compromise the simulation of large domains during many time steps.

The code was actually implemented over a more general-purpose framework (presented in the next chapter) designed to solve problems related to partial differential equations by means of the finite element method.

A real geological example (a delamination process) simulated by means of the model presented here is shown in chapter 6.

This paper describes in detail a new technique for the numerical solution of problems in the dynamics of an incompressible fluid for a free surface. The method has been developed for use on ***a high-speed electronic computer*** *and would be* ***impractical for hand-solution purposes****...*

Harlow and Welch (1965)

5

Finite element method implementation

The design of a numerical model goes through different stages until it can be considered functional and satisfactory results are obtained. A correct formulation of the problem is needed for numerical models based on the finite element method in order to assess, from a mathematical point of view, that a proper solution will be obtained. The equations, their discretization and the element employed are an integral part of these.

However, the initial design stage includes not only the mathematical formulation, but also the *software design*. A proper mathematical formulation can be wasted in a poor performance program if the necessary optimizations are not included during the implementation stage.

It is well known that many researchers code everything *from scratch* when a new problem has to be solved. Among the immediate effects caused by this we can mention: waste of time at the programming stage, lack of generalization in the approach, reappearance of common errors and code that is non-modular. Also, any modification to the mathematical formulation would be almost impossible once the code is in production mode.

In this chapter we present the design and implementation of a highly modular and flexible software framework to implement numerical models based on the finite element method. Its potentiality is based on proper abstractions, namely no underlying elemental formulation needs to be known in order to code the resolution of a problem. In addition, the mathematical implementation of operations does not need to be seen from the elemental formulation.

The isolation in three (or more) layers allows the reutilization of important parts of the code, in order to solve problems that can be completely different, or even change the components of the layers without varying the approach to the problem.

A detailed analysis of the class diagram is presented, as well as the main reasons and decisions related to implementation.

5.1 Objectives of the framework

Whenever a problem should be solved by means of numerical techniques, the solution is calculated trying to minimize the costs. How should these costs be evaluated, is the main matter for which usually there is no consensus. Several factors should be considered: basically, the time spent in programming, validation and execution, among others.

When the problem to solve is simple or the analytical solution is known, not much time is invested on the design stage. Unfortunately, if that is the first step to solve a more complex problem, errors might arise and, without a test-case, solutions become untrustful.

In such cases, it is a major improvement when previously validated modules can be utilized. Thus, the code can be extended to problems without known solution and still be considered trustful. If previously validated formulations should be modified to adapt them to the present problem, many different type of errors can be introduced in the code increasing the time spent in the debugging stage.

At the very first moment the code was developed to solve specific problems, but different operations are present in many problems solved by means of the finite element method (FEM). That was the most important reason to define separate modules and entities whenever was possible in order to reuse them without modification. Thus, through the proper definition of interfaces many type of problems can be solved without the need to code the whole resolution.

Many important improvements have been proposed in the last years to build tools or frameworks that allow a certain flexibility and facilities when applying the FEM. We have mentioned some of them in the first chapter (Cardona et al., 1994, Dari et al., 1999, Sonzogni et al., 2002).

This study improves the idea of Dari et al. (1999) by the definition of general interfaces among the different components of the model. This way, if the proposed architecture is respected, not only the elemental formulation, but also the methods employed to solve the problem or even the problem itself can be replaced with minimal changes to the code.

The main objective of the study described is not only to provide a tool to solve some problems of continuum mechanics, but also a framework that allows to reuse the classes designed by means of appropriate abstractions and the constant improvement and diversification at the different layers.

5.2 Proposed design

5.2.1 Identification of stages and entities

The finite element method is widely employed to solve partial derivatives equations (PDE). It is well known that, although many types of elements with their own properties

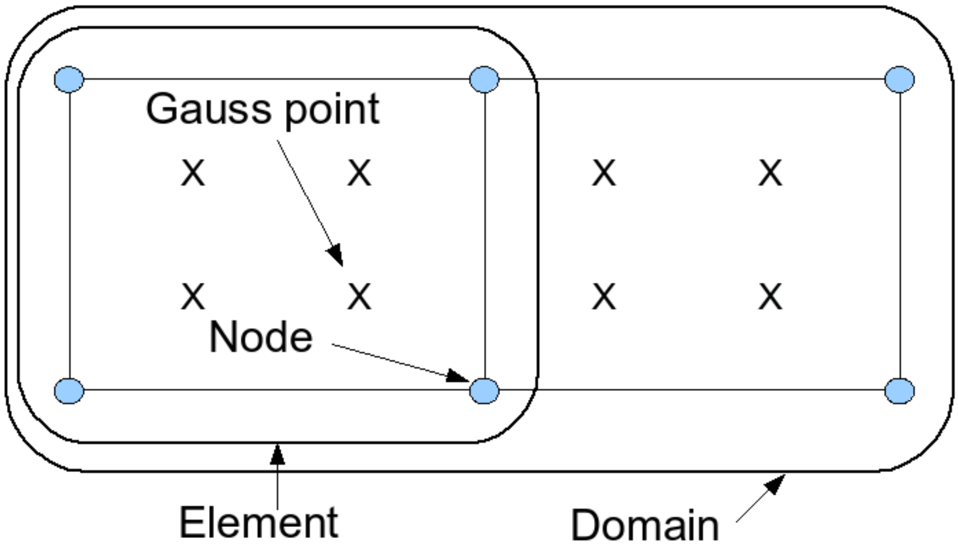

Figure 5.1: Conceptual view of a domain composed by two elements. The elements are defined by four corner nodes and the numerical integration is calculated in four Gauss points. It is shown only as an example, as it is one of many element types that can be employed.

exist, the FEM theory does not depend on a particular element. The FEM can be considered a framework where many specific aspects of the formulations can vary.

From a high level point of view, the following stages can be identified:

- domain description,
- domain discretization,
- element matrices calculation,
- numerical integration in the specified Gauss points,
- assemblage of global matrices/vectors,
- imposition of boundary conditions and
- resolution of the equation system, among others.

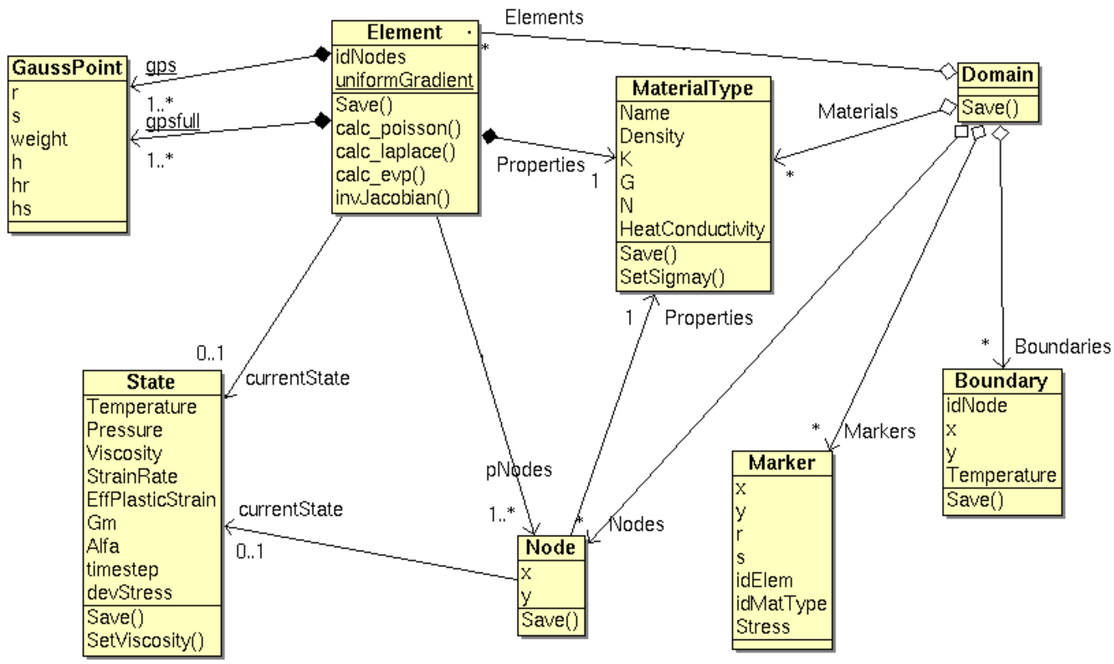

Figure 5.2: Part of the class diagram of the model.

Every stage is defined as independent from the others. Usually, the variations in the formulations can be achieved by means of appropriate parameters; thus, isolating the different processes.

As in a *sequential* analysis of the operations many independent and generic stages can be defined, different layers can be identified inside the domain.

The spatial concepts related to the discretization, like *domain*, *element*, *boundary condition*, *node* and *Gauss point*, introduce a new abstraction level, not in a sequential sense, but from an *entity* point of view.

One can see in figure 5.1 an example of a domain that is formed by two elements. The elements are defined by four nodes located at their corners. The numerical interpolation should be calculated in four Gauss points.

Based on these concepts, the class diagram that can be seen in Fig. 5.2 is proposed. It should be remarked that only the most important attributes of each class are included.

The class `Domain` is the one that includes all the information needed to describe the model by means of a set of elements and nodes stored in the attributes `Elements` and `Nodes`. Once the domain is known, every boundary condition is stored in an instance of the class `Boundary` and the set of all the boundary conditions that determine the problem is stored in another attribute of the `Domain` class (`Boundaries`).

In some problems where the mesh can be distorted, once a yield level of deformation is reached a new undistorted mesh should be generated and the domain state must be copied from the old mesh to the new one. One of the techniques that can be used is the one known as *Markers in cell* (Harlow and Welch, 1965, Moresi et al., 2003).

Due to these reasons, several particles called `Markers` are defined and tracked inside every element. The state of every marker is updated at each timestep based on the element state variables. For every `Marker` its position in physical (`x` and `y`) and natural (`r` and `s`) coordinates, as well as the containing element (`idElem`) and the variables that describe its state are stored. After remeshing takes place, the state of each new element is calculated based on the particles that it contains and the state of the nodes is calculated based on the nearest markers.

All the properties of each material contained in the domain are stored inside the class `MaterialType`, while the set of all materials that form the domain are stored in the attribute `Materials` of the class `Domain`. Considering that a `Marker` represents a particle, it can reference to only one type of material by means of the attribute `idMatType`. To avoid any problem related to particles of different materials that are contained inside the same element, the properties of the elements are calculated as a combination of the properties of the particles (Quinteros et al., 2006b).

It is important to note that the element is determined by a set of nodes that are connected. However, these nodes don't belong to the element because many of them are located on the border and are shared with another element. Thus, only the references to the nodes (`pNodes`) as well as their global id (`idNodes`) are stored in the class `Element`.

To calculate the stiffness matrix of each element, a numerical integration in the Gauss points determined by the order of interpolation should be made. The position of the

Gauss points is identical for every element because the integration is actually made in the master undeformed element. Thus, this set of Gauss points is stored in the attribute `gps` in `Element`, `gps` being declared as a `static` variable. This declaration saves a considerable amount of memory when working on problems that need very accurate solutions, as the information is considered metadata and is stored actually only once in the class and not in every instance. Also, the performance in the access to the elements is increased by a better use of the *caché*.

This way of storing the Gauss points is very flexible at the moment of the implementation of a selective reduced integration (Hughes, 1980) (see section 4.2.3), which can be defined including only the ones that will be employed to integrate and modifying its weight accordingly. Another attribute called `gpsfull` is included in `Element` to be able to perform a full integration for some operations that cannot be computed without the whole set of Gauss points. This variable is also declared as `static`.

As the evaluation of the shape functions (`h`) and their derivatives for every elemental coordinate (`hr` and `hs`) are calculated always in the master undeformed element, these are calculated in advance and stored in `GaussPoint`. Later at the integration stage, the only thing that is necessary to operate over the real deformed element is the inverse of the Jacobian matrix. This enhances the overall performance of the integrations when combined with the few instances of the class `GaussPoint`, that are stored in `static` variables.

Especially in transient problems, the state of the material should be stored in order to calculate the next time step. In the classical FEM, the unknown variables are calculated at the nodes and, thus, these results belong to them. But many secondary variables can be also calculated (e.g. stress, strain, effective plastic strain) and in some special cases these should be stored in the elements. The `State` class stores variables that are calculated by the model and must be stored arbitrarily in the `Element` or the `Node`. One can see in figure 5.2 that the `State` class is related to the `Element` *and* the `Node` class, by means of a pointer called `currentState`. Once the type of element is defined, as a part of the discretization passed as a parameter, it is clear for the model where the `State`s will be stored.

5.2.2 Interface with *solvers* and mathematical libraries

Once the design of the high level classes of the problem is complete, namely the data structures that are related to them, the connection with other pieces of code can be addressed. It is known that the stiffness matrix associated with every instance of the `Element` class is computed by means of the multiplication of some matrices related to some geometrical and compositional properties of the element. There are really good and thoroughly tested libraries for linear algebra operations that can be employed to address the matrices operations. Thus, some interfaces were included so that the model could be isolated from implementation details and libraries can be replaced in the future. The class `Matrix` is designed to store all the matrices and vectors that take part of the framework except in a few cases. It also isolates the model from the Lapack (Anderson et al., 1999) library by means of an interface that provides a basic set with the most common operations for matrices related to the FEM.

This class provides a simple, natural and practical way of manipulating matrices. Overloading of operators and polymorphism were heavily used in order to achieve an intuitive notation (Figure 5.3), preventing obscure coding techniques, particularly for the assignation of a value to a specific coordinate of the matrix.

The element matrices are considered to be dense because most nodes inside an element are in contact with each other. In these cases, matrix operations tend to reach a good performance because not much memory or computational time is needed to operate over matrices whose number of components is associated with the square of the number of nodes per element. However, that is not true in the case of the global stiffness matrix.

In problems that need a very accurate solution, the global stiffness matrix will be very sparse and its size in memory would be of the order of the square of the number of total nodes. Another class called `SparseMatrix` was designed for this type of matrices, in

```
Matrix<double> m_A( 2, 4, "A");
Matrix<double> m_B( 4, 2, "B");
Matrix<double> m_2x2( 2, 2, "2x2");
Matrix<double> m_4x4( 4, 4, "4x4");
...
m_A(0, 2) = 1.2;
m_A(0, 3) = 3.5;
m_B(0, 1) = 8.7;
m_B(3, 0) = 0.1;

m_2x2  = m_A * m_B;
m_4x4  = m_A.trans() * m_B.trans();
m_A   += m_B.trans();
```

Figure 5.3: Syntax example using the Matrix class.

order to improve the storage in memory and the time needed to process some operations. This class works as an interface that isolates the framework from the SuperLU library (Demmel et al., 1999). This library provides fast and tested procedures to solve linear systems stored in sparse matrices.

The low level tuning of the SuperLU parameters provides a very good performance associated with the resolution time in case of symmetry. If necessary, some precalculations can be stored and reused if the sparsity pattern is similar (general case), namely the row permutation, determined from partial pivoting, and the column permutation, that makes the L and U matrices sparser. This type of enhancements can reduce drastically the amount of time needed to solve transient non-linear problems.

`SparseMatrix` has less functionality than the `Matrix` class because it is used only to solve the system of equations. The class implements a particular storage format called *Harwell-Boeing* (Duff et al., 1992), also known as *compressed column storage*, that is supported by many scientific libraries. The structure associated with the storage format is shown in Figure 5.4.

This class includes some optimizations to improve the overall performance. The *Harwell-Boeing*(Duff et al., 1992) structure is replicated into a buffer inside the class that collects a certain amount of data, defined by a parameter at construction time,

```
template<class T>
class SparseMatrix{
public:
T *values;        /* non-zero values stored by column */
int *rowind;      /* row of the stored value */
int *colind;      /* colind[j] indicates the offset inside
      values and rowind indicates the offset of the
      first value of column j. It has cols+1 entries
      and colind[cols] = realnnz */
int rows;         /* number of rows in the matrix */
int cols;         /* number of columns in the matrix */
int realnnz;      /* number of non-zero values */
......
}
```

Figure 5.4: Specification of part of the SparseMatrix internal structure.

to improve the insertion process by reducing the number of access to memory needed. A method `flush` is also defined to merge the buffer into the already inserted data. This method can be called either manually or automatically when the class considers it necessary.

Another optimization is the option of storing only half the matrix in the case that it is symmetric, a situation that is quite usual in the problems solved by the FEM. A method called `Unpack` is also provided. This method converts a symmetric matrix that stores only half of the components into a full matrix that stores both sides of the diagonal.

The access to the elements and the basic matrix operations have the same specification than the class `Matrix`. So, small problems could be solved using normal dense matrices only by changing the type of the variable.

All the classes include the method `Save`, that stores the instance into an output stream. These same classes have a constructor, with an input stream as the parameter, that read the instance from the stream and creates it in memory. This way, if the simulation involves many time steps, the state of the simulation can be saved at any moment and the execution can be restarted again since the last checkpoint.

The main idea behind the implemented interfaces is to abstract the model from the libraries that are being used, which gives the opportunity to use different ones. For example, at this moment another library for sparse matrices, called Pardiso (Schenk et al., 2001), is being analyzed to replace the current implementation of SuperLU.

A list with the specification of some selected operations of the `Matrix` and `SparseMatrix` classes can be find in appendix A.

5.3 Elemental level abstraction

Up to this moment, no mention has been made of the type of element employed, mainly because the generic schema of resolution doesn't need to know the element implemented to solve the problem. By means of the proposed design and interfaces, a nearly total freedom from the element implementation can be obtained.

Many element operations can be specified in a generic way and without information about the type of element, like the *push forward* used in the Lagrangian approaches or the *uniform gradient*.

In the proposed design the `Element` class is defined as a base class that provides a common specification that the different types of element must implement. It also includes the specification of the functions to solve the different types of equations.

In Figure 5.5 we can see the schematic diagram of the message passing sequence among the different classes while creating a domain and its related objects.

All the element methods that cannot be defined in a generic way must be implemented in a separated class that inherits the specifications from `Element`. The `Liu` class that can be seen in Figure 5.5 is an example of a particular element implementation. See for instance the call to the `SetMaterialType`, that is in fact implemented in the `Element` class.

In its simplest form, the solution of partial derivative equations by means of the FEM implies, for each element, the evaluation of matrix products (that depend on the problem) in some points called *Gauss points*. These evaluations are multiplied by a

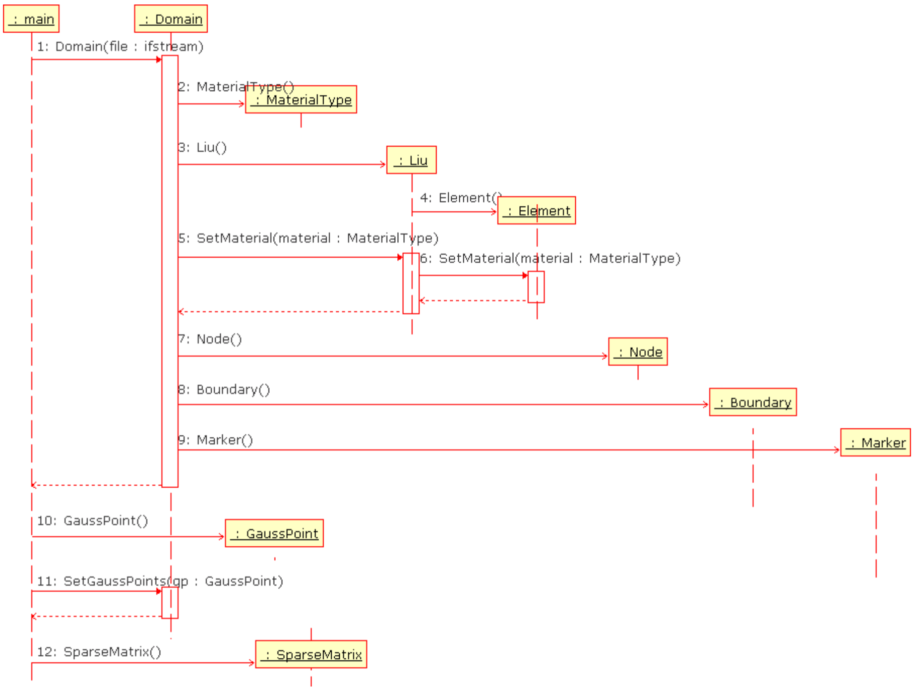

Figure 5.5: Schematic diagram of the message passing sequence to create a Domain and the related objects.

weight factor and summed to obtain the element stiffness matrix.

From all these tasks, only the evaluation in a specific Gauss point needs information about the number of nodes that the element have. That is the main reason to implement in the `Element` class a method called `calc_equation`, where all the necessary steps to get the element stiffness matrix related to the problem (`equation`) are implemented with the exception of the specific evaluation in the Gauss points, that must be defined in a method called `eval_equation` implemented in the derived class (`Liu` in this case) and that receives the `Gausspoint` where the integration will take place as a parameter.

The schematic diagram of an equation resolution is shown in Figure 5.6. In this particular case it is the Poisson equation. However, many different equations can be calculated in the same way.

It can be seen that the class that implements an specific element (`Liu`) passes the messages to the `Element` class, where all the common code was actually implemented. The only method that is executed in `Liu` is `eval_poisson`, which evaluates the integra-

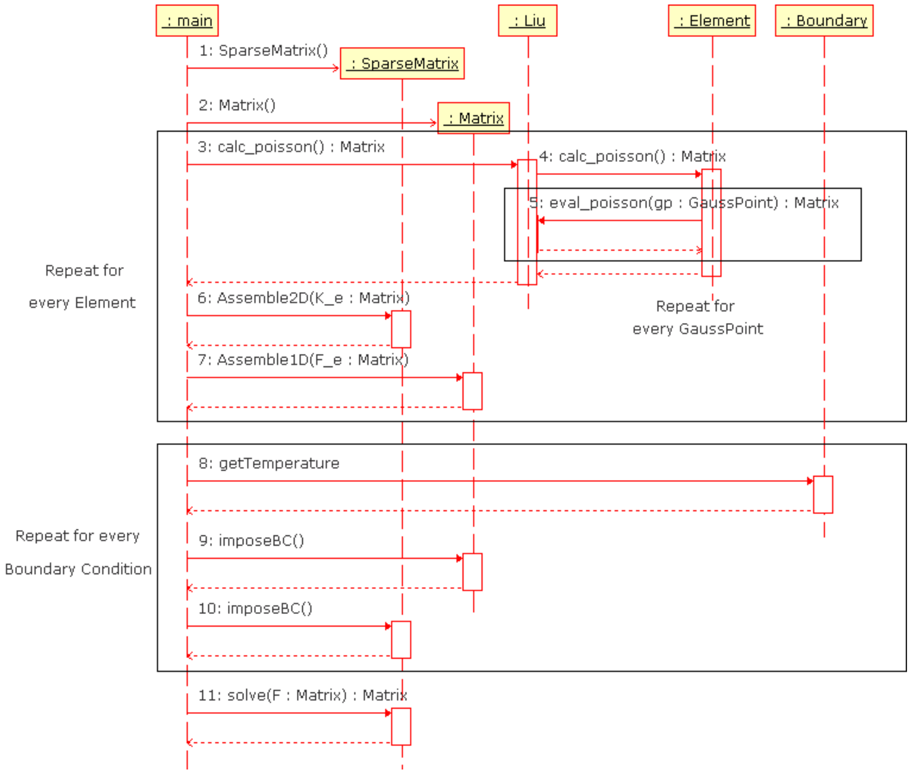

Figure 5.6: Schematic diagram from the resolution of the Poisson equation.

tion in a specific Gauss point.

5.4 General schema of the model components

The framework presented relates to other software components to perform some tasks, as the domain discretization and the resolution of the equation system. The relation among these components is shown in Figure 5.7.

As the model was thought and designed as a general purpose finite element framework, it should be domain independent and the selected discretization must be associated with input parameters rather than with the model itself. There are multiple choices of good graphical interfaces that can deal with this task, as the well known *GID*, designed and developed by CIMNE (International Center for Numerical Methods in Engineering).

An interface was developed in our model inside the class `Domain` in order to read the

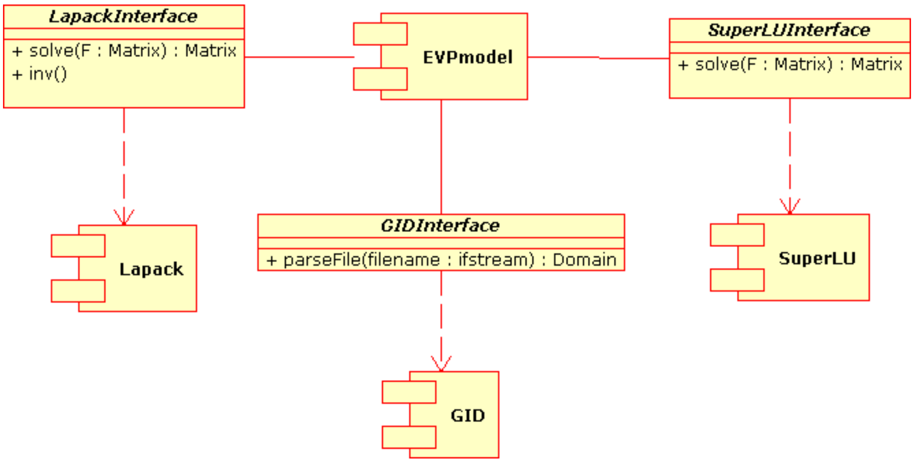

Figure 5.7: Schematic diagram of the model components and the interfaces that relate the different components of the model.

domain description from this system and to create the appropriate data structures that will be used by our code and that are independent from the software that generated them[1].

The operations on dense matrices are computed by the `Lapack` (Anderson et al., 1999) library. However, the only contact with the model is through the interface implemented in the `Matrix` class. Thus, only methods of this class are called in the model, isolating and abstracting the model from the component that actually executes the algebraic operations.

A similar case can be found in the `SparseMatrix` class, that isolates the model from the `SuperLU` (Demmel et al., 1999) libray and its implementation of resolution of big equations systems stored in a sparse matrix.

The language used to implement the framework was `C++` by means of a standard GCC compiler (tested with versions 3.3 to 4.1.2). The implementation was done on a *Gentoo* Linux distribution and also tested without problems in similar Linux distributions. One of the final aims of the development is to migrate the code with minimum effort and changes to a *Beowulf* cluster. That was the main reason behind the selection of the

[1] An interface to import the discretization structure from the Matlab domain generator is also being developed at this moment.

components, because not only `Lapack` but also `SuperLU` are available for this type of configurations.

5.5 Implemented elements

5.5.1 Four nodes with reduced integration

As an example of the flexibility of the developed model, two types of two-dimensional quadrilateral element with different features have been implemented. The first one was described in detail in section 4.2.3 and is implemented by the class called `Liu`.

The second one is implemented in the `EightNodes` class and is explained in the next section.

5.5.2 Classical eight noded element

It is known that the classical quadrilateral four noded element does not pass the Brezzi-Babuška condition (Brezzi and Fortin, 1991), which is necessary to assert the solution convergence and avoid collateral effects like *checkerboard* pressure distribution.

That's why the second element implemented was a two-dimensional quadrilateral eight noded element (NN = 8). Neither a stabilization operator nor any *hourglass mode* control was included due to the higher order in the interpolation.

Shape functions (h) are defined in the usual way for an eight noded element. The spatial coordinates (x) as well as the velocities (or displacements) are calculated by means of the 4.28 and 4.29 equations.

Strain rate is computed in the standard way by the equation 4.30, where B_a is the gradient matrix that includes the shape functions derivatives. No expansion in a Taylor series is made and the integration is performed in the usual full set of Gauss points related to the second order of interpolation inside the element (Bathe, 1996).

As a comparison of the convergence properties of both elements implemented, the cantilever beam test case shown in the previous chapter is run with the new element.

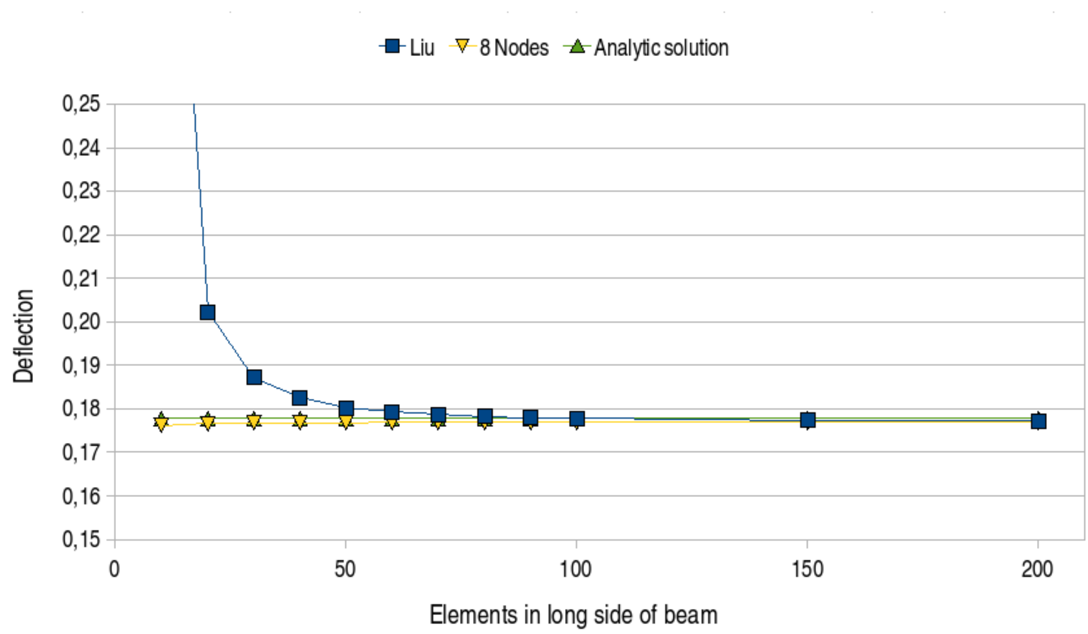

Figure 5.8: Convergence of the eight noded element compared to Liu as a function of the number of elements on the long side of the beam.

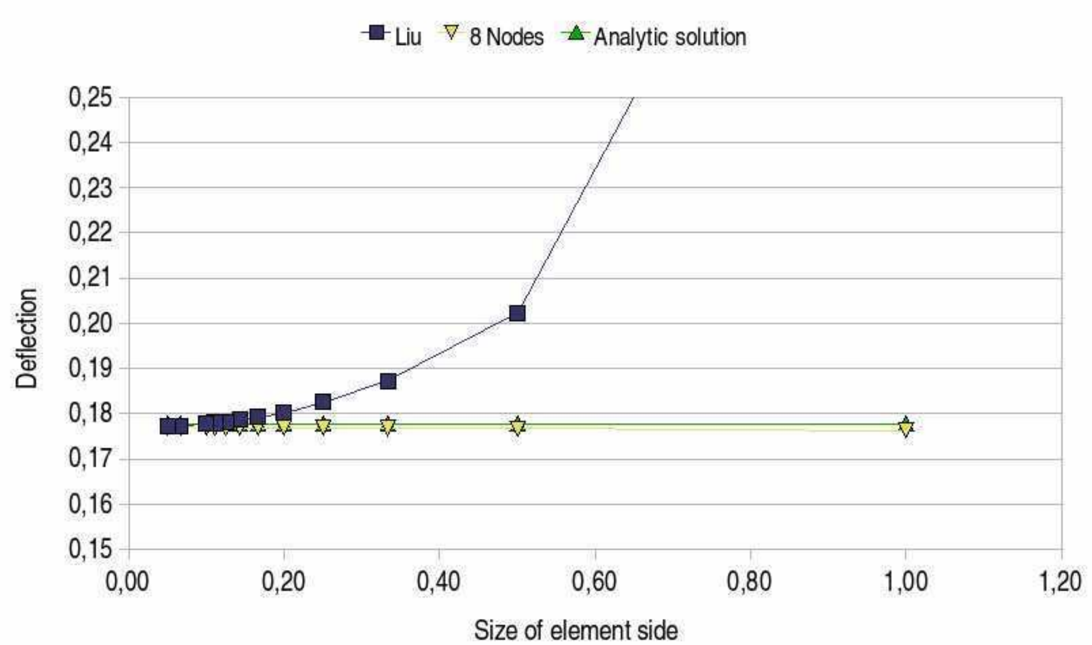

Figure 5.9: Convergence of the eight noded element compared to Liu as a function of the length of the element.

The results can be seen in figures 5.5.2 and 5.5.2. One can see the difference in terms of convergence that it can be achieved by the higher order of interpolation.

6

Results

Two examples of the results obtained by the application of the models defined in chapter 3 and 4 will be presented in this chapter.

In the first place, the model based on Stokes equations (see chapter 3) was employed to simulate the Miocene evolution of the Patagonian Andes. The results were compared with previous studies of Thomson et al. (2001) and Blisniuk et al. (2005) among others, that published evidences of subduction erosion, uplift and the establishment of a rain-shadow effect as a result of fission track analysis and stable isotopes studies.

In the second place, a geodynamic process called *delamination* and its influence in the surface evolution was simulated by means of the model described in chapter 4. The model was implemented over the FEM framework described in chapter 5.

6.1 Miocene evolution of the Patagonian Andes

6.1.1 Geological setting

The Southern Andes, as defined by Gansser (1973), encompass the orogen developed along the Pacific margin of South America between 46°30'S (Gulf of Penas) and 56°S. The segment to the North of the Strait of Magallanes is known as the Patagonian Andes. Subduction has been continuous since early Mesozoic times (more than 150 Ma (millions of years)). Deformation started in the Late Cretaceous and later in the Paleogene, although a great deformation and uplift phase in this segment took place after the late Oligocene (30-28 Ma) (Thomson et al., 2001). The sudden change in plate kinematics and the strong acceleration in the convergence rate (Somoza, 1998) controlled the deformation until the late Miocene-Pliocene (10-3 Ma) (Ramos, 1989), when an oceanic spreading ridge was subducted (Cande and Leslie, 1986, Ramos, 2005).

The Southern Patagonian Batholith is considered the backbone of the Patagonian Andes. It runs with a NNW trend continuously along all the segment and has an average width of 120 km (Hervé et al., 2000). The exhumation of the batholith indicates that it has suffered an extreme denudation which was climaxed later by the establishment or enhancement of an orographic rain-shadow by the middle Miocene (17-16 Ma). The rain-shadow caused drastic climatic and ecologic changes as a result of more than 1 km uplift (Blisniuk et al., 2005). The total denudation estimated by fission track analysis ranges from 4 to 9 km west of the present-day water divide and decreases to less than 3 km to the east (Thomson et al., 2001).

The facts that the batholith is located in the present forearc and that early Miocene magmatic rocks (Punta Daphne ca. 48°S) are found around 120 km from the present trench are considered to be proofs for subduction erosion occurring in this segment (e.g. Thomson et al., 2001). The apparent subduction angle at that moment (Bourgois et al., 1996) and the depth at which a typical magma should have been produced indicate that the original position of these could have been more than 200 km away from the early

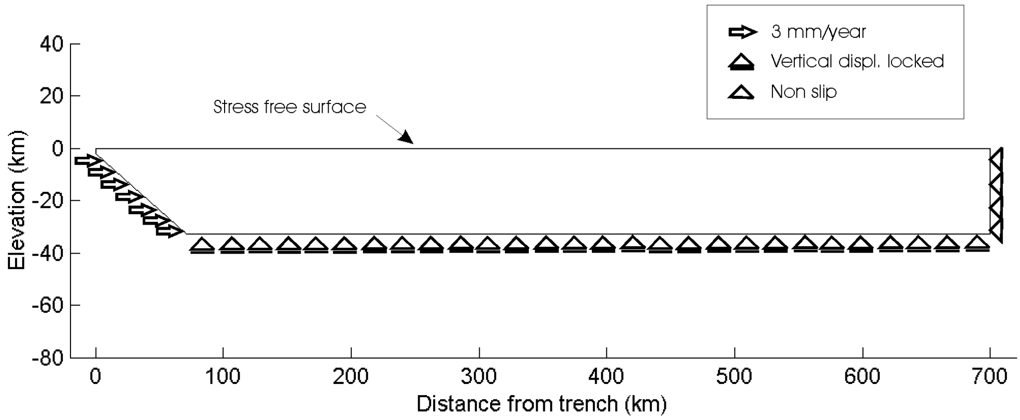

Figure 6.1: Boundary conditions.

Miocene trench. These facts indicate an approximate rate of more than 3 km/My of trench retreat.

6.1.2 Model set up

As can be seen in figure 6.1, the upper (topography) side is defined as a free stress surface that represents the topography resulting from the tectonic process, not taking into account the acting erosion. The western side represents the contact between the eastward subducting Nazca plate and the South America continental plate. On that side, the subduction imposes an horizontal velocity of 3 mm/year to the east (Brooks et al., 2003), and the vertical velocity is zero. The lower side represents the limit of the crust and was established at 33 km depth because of the rheological contrast with the deeper lithosphere. The vertical velocity was considered to be zero and the horizontal velocity was left free in the whole segment. On the eastern side all the nodes have a non-slip boundary condition, so the deformation is restricted.

The material properties were the ones shown in table 3.1. One can see that the upper crust is considered homogeneous and its viscosity distribution is basically determined by the temperature and the strain rate (see equation 3.19).

Only half of the absolute eastward trench motion is explained by the velocity imposed on the Wadati-Benioff zone. Due to the geological evidence showing the existence of subduction erosion, 3 mm/year are considered to be removed from the contact between both plates (Thomson et al., 2001). Thus, resulting in a shortening rate of 3km/My but a total overriding velocity of 6km/My (Vietor and Echtler, 2006). The trench roll-back velocity is not considered because only the continental plate is being modeled.

The model was applied to a transect (vertical section) at approximately 47°S. The results show that, at the beginning of the simulation, the deformation and uplift concentrate in the magmatic arc as a consequence of the thermal conditions. The high thermal flux in the magmatic arc causes the material to have low viscosity values (figure 6.2.a), which results in a higher initial strain rate (figure 6.2.b) and in a weaker zone where material flows/deforms easily.

6.1.3 Topography and orographic rain-shadow

The simulation of the evolution of the topography during early and middle Miocene can be seen in figures 6.3 and 6.5. As the orogen grows, erosion becomes more effective resulting in a higher erosion rate (figure 6.3.a / 6.3.b). When it reaches a certain yield altitude, humid winds cannot bypass the drainage-divide causing an asymmetric precipitation pattern with the western side heavily eroded (figure 6.3.b / 6.3.c). At the same time, as subduction erosion forces the shifting of the magmatic arc, eastern zones are heated and deformed (Fig. 6.4) resulting in a consequent surface uplift. The combination of both processes results in a progressive migration of the maximum locus of exhumation towards the east as can be seen in the four snapshots of figure 6.3.

The amount of denudation along the transect in our simulation is in complete agreement with the studies of Thomson et al. (2001) who were able to quantify approximately the eroded material in the zone. They demonstrated by means of fission track analysis that the surface erosion since ca. 30 Ma in the western side of the water-divide was between 4 and 9 km, while in the eastern side is at most 3 km. It can be seen in figure 6.3 that the calculated denudation is up to 8 km in some parts of the transect and only

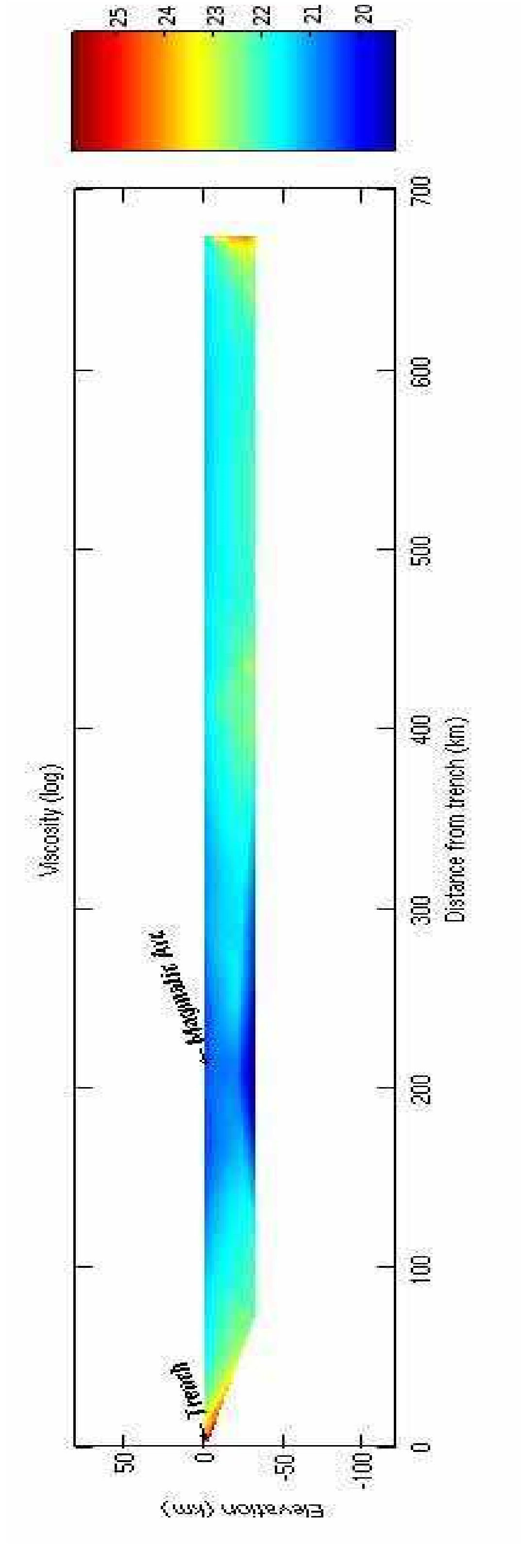

a)

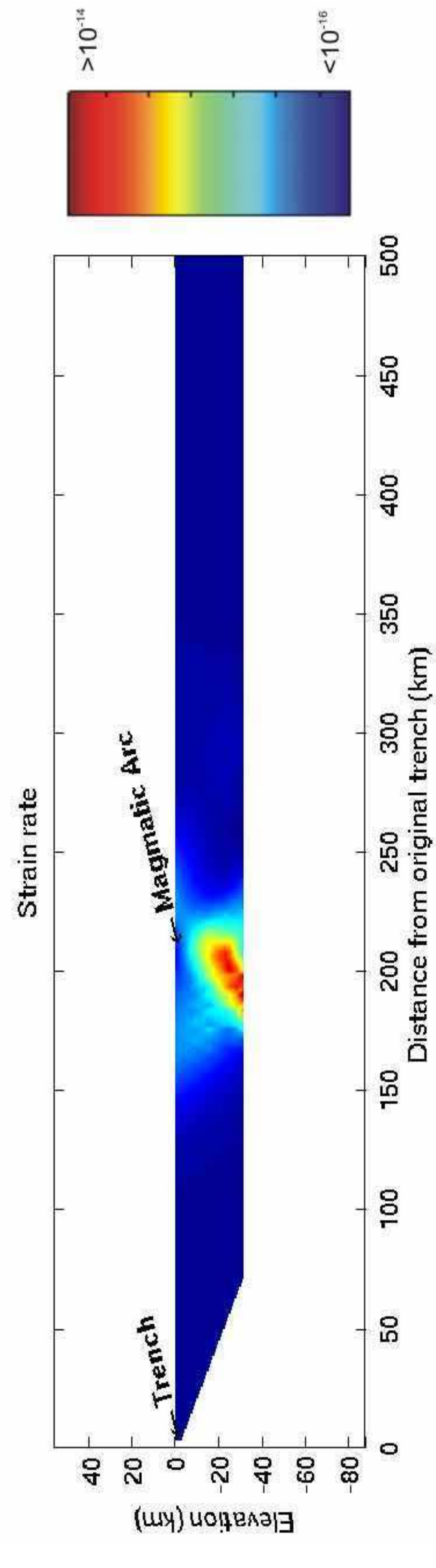

b)

Figure 6.2: a) Viscosity and b) Strain-rate at the beginning of the simulation.

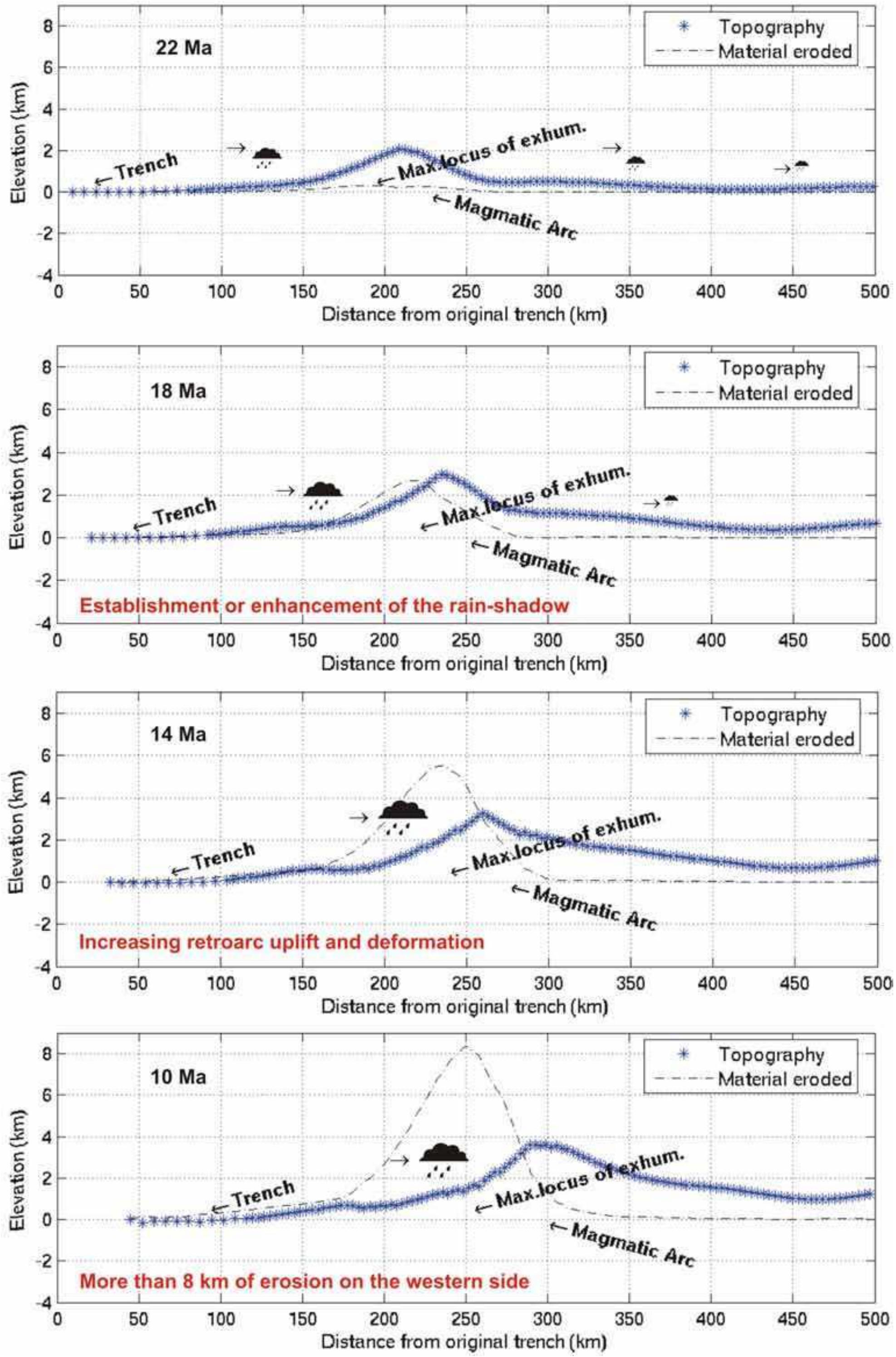

Figure 6.3: Topography and Surface Erosion at 22, 18, 14 and 10 Ma. Dotted line shows the amount of material carried out of the domain towards foreland basin or trench.

considering the period modelled, what would imply a good correspondence with figures found in Thomson et al. (2001). Also, the volume (per unit width) of the material eroded from the surface in the section considered is about 700 km^2. This is coherent in orders of magnitude with the volume of material sedimented to the east of the orogen. The deposits are known as *Santa Cruz Formation* (Nullo and Combina, 2002) and extend from almost the present water-divide to the Atlantic coast. The period encompassed by this Formation is almost the same as the one of the simulation. Thus, it turns out to be one of the best constraints to compare the model results, considering that at least a great part of the material that was eroded should have been preserved somewhere else. The other part could have reached the trench and be accumulated there or even be subducted with the ocean slab.

6.1.4 Deformation style

A particular observation in the simulation is the modification in the deformation style. In figure 6.4 the evolution of the strain rate is shown. The most remarkable feature in the evolution is the change of orientation for the maximum strain rate, which moved from the retro-shear to the pro-shear zone. Among the factors that favour this, we can mention the strong erosion acting on the western side of the orogen. This is in complete coincidence with the results of Beaumont et al. (1992) who found that when erosion removes mass from a plateau or its flanks, strain rates increase where erosion has occurred. Strong crustal erosion also favours this process because due to the migration of the arc, the lowest viscosity values and maximum strain rates can be found to the east and near the bottom boundary of the domain.

It is important to remark that the exhumation pattern shown in figure 6.3 has exactly the same features as the one proposed by Willett (1999a) for orogens with an asymmetric pattern of erosion (higher in the pro-shear zone), with a broad domal exhumation pattern across the prowedge interior. The main difference between both experiments is that in Willett's work there was no crustal erosion, so the process reaches a steady state at some

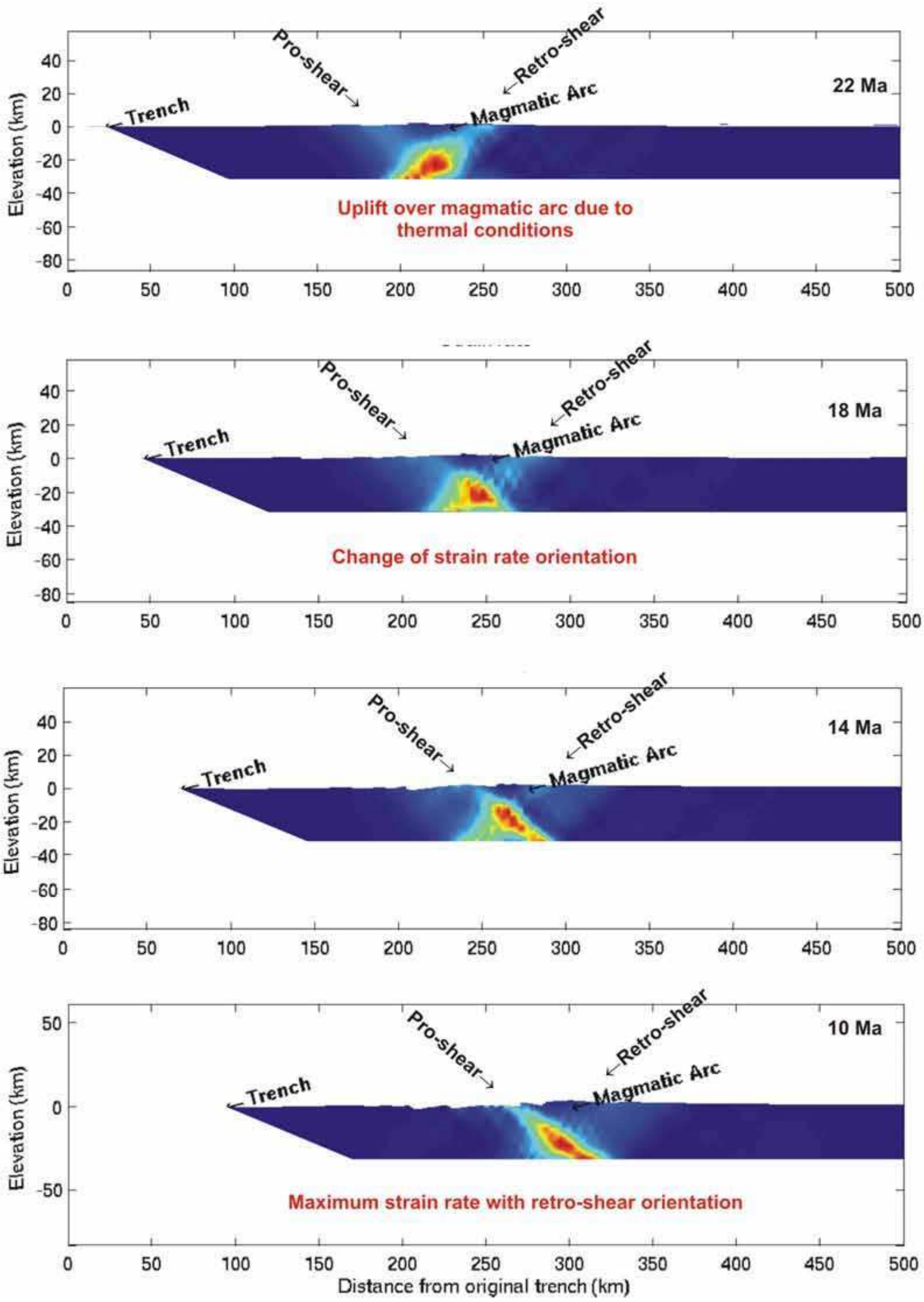

Figure 6.4: Strain-rate distribution at 22, 18, 14 and 10 Ma.

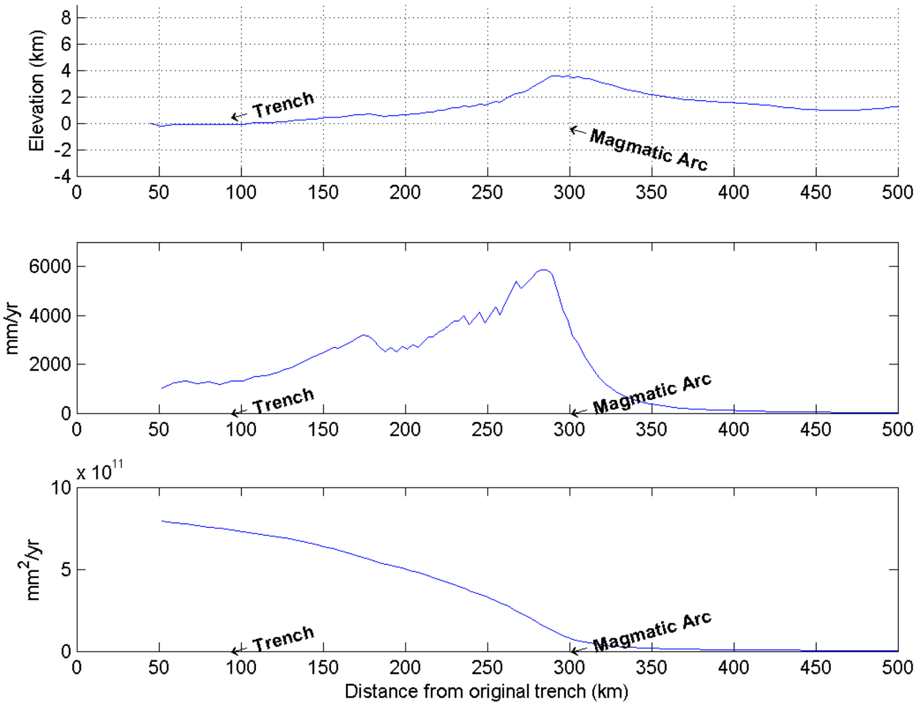

Figure 6.5: Topography, precipitation and available water flux calculated by the model at approximately middle Miocene (12 Ma).

point of the evolution and there is no surface uplift in the retrowedge. This could have been caused by the boundary conditions imposed, where the region over the point called S (see figure 1.1) concentrates a great part of the deformation due to the restrictive kinematical conditions towards the forearc and retroarc.

In the case of our simulation, the migration of the magmatic arc towards the east increases the thermal flux in the foreland, which will quickly be weakened by the reduction of its viscosity that favours the deformation and surface uplift on the retrowedge.

The total shortening obtained in the simulation during the considered period is about 45 km. This shortening is in complete agreement with the detailed field evidence published by Ramos (1989) where the absolute minimum shortening for this period ranges from 22 to 45 km.

Another important result is that the model predicts the establishment and posterior enhancement of the orographic rain-shadow in similar circumstances as the ones described by Blisniuk et al. (2005), who published data that support the drastic ecological and climate changes that were caused by this process. The asymmetric pattern of precipitation predicted for middle Miocene can be seen in part b) of figure 6.5. Precipitation reaches its maximum value almost at the topographic divide in coincidence with present day distribution.

6.2 Lithospheric delamination: a geological example

A common feature of every orogen is the presence of a crustal root. Let's define *crustal root* as the deepest part of the crust which grows in order to compensate isostatically the tectonic stacking that is produced in the surface because of the intense compression.

In a simplified way, the following stages can be found in the life of an orogen as proposed by Leech (2001): compression and crustal thickening; mineralogical changes in the crustal root; extensional orogenic collapse and a new equilibrium configuration.

When the tectonic stacking is above a certain threshold that imposes high pressure and temperature conditions on the deepest part of the crust, the crustal root suffers

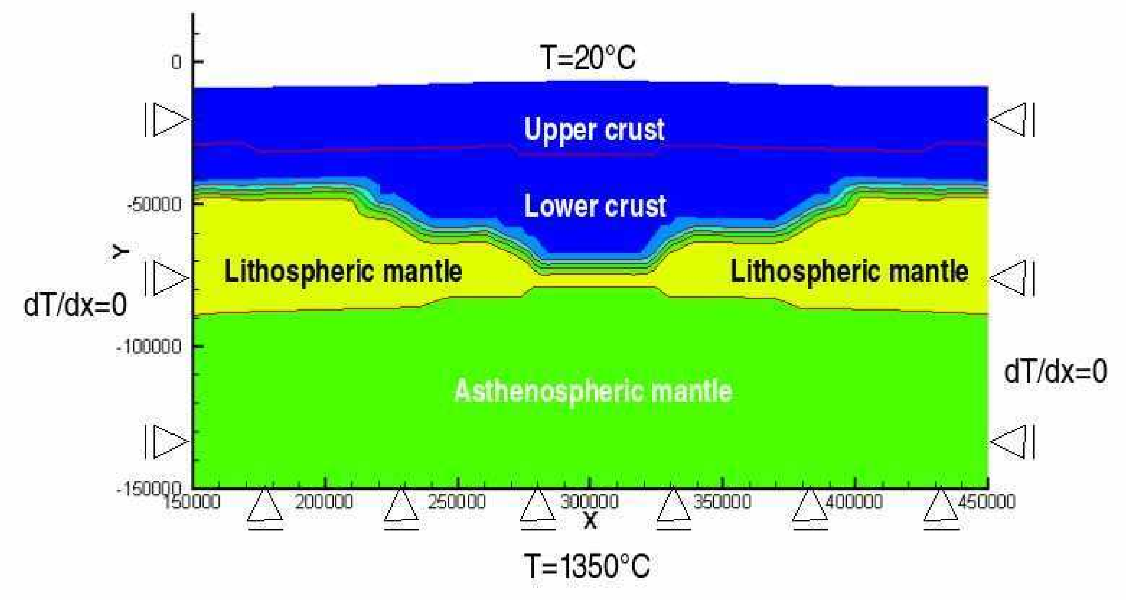

Figure 6.6: Boundary conditions of the thermo-mechanical model to study the evolution of an orogen whose crustal root delaminates.

mineralogical changes (e.g. Austrheim, 1998). With these conditions and in the presence of fluids, the rocks of the lower crust evolves to others with higher density until a rock called *eclogite* is formed. Finally, the system dynamics suffers a sudden change and turns to be unstable, due to the density increment in these rocks.

Delamination is defined as the process by which the eclogite detaches from the lower crust and falls into the asthenospheric mantle driven by its higher density. The main causes of crustal delamination are thermal and mechanical (composition and phase changes) as mentioned by Kay and Kay (1993). Every orogen is supposed to suffer crustal delamination at a certain moment of its evolution (Leech, 2001).

Details about this process are known from a conceptual point of view, but some of its aspects are quite difficult to quantify.

6.2.1 Model setup

The domain studied consists of the lithosphere and asthenosphere up to 150 km depth and 300 km width. The orogen is considered to be located in the middle of the domain.

Parameter	1	2	3/4	5
ρ / Density (kg m^{-3})	2800	2900	3340/3220	3850
K / Bulk elastic Modulus (GPa)	55	55	122	63
G / Shear elastic modulus (GPa)	36	36	74	40
A / Material rigidity (MPa^{-1} s^{-1})	10^{-28}	10^{-28}	$10^{-14.3}$	$10^{-15.4}$
Q / Molar strength activation (kJ mol^{-1})	223	300	515	356
n / Power law exponent	4.0	4.0	3.5	3.0
$\dot{\varepsilon_o}$ / Reference strain rate (s^{-1})	10^{-15}			
σ_0 / Cohesion strength (MPa)	20		40	
Θ / Internal friction angle (°)	30			
Δt / Time step (years)	10^3			
R / Gas universal constant (J mol^{-1} K^{-1})	8.3144			
κ / Heat conductivity (W/K/m)	2.0	2.5	3.3 / 41.0	2.5
q / Heat productivity (μW m^{-3})	2.0	0.75		

Table 6.1: Model parameters to study the delamination process. 1) Upper crust / 2) Lower crust / 3) Lithospheric mantle / 4) Asthenospheric mantle / 5) Eclogite.

Crust is 36 km deep far from the orogen and 60 km deep in its axis. The crust is divided in two layers: upper and lower crust, whose distribution can be seen in figure 6.6.

There is an underlying layer of mantle that is divided into lithospheric and asthenospheric. The main difference between both of them is not compositional but thermal. When the lithospheric mantle temperature is above 1250°C it transforms into asthenospheric and its density changes. The limit between both types of mantle is calculated by means of the coupling and feedback between the thermal and mechanical model.

All the variables associated with thermal and mechanical properties, the rheology of the materials and other parameters are shown in table 6.1.

In the beginning, the domain has an arbitrary distribution of lithosphere and asthenosphere. However, after a few time steps the isotherms stabilizes and also the distribution of the two different types of material that are temperature dependent (asthenosphere and lithospheric mantle). Later, a real configuration is obtained, in accordance with the one expected by the thermal conditions applied and the material properties. During these stabilization time steps, the domain is compressed slightly by the action of gravity until an equilibrium state is reached. At that moment, the whole configuration is consistent and the desired boundary conditions can be applied.

The boundary conditions for the thermal model are: 20°C over the surface and 1350°C over the bottom boundary. On the lateral boundaries *free-slip* vertical conditions are imposed and horizontal displacements are not allowed. Vertical displacements over the bottom boundary are also forbidden.

The orogen is about 3 km height after the stabilization time steps, at the moment when the eclogitized root appears.

6.2.2 Results

The main objective for this experiment was to model the effects of eclogitization on the base of the orogen in a case where the lower crust evolves to one of the densest eclogites. To study the phenomenon in a proper way, it was isolated from other types of forces that modifies the dynamics of lithosphere, namely compression, extension or thermal anomalies.

In this experiment, an orogen with a deep crustal root was considered. A fluid that favours the transformation to eclogite is present at the beginning of the simulation and lasts up to 3.5 My.

Once the orogen is stabilized, the appropriate boundary conditions are applied. All the material that suffers the pressure of more than 55 km of crust is considered to transform into an eclogite during the first 3.5 My, due to the presence of fluids in the system. The evolution of the whole domain for this experiment can be seen in figure 6.7.

The transformation of the crustal root to eclogite, which has a higher density than normal lower crust, causes orogen collapse due to the increment of weight. In the base

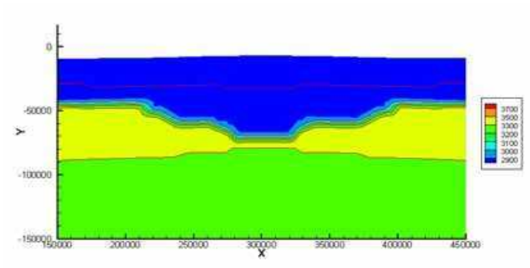

0 My)

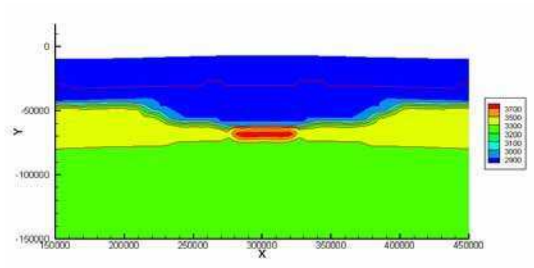

1 My)

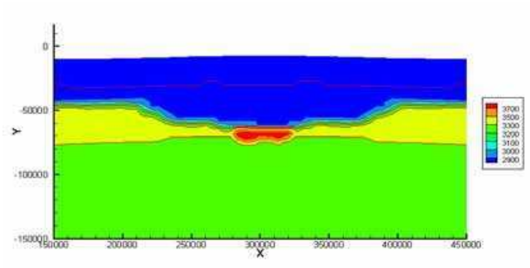

2 My)

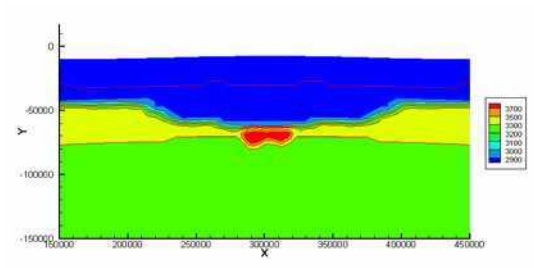

3 My)

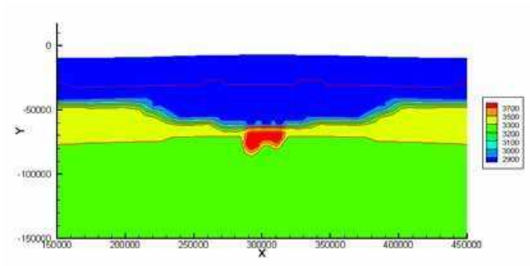

4 My)

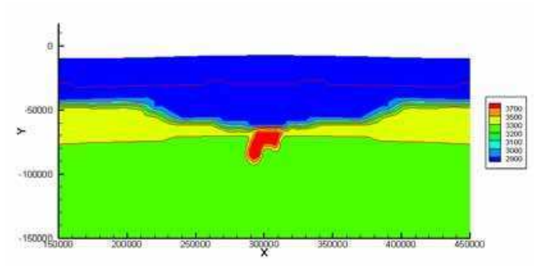

5 My)

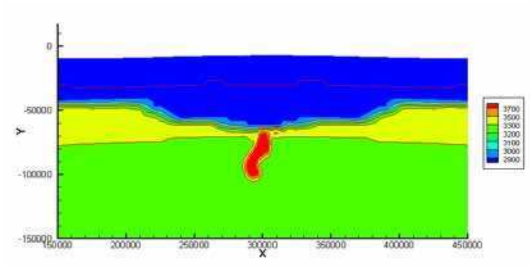

6 My)

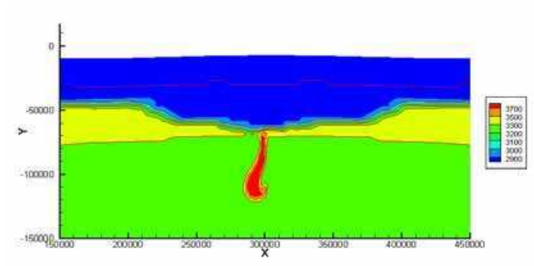

7 My)

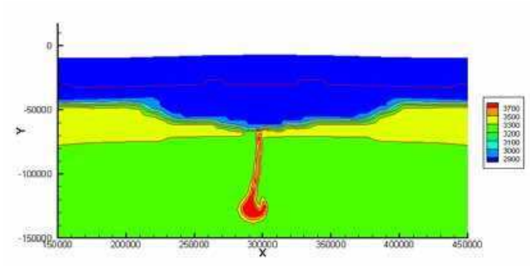

8 My)

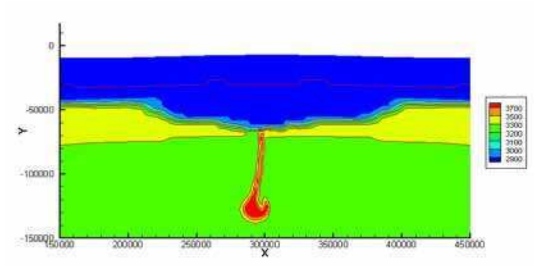

9 My)

Figure 6.7: Evolution of the density distribution in the domain during the *eclogitization* process of part of the lower crust.

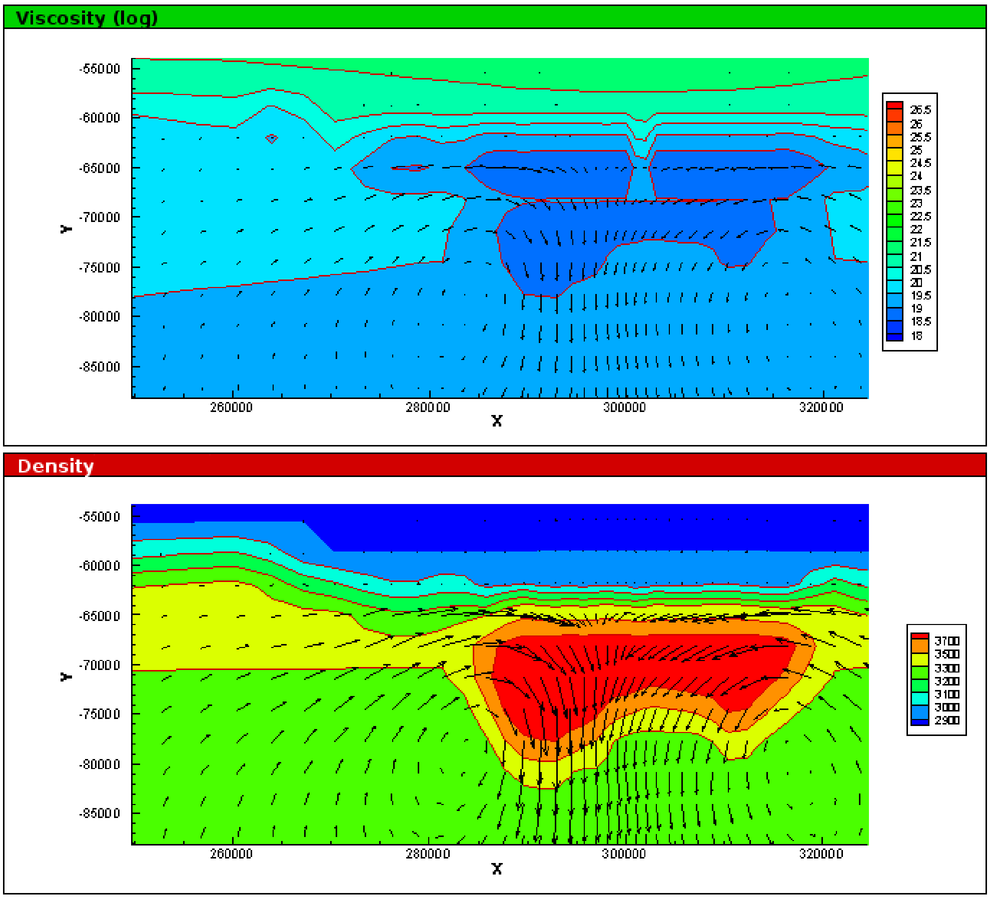

Figure 6.8: Detail of the contact between eclogite and lower crust.

of the crust, due to the density difference between the eclogite and the asthenospheric mantle, the former tries to go down but this is difficult during the first My because it is stuck to the rigid lower crust. It should be pointed out that the crustal roots, due to the regional compensation (Vening-Meinesz, 1941, Turcotte and Schubert, 1982), are usually distributed in an horizontal direction as the one seen in figure 6.6. This fact can sometimes prevent the vertical column from having the necessary mass difference to start the detachment process.

When one sees tomographies of this deeper processes, it is usual to consider that the eclogitized root is simply detached from the crust due to the mass anomaly. Specially if the material was part of the rigid crust and thus, resistant to the forces exerted over it. This way, it would delaminate without much internal deformation. However, laboratory experiments performed by Leech (2001) show that eclogite is much more *ductile* than the original rock and thus would suffer a greater deformation as soon as the system turns unstable and the stress increases. This ductility will be one of the weak points of the domain from a mechanical point of view.

But Leech identifies another point of weakness in the system: the contact between eclogite and the lower crust. The downward pressure that the eclogite exerts and the crustal rigidity turns the contact between them into a low pressure region, and thus unstable. One can see the distribution of density and viscosity for the crustal root of the orogen in figure 6.8. The contact will receive a hot incoming mantle flow from the sides because there it is the material with lowest viscosity, the one that can easily flow to *fill this gap*. The lateral force exerted by the incoming mantle is not only deforming the eclogite, but also introduced into the contact between the latter and the crust. The expossure of the contact to higher temperatures and the intense deformation in the zone that increases the strain rate, results in a decreasing viscosity, that is in complete agreement with the results published by Leech (2001). One can see in the figure that the lowest viscosity zone is located exactly on the contact between eclogite and lower crust.

The force exerted by the mantle from the sides, the eclogite ductility and its increased weight due to its higher density are the main causes for the formation of a descendant plume, that is pushed and deformed by two convective cells mainly composed of hot asthenospheric mantle. The convective cells at a certain moment of the evolution are shown in figure 6.9.

An important consideration that should be addressed is the distribution of the isotherms. In a more typical subduction scenario, the temperature at both sides of the orogen will not be symmetric. The temperature near the trench is colder as in the retroarc. This will lead to a different distribution of viscosity, expecting high viscosity values near the trench and material that can easily flow in the retroarc. Thus, the influence that the convective cells can have in this scenario will be completely different. Usually, only the one in the retroarc will have the capacity to drag the descendant ma-

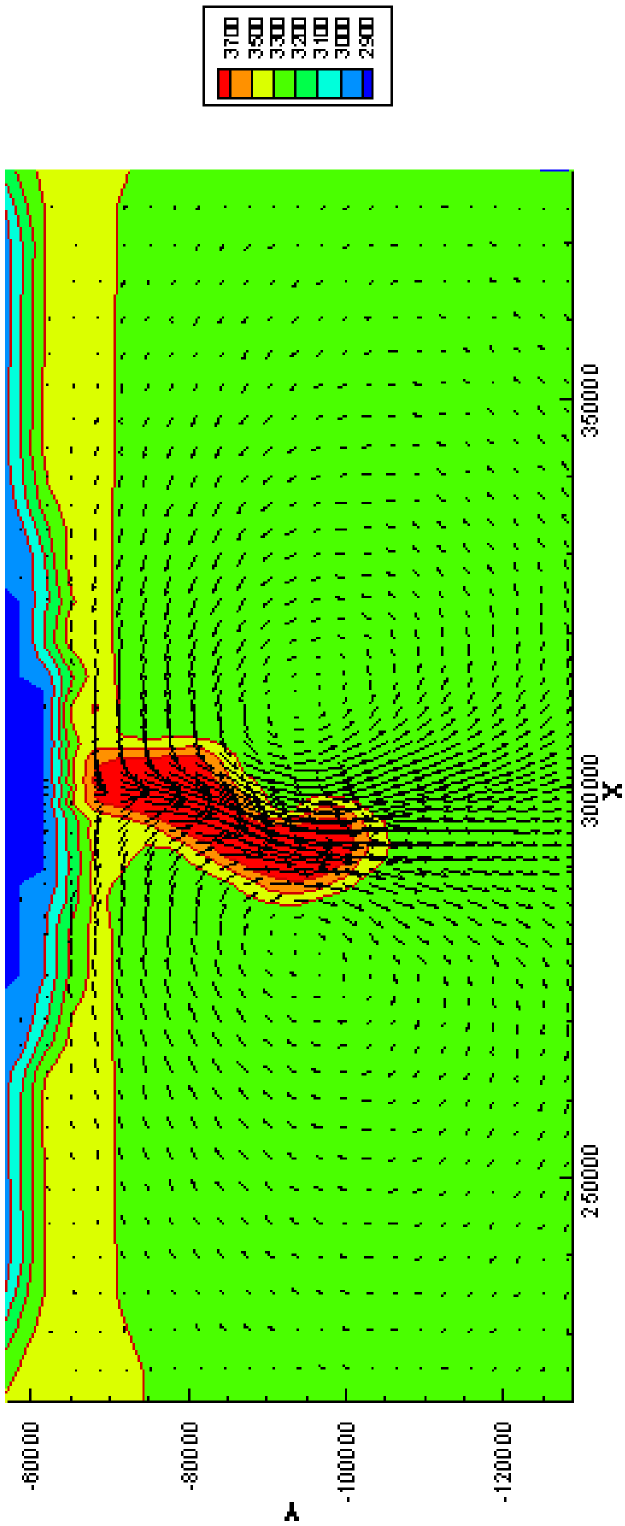

Figure 6.9: Convective cells acting during the delamination process.

terial, while the other can be much slower and only driven by the traction of the oceanic slab being subducted.

After 3.5 My, the income of fluids ends and the transformation from lower crust to eclogite stops. However, the delamination process evolves until 7/8 My, when the eclogite detaches from the lower crust and sinks into the asthenosphere.

6.2.3 Isostatic rebound

Other process that is tightly associated with delamination is the *isostatic rebound*. This effect happens after the detachment of the eclogite from the lower crust. Then, the crust should elevate in order to compensate the losing of the heavy crustal root. The evolution of topography associated with the different stages of the delamination process can be seen in figure 6.12.

It is shown that the maximum orogen elevation reduces continuously since the first eclogite appears. As the orogen collapses to compensate the extra weight, more lower crust is converted to eclogite, due to the tectonic stacking and the presence of fluids. Once the system is completely out of fluids, it starts to stabilize slowly.

However, the system gets unstable again as soon as the root detaches from the lower crust. At that moment, the descendant force that was applied at the base of the crust diminishes and the orogen elevates until a new stabilization equilibrium is reached[1].

6.3 Framework evaluation

6.3.1 Efficiency measures

We consider two different ways to measure the efficiency of the framework proposed. In the first place, we present some figures associated with the time needed to solve a

[1]In other experiments, a relationship between the amount of time that the fluids are present and the magnitude of the isostatic rebound was found. It could be seen that if the presence of fluids lasts longer more eclogites are formed and the isostatic rebound decreases. However, the results are still preliminary to be included in this thesis.

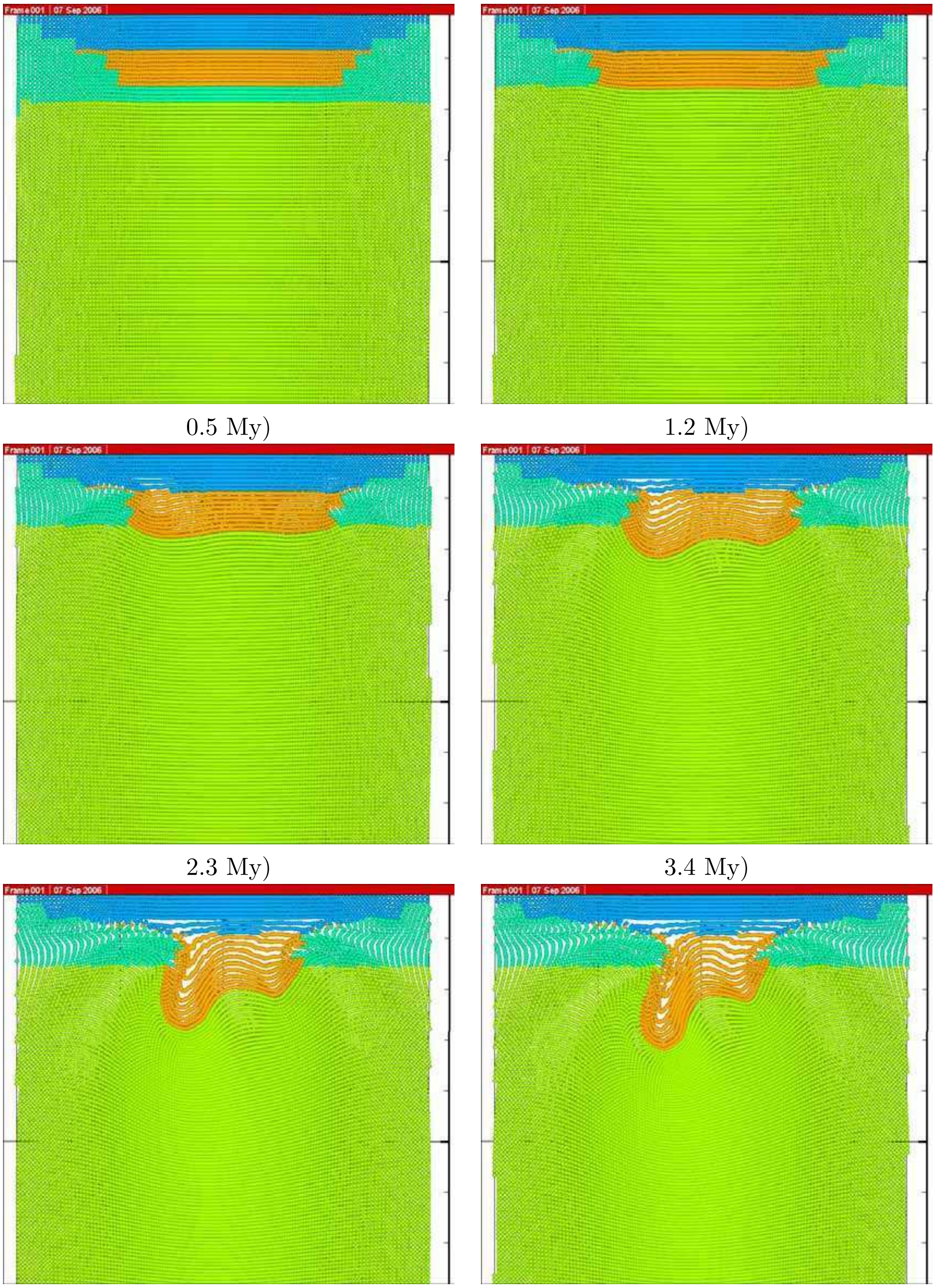

0.5 My) 1.2 My)

2.3 My) 3.4 My)

4.5 My) 5.0 My)

Figure 6.10: Evolution of the particles during the *delamination* process of part of the lower crust.

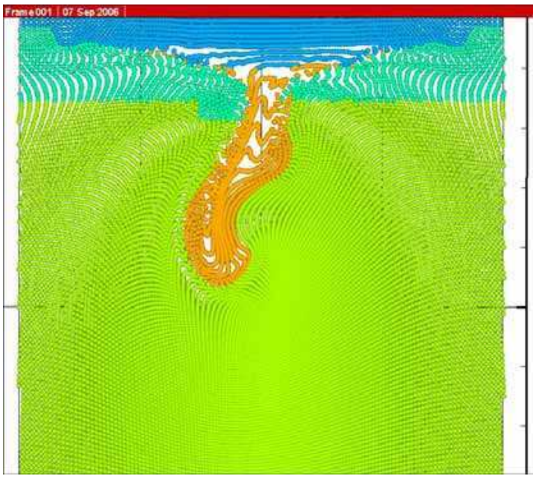

6.2 My)

6.7 My)

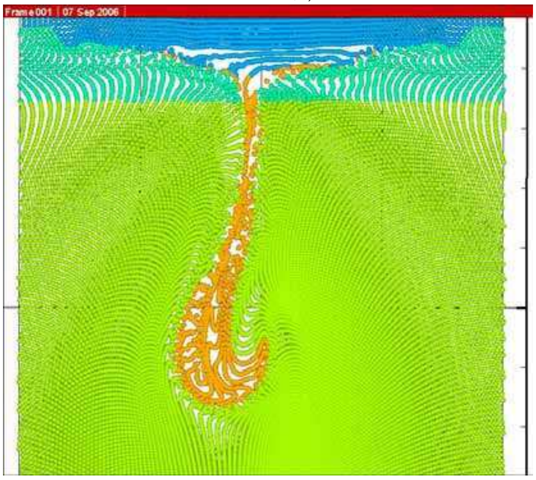

7.5 My)

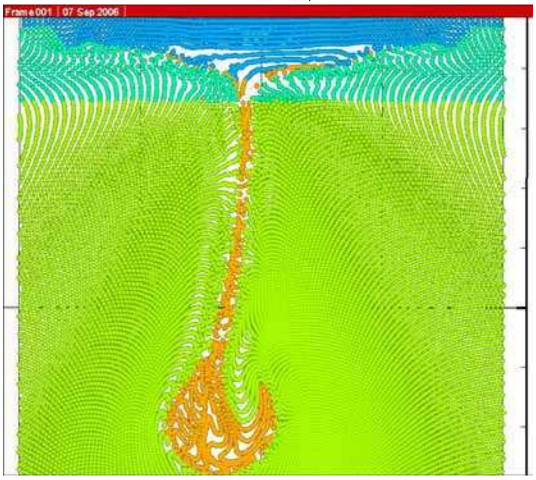

8.2 My)

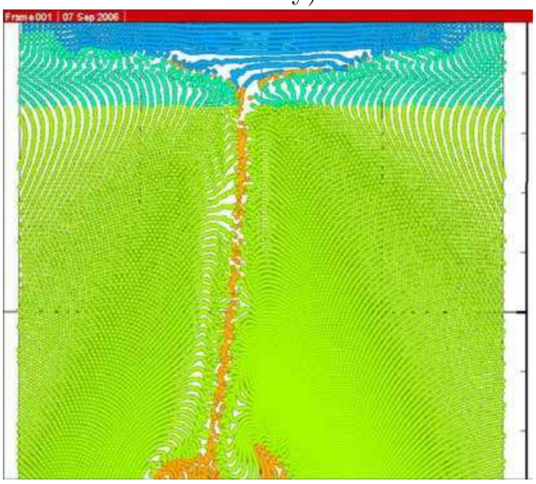

9.0 My)

Figure 6.11: Evolution of the particles during the *delamination* process of part of the lower crust.

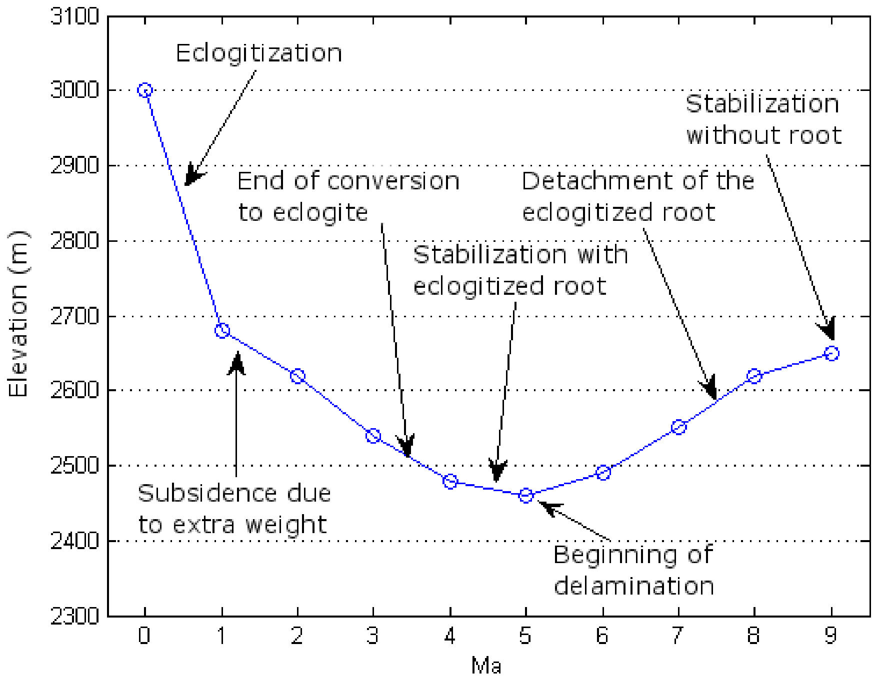

Figure 6.12: Evolution of the maximum orogen elevation during the simulation (0-9 My).

problem varying the number of degrees of freedom and specifying the amount of time dedicated to every stage.

However, we consider very important another point of view about efficiency that is more related to the good design of the framework in all the topics previously described. We decided to calculate the extra effort (lines of code) needed to include the solution of a new PDE equation or change the element employed to solve the existing ones.

6.3.2 Computational time

To calculate the seconds spent in each stage, the isoviscous instability Rayleigh-Taylor test was run with the element detailed in section 4.2.3.

The simulations were executed in a Pentium Dual Core (1.6 GHz each) laptop with 800 MB RAM. The operative system is a Gentoo Linux distribution (kernel version 2.6) and no other resource-consuming tasks were executed concurrently. The results can be

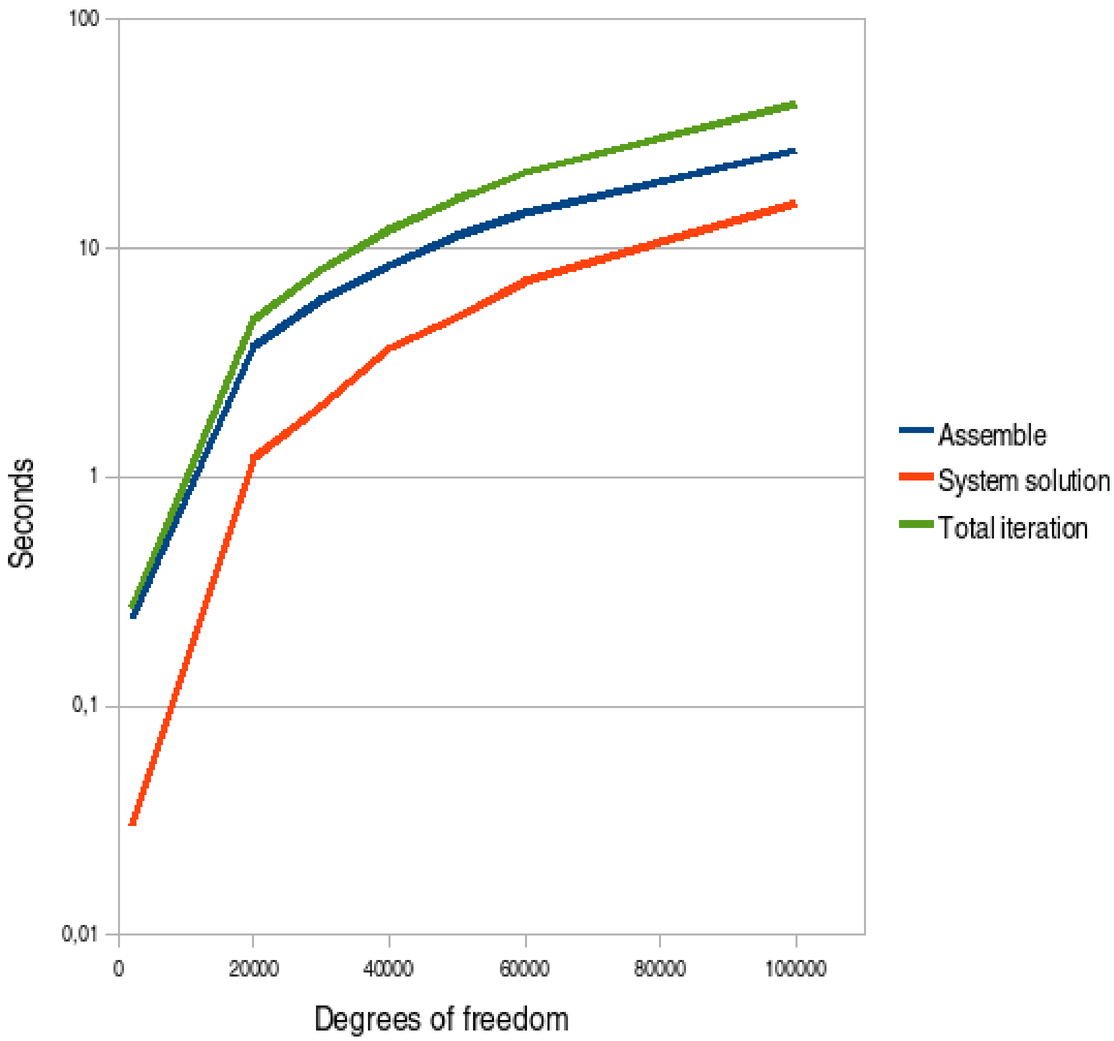

Figure 6.13: Seconds invested to solve an iteration of a non-linear problem as a function of degrees of freedom.

seen in table 6.2 and in figure 6.13.

The same results but expressed as a percentage of the whole iteration can be seen in table 6.3 and in figure 6.14. One can see that, as the number of degrees of freedom grows, is the resolution of the system the stage that requires more resources. Due to this reason, other libraries than SuperLU are being analyzed in order to have another alternatives. In particular Pardiso (Schenk et al., 2001), that is considered to have a very good performance and that also supports not only a row/column compressed format, but the storage of only half the matrix in case of symmetry.

Every single part of the code is being continuously improved from a time-consumption point of view as can be seen if the results were compared with the ones published in Quinteros et al. (2007).

6.3.3 Framework scalability

Flexibility, modularization and proper abstractions in the design of the system allowed that many different problems related to PDE equations can be solved reusing the common parts of the model and coding only the particular features of the problem.

One can see in table 6.4 the type of problems that can already be solved, the related equations and the number of extra lines needed to implement the resolution[2]. It's clear that the resolution of a new type of problem can be achieved with a very low cost due to the flexibility of the model and the reuse of code.

As it was remarked in the previous section, the convergence property of the high order interpolation elements (8 or 9 nodes) are well known(Brezzi and Fortin, 1991). Unfortunately, using that amount of nodes has an important drawback: the computational cost, that can sometimes be unaffordable.

In our case, a novel formulation to solve a geological problem could be tested and validated with a high order element (8 nodes), but actually the experiments were run with a four noded element, allowing us to save time and resources. In fact, we could be

[2]The number of lines needed was calculated as the increment of the total lines of code in percentage starting from the basic model.

Degrees of freedom	Assemblage	System solution	Iteration
2000	0,24	0,03	0,27
20000	3,71	1,24	4,95
30000	5,94	2,05	7,99
40000	8,39	3,60	11,99
50000	11,35	5,02	16,37
60000	14,16	7,18	21,34
100000	26,75	15,79	42,54

Table 6.2: Seconds invested to solve a whole iteration at each stage.

Degrees of freedom	Assemblage	System solution
2000	88,89%	11,11%
20000	74,95%	25,05%
30000	74,34%	25,66%
40000	69,97%	30,03%
50000	69,33%	30,67%
60000	66,35%	33,65%
100000	62,88%	37,12%

Table 6.3: Percentage of the total time spent at each stage.

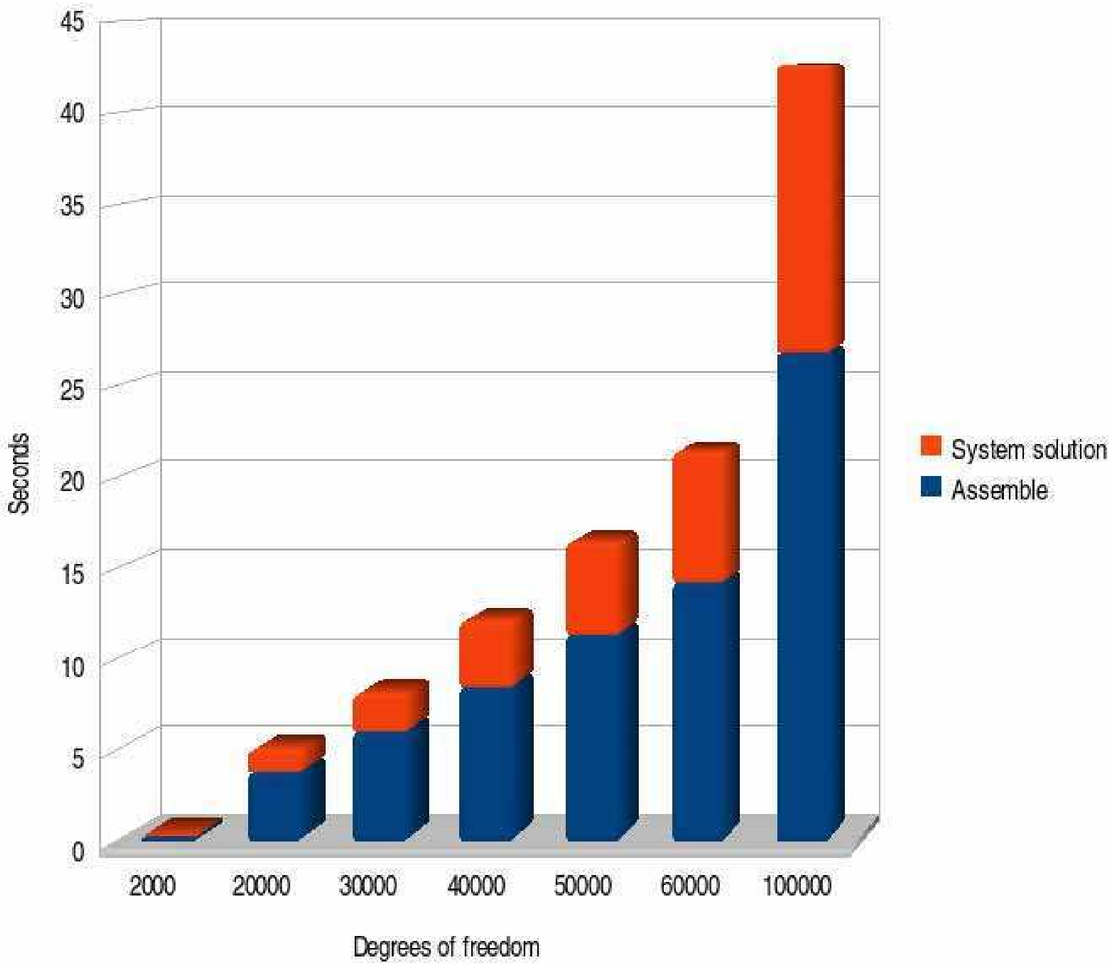

Figure 6.14: Percentage of the total time spent at each stage as a function of degrees of freedom.

Problem	Equation	Extra lines of code compared to total lines
Thermal	Poisson	1.36 %
Remeshing	Laplace	1.13 %
Elasto-visco-plastic solids deformation	(see Quinteros et al. (2006b))	4.91 %
Whole replacement of element in the three equations		6.94 %

Table 6.4: Equations implemented up to this moment and extra lines of code needed to implement the solution.

sure that if any of the experiments failed it was because of the element and not because of the formulation.

Only minor modifications were necessary in the code to change the selected element due to the use of a proper interface by means of the `Element` class.

The results were identical with both elements. The only difference was the number of times that a remeshing was applied. In the case of the Liu element remeshing was necessary to solve the *hourglass mode* inside the domain. That happens because the element proposed by Liu et al. (1994) *diminishes* these modes, but does not prevent the accumulated effects after a big number of time steps.

The different remeshing techniques implemented (Carey and Oden, 1984) and the *Markers* employed (Harlow and Welch, 1965) to translate the state between both meshes were indirectly validated by the Rayleigh-Taylor instability test case.

7

Conclusions

Two different original models have been presented in this thesis. The one presented in chapter 3 is based on Stokes equations to simulate the visco-plastic behaviour of the upper crust. The underlying assumption that the elastic strain can be discarded makes it simple and suitable only to simulate large-scale and long-term evolution of the lithosphere. A typical steady distribution of temperature associated with subduction zones was employed. The isostatic compensation was achieved by means of the numerical resolution of the Timoshenko's beam equation. A superficial erosion model was also developed to study the relationship between climate and tectonic deformation, while numerical techniques were applied to simulate crustal erosion next to the trench.

The boundary conditions employed are more appropriate compared to the ones used in Beaumont et al. (1992), Willett (1999a,b).

A proper feedback was established between the three components (tectonic deformation, isostatic compensation and superficial erosion) through time. The model was implemented in MATLAB and, thus it has some limitations in the number of elements that can handle.

In spite of this, satisfactory results were obtained with this model, particularly developed to study subduction zones. The Miocene evolution of the Patagonian Andes could be simulated. The results showed a good agreement with the constraints imposed by geological evidences.

In this particular case, it is important to remark that the modelling of the active processes in this region during such a long period of time is new, contributing to support some geological hypotheses about the Miocene deformation of the Andes at these latitudes.

In addition, the capability of following the topographic evolution through millions of years, of quantifying eroded volumes of rock and the time where it could have happened, of knowing the tectonic stresses distribution inside the upper crust, of understanding the way in which thermal conditions are related to mechanical properties of the crust and of achieving the flexibility to adapt to multiple geometries and configurations through the correct setting of parameters, among other features, turns this model into a powerful and flexible tool for a geologist researching large-scale evolution of non-collisional orogens formed parallel to subduction zones.

However, the formulation of this type of models suffers from some drawbacks, namely in the calculation of isostatic compensation by means of a second model. Firstly, it can lead to high spurious stresses due to the unreal boundary conditions imposed on the bottom of the domain. The material uplifts because of the conditions but is later compensated downwards by the isostatic model, as a result of the tectonic stacking. Then, all the material uplifts (at a first approximation) while in nature a great part of the shortening sinks and only a minor part rises up.

In the second place, the compensation level exists at a certain shallow level in lithosphere. If the studied domain needs to include the asthenosphere, the isostatic compensation model would be impractical or even not proper. Thus, the inclusion of an elastic behaviour that holds the stress to compensate regionally the load distribution considering the restoring forces is completely necessary to achieve a broader simulation. One can see then that the absence of an *elastic component*, that was discarded in the tectonic deformation model based on Stokes equations, in fact was actually included in an unnatural way within the beam equation.

The model presented in chapter 4 was based on deformation of solids. It could simulate elasto-visco-plastic behaviour of the rocks to a depth of 410 km approximately under different kinematical conditions. Due to its characteristics, the compensation model is not necessary and all the mentioned drawbacks are addressed.

The formulation proposed has been implemented with the following features:

- four nodes element: requires less computational effort to calculate the solution,
- reduced and selective integration: avoids the volumetric locking and implies a lower computational cost,
- a modified gradient matrix: diminishes the *hourglass* effect caused by the reduced integration.

Also, as the model formulation relays on an implicit approach larger time steps can be employed compared to Sobolev and Babeyko (2005), Babeyko et al. (2002).

A thermal model was appropriately coupled to the tectonic model in order to accurately calculate the viscosity values over the domain.

The domain studied can have an arbitrary number and distribution of materials, whose properties are parametrized and, hence, are independent from the model.

Also, a remeshing algorithm based on the Laplace equation was implemented. The position of the nodes belonging to the boundary is imposed as a Dirichlet condition. The translation of the domain state from the distorted mesh to the undistorted one is calculated after remeshing based on the information (stress, material properties) stored by the markers (Lagrangian particles).

The different types of behaviour were validated by means of well known test cases. Thus, not only the results are validated, but also the good performance of the remeshing algorithm and the mapping of the state variables between the old and new mesh could be tested by the Rayleigh-Taylor instability test case.

The model was employed to study the insights of a geodynamic process called *delamination*. As an example, the evolution of a 150 km deep and 300 km wide domain consisting of lithosphere and asthenosphere through more than 8 My was simulated. In this experiment, the root of the orogen detaches from the lower crust because of its transformation into a dense eclogite.

The points of weakness of the domain could be identified, namely the contact between the eclogite and the base of the remaining crust and the core of the volume of eclogite existant. Also, the force exerted by the mantle from the sides, the eclogite ductility and its increased weight due to its higher density were established as the main causes for the formation of a descendant plume, that is pushed and deformed by convective cells of hot asthenosphere.

The isostatic rebound that would imply the detachment of the crustal roots of a stabilized 3 km height orogen was quantified. After collapsing 550 m, the detachment of the eclogitized root starts and the orogen uplifts isostatically. When the detachment finishes, the roots sink into the asthenosphere and the orogen finds the new state of equilibrium. From the 550 m of collapse, the orogen recovers almost 200 m.

A full-featured general purpose FEM framework was presented in chapter 5. The model presented in chapter 4 was actually implemented over this framework.

A detailed description of the design and implementation of the proposed framework to solve PDE related problems by means of the finite element method was presented. Its modular design and the proper use of abstractions give a huge flexibility to employ different types of elements to solve the problem. It also benefits from the reuse of previously validated code, reducing the number of bugs and increasing the trustfulness in the case of unknown solutions.

An eight nodes element that is not used in the experiments was implemented, only to test the flexibility of the framework, with good results. Some performance measures about the framework were given showing that is not only flexible but also fast from a time consumption point of view.

As a concluding remark, it should be mentioned that the development and the use of numerical models as tools to achieve a better understanding of the geodynamic processes at a significant depth is of a great importance for geology, because the lack of direct evidences and measures turns any quantification into an untrustful task. In this direction, two different approaches to study geodynamic problems are provided.

In addition, from a computational point of view, a generic framework to solve partial differential equations by means of the FEM was designed and implemented, not as a ready-made tool but as a base to guide future developments of other researchers, who could use and/or enhance the framework with their own work.

7.1 Future works and enhancements

Although far from the scope of this thesis, the framework presented is being enhanced with the implementation of high order spectral elements (Patera, 1984, Karniadakis et al., 1985) and elements that include the *condensation* of the inside nodes (see for instance Henderson and Karniadakis, 1995).

In addition, the implementation of a novel method called *Kinematic Laplacian Equation* developed by Ponta (2005) to solve fluid dynamics problems is being included in the equations that can be solved by means of this framework. Some results and features of this method can be seen in Otero (2006).

Up to this moment, the boundary conditions have limitations in the case that these were time dependent. To avoid this limitation, a code called *muParser* is being evaluated to allow the definition of boundary conditions that are actually functions that depend on time and not constants. By means of this parser the function can be parametrized and it will not be necessary to compile it into the code.

The Pardiso library (Schenk et al., 2001) is being analyzed in order to be incorporated as an alternative option to SuperLU (Demmel et al., 1999).

From a geological point of view, the application of this model to other geodynamic cases has just started. The examples presented here are only the first of many that could be simulated by means of these tools and open a new world of comparative tectonics that could help to validate different geological models proposed based on fragmentary evidence. In that way, the present research will contribute not only to a better understanding of the processes, but also to set new premises that can be validated by geological observations generating an iterative approach to some fundamental geodynamic problems.

The influence of the friction coefficient in the contact between the subducted and overriding plate and the consequences related to the evolution of the fold and thrust belt, the key role played by the sediments in the trench, the thermal anomalies caused by magma intrusions, the subduction of seismic and aseismic ridges, medium scale problems associated with the evolution of structures in the crust, the influence of fluids in some particular and specific tectonic settings, the formation of foreland basins, the study of the migration of forebulges related to the orogenic front motion and many others are just examples of future cases that could be simulated by means of the model presented here.

A

Specification of some implemented classes

The following is a list with the description of some selected operations implemented on the `Matrix` and `SparseMatrix` classes that are usually useful in the programming stage of the models based on the finite element method.

A.1 Matrix

operator=: Copies the contents of a matrix into another one. Optionally, it can copy the values from a buffer.

operator<<: Friendly output of the contents to an output stream (e.g. console). The format can be imported to Matlab and other programs.

operator(): Gets the value stored in the specified position.

Get: Same as operator().

Save: Stores the instance in an output stream (e.g. file).

maxabs: Returns the maximum absolute value of the Matrix. Optionally, it can search only in the positions determined by a container passed as a parameter.

blank: Erases all the values of the matrix.

Assemble2D: Assembles the given elemental matrix into the global one. The mapping parameter can be a generic container or a Matrix object. Optionally, the mapping for rows and columns can be different.

Assemble1D: Assembles the given elemental vector into the global one. The mapping parameter can be a generic container or a Matrix object.

SecondInv: Returns the second invariant of a tensor.

solve: Solves the system determined by $K * U = R$, where K is the stiffness matrix and R is the force vector passed as a parameter.

operator*: Matrix multiplication.

operator-: Matrix substraction.

operator+: Matrix addition.

operator+=: Adds two matrices, or one matrix and a scalar, and stores the result in the first one.

operator-=: Substracts two matrices, or one matrix and a scalar, and stores the result in the first one.

operator*=: Multiplies a matrix and a scalar and stores the result in the first one.

trans: Returns the transpose of the matrix.

inv: Returns the inverse of the matrix.

length: Returns the number of components of the matrix.

copyrow: Copies one row to another matrix.

copycol: Copies one column to another matrix.

sumRows: Returns a column vector with the sum of the rows.

sumCols: Returns a row vector with the sum of the columns.

multRows: Returns a column vector with the product of the components in each row.

multCols: Returns a row vector with the product of the components in each column.

A.2 SparseMatrix

operator=: Copies the contents of a matrix into another one.

operator<<: Friendly output of the contents to an output stream (e.g. console).

operator(): Gets the value stored in the specified position.

Get: Same as operator().

Set: Sets the value of a specified position.

Add: Adds a value at a specified position.

Save: Stores the instance in an output stream (e.g. file).

flush: Includes into the matrix the values stored in the buffer.

maxabs: Returns the maximum absolute value of the Matrix.

blank: Erases all the values of the matrix. Optionally, the structure can be kept and the values replaced with 0 to speed the assemblage of the next matrix.

Assemble2D: Assembles the given elemental matrix into the global one. The mapping parameter can be a generic container or a Matrix object. Optionally, the mapping for rows and columns can be different.

Pack: Changes the storage to actually save only the lower half of the matrix in case of symmetry.

solve: Solves the system determined by $K * U = R$, where K is the stiffness matrix and R is the force vector passed as a parameter.

Bibliography

P. A. Allen and J. R. Allen. *Basin analysis, principles & applications.* Blackwell Scientific Publications, Oxford, 1990.

E. Anderson, Z. Bai, C. Bischof, S. Blackford, J. Demmel, J. Dongarra, J. Du Croz, A. Greenbaum, S. Hammarling, A. McKenney, and D. Sorensen. *LAPACK users' guide*. Society for Industrial and Applied Mathematics, Philadelphia, PA, third edition, 1999. ISBN 0-89871-447-8 (paperback).

H. Austrheim. Influence of fluid and deformation on metamorphism of the deep crust and consequences for the geodynamics of collision zones. In B. R. Hacker and J. G. Liou, editors, *When continents collide: geodynamics and geochemistry of ultrahigh-pressure rocks*, pages 297–323. Kluwer Academic Publishers, 1998.

Andrey Y. Babeyko and Stephan V. Sobolev. Quantifying different modes of the late cenozoic shortening in the Central Andes. *Geology*, 33:621–624, 2005.

Andrey Y. Babeyko, Stephan V. Sobolev, R. B. Trumbull, Onno Oncken, and L. L. Lavier. Numerical models of crustal scale convection and partial melting beneath the Altiplano - Puna plateau. *Earth and Planetary Science Letters*, 199:373–388, 2002.

Andrey Y. Babeyko, Stephan V. Sobolev, Tim Vietor, Onno Oncken, and Robert B. Trumbull. Numerical study of weakening processes in the Central Andean back-arc. In Onno Oncken, Guillermo Chong, Gerhard Franz, Peter Giese, Hans-Jürgen Götze, Víctor A. Ramos, Manfred R. Strecker, and Peter Wigger, editors, *The Andes - Active subduction orogeny*, chapter 24, page 569 pp. Springer-Verlag, 2006.

Klaus-Jurgen Bathe. *Finite element procedures.* Prentice Hall, New Jersey, 1996.

Christopher Beaumont, Philippe Fullsack, and Juliet Hamilton. Erosional control of active compressional orogens. In K. R. McClay, editor, *Thrust tectonics*, pages 1–18. Chapman and Hall, New York, 1992.

Christopher Beaumont, M. H. Nguyen, R. A. Jamieson, and S. Ellis. Crustal flow modes in large hot orogens. In R. D. Law, M. P. Searle, and L. Godin, editors, *Channel flow, ductile extrusion and exhumation in continental collision zones*, pages 91–145. Geological Society of London, 2006.

Mark D. Behn, Jian Lin, and Maria T. Zuber. A continuum mechanics model for normal faulting using a strain-rate softening rheology: implications for thermal and rheological controls on continental and oceanic rifting. *Earth and Planetary Science Letters*, 202:725–740, 2002.

Hugo Benioff. Orogenesis and deep crustal structure: Additional evidence from seismology. *GSA Bulletin*, 64:385–400, 1954.

Peter M. Blisniuk, Libby A. Stern, C. Page Chamberlain, Bruce Idleman, and Peter K. Zeitler. Climatic and ecologic changes during Miocene surface uplift in the Southern Patagonian Andes. *Earth and Planetary Science Letters*, 230:125–142, 2005.

J. Bourgois, H. Martin, J. Le Moigne, and J. Frutos. Subduction erosion related to spreading-ridge subduction: Taitao peninsula (Chile margin triple junction area). *Geology*, 24(8):723–726, 1996.

F. Brezzi and M. Fortin. *Mixed and hybrid finite elements methods*. Springer-Verlag, 1991.

Benjamin Brooks, Michael Bevis, Robert Jr. Smalley, Eric Kendrick, René Manceda, Eduardo Lauria, Rodrigo Maturana, and Mario Araujo. Crustal motion in the Southern Andes (26° - 36°): Do the Andes behave like a microplate? *Geochemistry, Geophysics, Geosystems*, 4(10): 1085, 2003.

E. B. Burov and M. Diament. The effective elastic thickness (T_e) of continental lithosphere: What does it really means? *Journal of Geophysical Research*, 100:3905–3927, 1995.

J. Byerlee. Friction of rocks. *Pure and Applied Geophysics*, 116:615–626, 1978.

S. C. Cande and R. B. Leslie. Late Cenozoic tectonics of the Southern Chile trench. *Journal of the Geophysical Research*, 91:471–496, 1986.

A. Cardona, I. Klapka, and M. Geradin. Design of a new finite element programming environment. *Engineering Computation*, 11(4):365–381, 1994.

Graham F. Carey and J. Tinsley Oden. *Finite elements - computational aspects - volume III.* Prentice-Hall, Inc., New Jersey, first edition, 1984.

P. N. Chopra and M. S. Paterson. The role of water in the deformation of the dunite. *Journal of Geophysical Research*, 89:7861–7876, 1984.

Allan Cox and Robert Brian Hart. *Plate tectonics - How it works.* Blackwell Science, Inc., 1986.

S. H. Crandall, N. C. Dahl, and T. J. Lardner. *An introduction to the mechanics of solids.* McGraw-Hill, New York, second edition, 1978.

Ernesto O. Cristallini and Richard W. Allmendinger. Pseudo 3-D modeling of trishear fault-propagation folding. *Journal of Structural Geology*, 23:1883–1899, 2001.

Enzo A. Dari, Gustavo C. Buscaglia, and Adrian Lew. A parallel general purpose finite element system. In *IX SIAM Conference on Parallel Processing for Scientific Computing*, San Antonio, Texas, USA, Mar 1999.

Geoffrey F. Davies. *Dynamic Earth: plates, plumes and mantle convection.* Cambridge University Press, 1999.

James W. Demmel, Stanley C. Eisenstat, John R. Gilbert, Xiaoye S. Li, and Joseph W. H. Liu. A supernodal approach to sparse partial pivoting. *SIAM J. Matrix Analysis and Applications*, 20(3):720–755, 1999.

I.S. Duff, R.G. Grimes, and J.G. Lewis. Users' guide for the Harwell-Boeing sparse matrix collection (release 1). Technical Report RAL-92-086, Rutherford Appleton Laboratory, dec 1992.

W. G. Ernst. Systematics of large-scale tectonics and age progressions in Alpine and Circum-Pacific blueschist belts. *Tectonophysics*, 26:229–246, 1975.

P. Flemings and T. E. Jordan. A synthetic stratigraphic model of foreland basin development. *Journal of Geophysical Research*, 94:3851–3866, 1989.

Philippe Fullsack. An arbitrary Lagrangian-Eulerian formulation for creeping flows and its application in tectonic models. *Geophysics Journal International*, 120:1–23, 1995.

A. Gansser. Facts and theories of the Andes. *Journal of the Geological Society*, 129:93–131, 1973.

Daniel García Castellanos, M. Fernández, and M. Torne. Numerical modeling of foreland basin formation: a program relating thrusting, flexure, sediment geometry and lithosphere rheology. *Computers and Geosciences*, 23(9):993–1003, 1997.

Lykke Gemmer, Sø ren B. Nielsen, and Ulf Bayer. Late Cretaceous-Cenozoic evolution of the North German Basin – results from 3-D geodynamic modelling. *Tectonophysics*, 373:39–54, 2003.

Matías C. Ghiglione, Javier Quinteros, Julio Hlebszevitsch, Daniel Yagupsky, Claudio Haring, and Gustavo Vergani. Cuencas del extremo Austral de la Placa Sudamericana: Diferencias, conexiones y una historia en común. In *Actas del XVI Congreso Geológico Argentino*, volume 1, pages 201–206, La Plata, Argentina, Sep 2005. ISBN 987-595-001-7.

Vivette Girault and Pierre-Arnaud Raviart. *Finite element methods for Navier-Stokes equations*. Springer-Verlag, Berlin, 1986.

G. C. Gleason and Jan Tullis. A flow law for dislocation creep of quartz aggregates with the molten salt cell. *Tectonophysics*, 247:1–23, 1995.

Francis H. Harlow and J. Eddie Welch. Numerical calculation of time-dependent viscous incompressible flow of fluid with free surface. *The Physics of Fluids*, 8(12):2182–2189, 1965.

R. D. Henderson and G. E. Karniadakis. Unstructured spectral element methods for simulation of turbulent flows. *Journal of Computational Physics*, 122:191–217, 1995.

Francisco Hervé, Alain Demant, Víctor A. Ramos, Robert J. Pankhurst, and Manuel Suárez. The Southern Andes. In U. G. Cordani, E. J. Milani, A. Thomaz Filho, and D. A. Campos, editors, *Tectonic Evolution of South America*, pages 605–634, Rio de Janeiro, 2000. International Geological Congress.

David Hindle, Oliver Besson, and Martin Burkhard. A model of displacement and strain for arc-shaped mountain belts applied to the Jura arc. *Journal of Structural Geology*, 22:1285–1296, 2000.

A. D. Howard and D. Kerby. Channel changes in badlands. *Geological Society of American Bulletin*, 94:739–752, 1983.

Thomas J. R. Hughes. Generalization of selective integration procedures to anisotropic and nonlinear media. *International Journal for Numerical Methods for Engineering*, 15:1413–1418, 1980.

Thomas J. R. Hughes and James Winget. Finite rotation effects in numerical integration of rate constitutive equations arising in large-deformation analysis. *International Journal for Numerical Methods for Engineering*, 15:1862–1867, 1980.

B. Isacks. Uplift of the central andean plateau and bending of the bolivian orocline. *Journal of Geophysical Research*, 93(B4):3211–3231, 1988.

B. Isacks, L. R. Sykes, and J. Oliver. Seismology and new global tectonics. *Journal of Geophysical Research*, 73:5855–5899, 1968.

Olivier Jaoul, Jan Tullis, and Andreas Kronenberg. The effect of varying water contents on the creep behavior of heavytree quartzite. *Journal of Geophysical Research*, 89(B6):4298–4312, 1984.

M. Kameyama, D. A. Yuen, and S. I. Karato. Thermal-mechanical effects on low-temperature plasticity (the Peierls mechanism) on the deformation of a viscoelastic shear zone. *Earth and Planetary Science Letters*, 168:159–172, 1999.

G. D. Karner, M. S. Steckler, and J. A. Thorne. Long-term thermo-mechanical properties of the lithosphere. *Nature*, 304:250–252, 1983.

G. E. Karniadakis, E. T. Bullister, and A. T. Patera. A spectral element method for solution of two- and three-dimensional time-dependent incompressible Navier-Stokes equations. In *Finite Element Methods for Nonlinear Problems*, page 803. Springer-Verlag, 1985. Elementos espectrales.

Robert W. Kay and Suzanne Mahlburg Kay. Delamination and delamination magmatism. *Tectonophysics*, 219:177–189, 1993.

Suzanne Mahlburg Kay, Estanislao Godoy, and Andrew Kurtz. Episodic arc migration, crustal thickening, subduction erosion, and magmatism in the south-central Andes. *Geological Society of America Bulletin*, 117(1/2):67–88, 2005.

D. L. Kohlstedt, B. Evans, and S. J. Mackwell. Strength of the lithosphere: constraints imposed by laboratory experiments. *Journal of Geophysical Research*, 100:17587– 17602, 1995.

Simon Lamb and Paul Davis. Cenozoic climate change as a possible cause for the rise of the Andes. *Nature*, 425:792–797, 2003.

Mary L. Leech. Arrested orogenic development: eclogitization, delamination, and tectonic collapse. *Earth and Planetary Science Letters*, 185:149–159, 2001.

Wing Kam Liu, Yu-Kan Hu, and Ted Belytschko. Multiple Quadrature underintegrated finite elements. *International Journal for Numerical Methods in Engineering*, 37:3263–3289, 1994.

William Lowrie. *Fundamentals of geophysics*. Cambridge University Press, 1997.

S. J. Mackwell, M. E. Zimmerman, and D. L. Kohlstedt. High temperature deformation of dry diabase with application to tectonics on Venus. *Journal of Geophysical Research*, 103(B1): 975–984, 1998.

L. E. Malvern. *Introduction to the mechanics of a continuous medium*. Prentice-Hall, 1969.

Motonori Matuyama. On the direction of magnetization of basalt in Japan, Tyosen and Manchuria. *Proceedings of the Imperial Academy of Japan*, 5:203–205, 1929.

David R. Montgomery, Greg Balco, and Sean D. Willett. Climate, tectonics, and the morphology of the andes. *Geology*, 29:579–582, 2001.

Eldridge M. Moores and Robert J. Twiss. *Tectonics*. W. H. Freeman and Company, 1995.

L. N. Moresi, F: Dufour, and H. B. Muhlhaus. A Lagrangian integration point finite element method for large deformation modeling of viscoelastic geomaterials. *Journal of Computational Physics*, 184:476–497, 2003.

Lawrence Morley and A. Larochelle. Paleomagnetism as a means of dating geological events. In *Geochronology in Canada*, pages 39–50. Royal Society of Canada, 1964.

Roman Y. Novoselov, Dale A. Lawrence, and Lucy Y. Pao. Haptic rendering of data on unstructured tetrahedral grids. In *Symposium on haptic interfaces for virtual environment and teleoperator systems*, pages 193–200, 2002.

F. E. Nullo and A. M. Combina. Sedimentitas terciarias continentales. In M. J. Haller, editor, *Geología y recursos naturales de Santa Cruz. Relatorio del XV Congreso Geológico Argentino. El Calafate*, volume I-16, pages 245–258, Buenos Aires, 2002. Asociación Geológica Argentina.

Alejandro D. Otero. Spectral element implementation of the KLE method: a (ω, v) formulation of the Navier-Stokes equations. In Alberto Cardona, Norberto Nigro, Victorio Sonzogni, and Mario Storti, editors, *Mecánica Computacional*, volume XXV, pages 2649–2668. AMCA, 2006.

F. Pardo-Casas and P. Molnar. Relative motion of the Nazca (Farallon) and South American plates since late cretacous time. *Tectonics*, 6:233–248, 1987.

A. T. Patera. A spectral element method for fluid dynamics: laminar flow in a channel expansion. *Journal of Computational Physics*, 54:468–488, 1984. Elementos espectrales.

Alexey N. Poliakov, P. A. Cundall, Yuri Y. Podladchikov, and V. A. Lyakhovsky. An explicit inertial method for the simulation of the viscoelastic flow: an evaluation of elastic effects on diapiric flow in two- and three-layers models. In D. B. Stone and S. K. Runcorn, editors, *Flow and Creep in the Solar System: Observations, Modelling and Theory*, pages 175–195. Kluwer Academic Publishers, 1993.

Fernando L. Ponta. The kinematic Laplacian equation method. *Journal of Computational Physics*, 207:405–426, 2005.

Russell N. Pysklywec. Evolution of subducting mantle lithosphere at a continental plate boundary. *Geophysical Research Letters*, 28(23):4399–4402, 2001.

Russell N. Pysklywec and Christopher Beaumont. Intraplate tectonics: feedback between radioactive thermal weakening and crustal deformation driven by mantle lithosphere instabilities. *Earth and Planetary Science Letters*, 221:275–292, 2004.

Russell N. Pysklywec and M. Hosein Shahnas. Time-dependent surface topography in a coupled crust-mantle convection model. *Geophysics Journal International*, 154:268–278, 2003.

Javier Quinteros, Pablo M. Jacovkis, and Víctor A. Ramos. Evolution of the Upper Crustal Deformation in Subduction Zones. *Journal of Applied Mechanics*, 73:984–994, 2006a.

Javier Quinteros, Pablo M. Jacovkis, and Víctor A. Ramos. Formación de cordilleras y delaminación litosférica. un modelo elasto-visco-plástico mediante elementos finitos. In Alberto Cardona, Norberto Nigro, Victorio Sonzogni, and Mario Storti, editors, *Mecánica Computacional*, volume XXV, pages 2669–2686, Santa Fe, Argentina, Nov 2006b. Asociación Argentina de Mecánica Computacional.

Javier Quinteros, Pablo M. Jacovkis, and Víctor A. Ramos. Diseño flexible y modular de modelos numéricos basados en elementos finitos. In Sergio A. Elaskar, Elvio A. Pilotta, and Germán A. Torres, editors, *Mecánica Computacional*, volume XXVI, pages 1724–1740, Córdoba, Argentina, Oct 2007. Asociación Argentina de Mecánica Computacional.

Víctor A. Ramos. Andean foothills structures in Northern Magallanes Basin, Argentina. *The American Association of Petroleum Geologists Bulletin*, 73(7):887–903, 1989.

Víctor A. Ramos. Seismic ridge subduction and topography: foreland deformation in the Patagonian Andes. *Tectonophysics*, 399:73–86, 2005.

William F. Ruddiman, Maureen E. Raymo, Warren L. Prell, and John E. Kutzbach. The uplift-climate connection: a synthesis. In W. F. Ruddiman, editor, *Tectonic Uplift and Climate Change*, chapter 20, pages 471–515. Plenum Press, New York, 1997.

Olaf Schenk, Klaus Gaertner, Wolfgang Fichtner, and Andreas Stricker. Pardiso: a high-performance serial and parallel sparse linear solver in semiconductor device simulation. *Future Generation Computer Systems*, 18:69–78, 2001.

Paul G. Silver, Raymond M. Russo, and Carolina Lithgow-Bertelloni. Coupling of South American and African plate motion and plate deformation. *Science*, 279:60–63, 1998.

J. C. Simo and R. L. Taylor. Consistent tangent operators for rate-independent elasto-plasticity. *Computer Methods in Applied Mechanics and Engineering*, 48:101–118, 1985.

Stephan V. Sobolev and Andrey Y. Babeyko. What drives orogeny in the Andes? *Geology*, 33: 617–620, 2005.

Stephan V. Sobolev, Andrey Y. Babeyko, Ivan Koulakov, and Onno Oncken. Mechanism of the andean orogeny: insight from numerical modeling. In Onno Oncken, Guillermo Chong, Gerhard Franz, Peter Giese, Hans-Jürgen Götze, Víctor A. Ramos, Manfred R. Strecker, and Peter Wigger, editors, *The Andes - Active subduction orogeny*, chapter 25, page 569 pp. Springer-Verlag, 2006.

R. Somoza. Updated Nazca (Farallon) - South America relative motions during the last 40 My: implications for mountain building in the central Andean region. *Journal of South American Earth Sciences*, 11(3):211–215, 1998.

V. E. Sonzogni, A. M. Yommi, N. M. Nigro, and M. A. Storti. A parallel finite element program on a Beowulf cluster. *Advances in Engineering Software*, 33:427–443, 2002.

Luther M. Strayer and John Suppe. Out-of-plane motion of a thrust sheet during along-strike propagation of a thrust ramp: a distinct-element approach. *Journal of Structural Geology*, 24: 637–650, 2002.

John Suppe. *Principles of structural geology.* Prentice Hall, 1985.

Yasumoto Suzuki. Kiyoo Wadati and the path to the discovery of the intermediate-deep earthquake zone. *Episodes*, 24:118–123, 2001.

Edward J. Tarbuck and Frederick K. Lutgens. *Earth. An introduction to physical geology.* Prentice Hall, Inc., 6th. edition, 1999.

Stuart N. Thomson, Francisco Hervé, and Bernhard Stöckhert. Mesozoic-Cenozoic denudation history of the Patagonian Andes (southern Chile) and its correlation to different subduction processes. *Tectonics*, 20(5):693–711, 2001.

S. Timoshenko. *Theory of elasticity.* McGraw-Hill, 1934.

M. C. Tsenn and N. L. Carter. Upper limits of power law creep of rocks. *Tectonophysics*, 136: 1–26, 1987.

D. L. Turcotte and G. Schubert. *Geodynamics: applications of continuum mechanics to geological problems.* Wiley, New York, 1982.

P. E. van Keken, S. D. King, H. Schmeling, U. R. Christensen, D. Neumeister, and M. P. Doin. A comparison of methods for the modeling of thermochemical convection. *Journal of Geophysical Research*, 102:22477–22495, 1997.

Felix Andries Vening-Meinesz. Gravity over the Hawaiian archipelago and over the Madiera area. In *Proc. Netherlands Acad. Wetensch.*, volume 44, pages 1–12, 1941.

Tim Vietor and H. Echtler. Episodic neogene southward growth of the andean subduction orogen between 30° s and 40° s - plate motions, mantle flow, climate, and upper-plate structure. In Onno Oncken, Guillermo Chong, Gerhard Franz, Peter Giese, Hans-Jürgen Götze, Víctor A. Ramos, Manfred R. Strecker, and Peter Wigger, editors, *The Andes - Active subduction orogeny*, chapter 18, page 569 pp. Springer-Verlag, 2006.

F. J. Vine and D. H. Matthews. Magnetic anomalies over oceanic ridges. *Nature*, 199:947–949, 1963.

R. von Huene and D. W. Scholl. Observations at convergent margins concerning sediment subduction, subduction erosion, and the growth of continental crust. *Reviews of Geophysics*, 29: 279–316, 1991.

K. Wadati. Shallow and deep earthquakes. *Geophysical Magazine*, 1:162–202, 1928.

K. Wadati. On the activity of deep-focus earthquakes in the Japan islands and the neighborhoods. *Geophysical Magazine*, 8:305–325, 1935.

Alfred Wegener. *Die Entstehung der Kontinente und Ozeane.* Friedrich Vieweg and Sohn AG, 1915.

Sean D. Willett. Kinematic and dynamic growth and change of a Coulomb wedge. In K. R. McClay, editor, *Thrust tectonics*, pages 19–31. Chapman and Hall, New York, 1992.

Sean D. Willett. Orogeny and orography: the effects of erosion on the structure of mountain belts. *Journal of Geophysical Research*, 104(B12):28957–28981, 1999a.

Sean D. Willett. Rheological dependence of extension in wedge models of convergent orogens. *Tectonophysics*, 305:419–435, 1999b.